Influence of defects and impurities on the properties of 2D materials

SOUMYAJYOTI HALDAR

Dissertation presented at Uppsala University to be publicly examined in Polhemsalen Ång/10134, Ångströmlaboratoriet, Lägerhyddsvägen 1, Uppsala, Friday, 11 November 2016 at 10:15 for the degree of Doctor of Philosophy. The examination will be conducted in English. Faculty examiner: Dr. Torbjörn Björkman (Åbo Akademi University).

Abstract

Haldar, S. 2016. Influence of defects and impurities on the properties of 2D materials. *Digital Comprehensive Summaries of Uppsala Dissertations from the Faculty of Science and Technology* 1432. 100 pp. Uppsala: Acta Universitatis Upsaliensis. ISBN 978-91-554-9699-9.

Graphene, the thinnest material with a stable 2D structure, is a potential alternative for silicon-based electronics. However, zero band gap of graphene causes a poor on-off ratio of current thus making it unsuitable for logic operations. This problem prompted scientists to find other suitable 2D materials. Creating vacancy defects or synthesizing hybrid 2D planar interfaces with other 2D materials, is also quite promising for modifying graphene properties. Experimental productions of these materials lead to the formation of possible defects and impurities with significant influence in device properties. Hence, a detailed understanding of the effects of impurities and defects on the properties of 2D systems is quite important.

In this thesis, detailed studies have been done on the effects of impurities and defects on graphene, hybrid graphene/h-BN and graphene/*graphane* structures, silicene and transition metal dichalcogenides (TMDs) by *ab-initio* density functional theory (DFT). We have also looked into the possibilities of realizing magnetic nanostructures, trapped at the vacancy defects in graphene, at the reconstructed edges of graphene nanoribbons, at the planar hybrid h-BN graphene structures, and in graphene/*graphane* interfaces. A thorough investigation of diffusion of Fe adatoms and clusters by *ab-initio* molecular dynamics simulations have been carried out along with the study of their magnetic properties. It has been shown that the formation of Fe clusters at the vacancy sites is quite robust. We have also demonstrated that the quasiperiodic 3D heterostructures of graphene and h-BN are more stable than their regular counterpart and certain configurations can open up a band gap. Using our extensive studies on defects, we have shown that defect states occur in the gap region of TMDs and they have a strong signature in optical absorption spectra. Defects in silicene and graphene cause an increase in scattering and hence an increase in local currents, which may be detrimental for electronic devices. Last but not the least, defects in graphene can also be used to facilitate gas sensing of molecules as well as and local site selective fluorination.

Keywords: 2D Materials, Defects on 2D materials, Impurities on 2D materials

Soumyajyoti Haldar, Department of Physics and Astronomy, Materials Theory, Box 516, Uppsala University, SE-751 20 Uppsala, Sweden.

*Dedicated to my parents
and to all my teachers*

List of papers

This thesis is based on the following papers, which are referred to in the text by their Roman numerals.

I **Magnetic impurities in graphane with dehydrogenated channels**
Soumyajyoti Haldar, Dilip Kanhere and Biplab Sanyal.
Phys. Rev. B **85**, 155426, (2012)

II **Functionalization of edge reconstructed graphene nanoribbons by H and Fe: A density functional study**
Soumyajyoti Haldar, Sumanta Bhandary, Satadeep Bhattacharjee, Olle Eriksson, Dilip Kanhere and Biplab Sanyal.
Solid State Communications **152**, 1719, (2012)

III **Designing Fe nanostructures at graphene/h-BN interfaces**
Soumyajyoti Haldar, Pooja Srivastava, Olle Eriksson, Prasenjit Sen and Biplab Sanyal.
J. Phys. Chem. C **117**, 21763, (2013)

IV **Quasiperiodic van der Waals heterostructures of graphene and h-BN**
Sumanta Bhandary, **Soumyajyoti Haldar** and Biplab Sanyal.
Manuscript.

V **Fe$_n$(n=1-6) clusters chemisorbed on vacancy defects in graphene: Stability, spin-dipole moment and magnetic anisotropy**
Soumyajyoti Haldar, Bhalchandra S. Pujari, Sumanta Bhandary, Fabrizio Cossu, Olle Eriksson, Dilip Kanhere and Biplab Sanyal.
Phys. Rev. B **89**, 205411, (2014)

VI **Systematic study of structural, electronic, and optical properties of atomic-scale defects in the two-dimensional transition metal dichalcogenides MX$_2$ (M=Mo,W; X =S, Se, Te)**
Soumyajyoti Haldar, Hakkim Vovusha, Manoj Kumar Yadav, Olle Eriksson and Biplab Sanyal.
Phys. Rev. B **92**, 235408, (2015)

VII **Energetic stability, STM fingerprints and electronic transport properties of defects in graphene and silicene**

Soumyajyoti Haldar, Rodrigo G. Amorim, Biplab Sanyal, Ralph H. Scheicher and Alexandre R. Rocha.
RSC Advances **6**, 6702, (2016)

VIII **Improved gas sensing activity in structurally defected bilayer graphene**
Y Hajati, T Blom, S H M Jafri, **S Haldar**, S Bhandary, M Z Shoushtari, O Eriksson, B Sanyal and K Leifer.
Nanotechnology **23**, 505501, (2012)

IX **Site-selective local fluorination of graphene induced by focused ion beam irradiation**
Hu Li, Lakshya Daukiya, **Soumyajyoti Haldar**, Andreas Lindblad, Biplab Sanyal, Olle Eriksson, Dominique Aubel, Samar Hajjar-Garreau, Laurent Simon and Klaus Leifer.
Scientific Reports **6**, 19719, (2016)

Reprints were made with permission from the publishers.

Comments on my participation

The works presented in the Papers I to IX have been done in collaboration with other coauthors. Here, I will briefly state my contributions to them. I have participated in all three parts, planning the research, calculations and writing the manuscript for Papers I – VII. For calculations, there were contributions from PS in Paper III, SB, SB in Paper II, SB in Paper IV, BSP, SB in Paper V, HV, MKY in Paper VI, RGA in Paper VII. PS in Paper III, SB, SB in Paper II, SB in Paper IV and RGA in Paper VII contributed equally in manuscript writing. The experiments in Paper VIII – IX were carried out by the group of KL. In Paper VIII – IX, I have performed the theoretical simulations, have participated in the discussions and have written the corresponding theory part. The IPR calculations in Paper VIII were performed by SB.

Additional publications, but not included in the thesis:

♣ **A systematic study of electronic structure from graphene to *graphane***
Prachi Chandrachud, Bhalchandra S Pujari, **Soumyajyoti Haldar**, Biplab Sanyal and D G Kanhere.
J. Phys.: Condens. Matter **22**, 465502, (2010)

♣ **Metallic clusters on a model surface: Quantum versus geometric effects**
S. A. Blundell, **Soumyajyoti Haldar** and D. G. Kanhere.
Phys. Rev. B **84**, 075430, (2011)

♣ **The dipole moment of the spin density as a local indicator for phase transitions**
D. Schmitz, C. Schmitz-Antoniak, A. Warland, M. Darbandi, **S. Haldar**, S. Bhandary, O. Eriksson, B. Sanyal and H. Wende.
Scientific Reports **4**, 5760, (2014)

♣ **A real-space study of random extended defects in solids: Application to disordered Stone–Wales defects in graphene**
Suman Chowdhury, Santu Baidya, Dhani Nafday, **Soumyajyoti Halder**, Mukul Kabir, Biplab Sanyal, Tanusri Saha-Dasgupta, Debnarayan Jana and Abhijit Mookerjee.
Physica E **61**, 191, (2014)

♣ **Influence of Electron Correlation on the Electronic Structure and Magnetism of Transition-Metal Phthalocyanines**
Iulia Emilia Brumboiu, **Soumyajyoti Haldar**, Johann Lüder, Olle Eriksson, Heike C. Herper, Barbara Brena and Biplab Sanyal.
J. Chem. Theory Comput. **12**, 1772, (2016)

♣ **Metal-Free Photochemical Silylations and Transfer Hydrogenations of Benzene, Polycyclic Aromatic Hydrocarbons and Graphene**
Raffaello Papadakis, Hu Li, Joakim Bergman, Anna Lundstedt, Kjell Jorner, Rabia Ayub, **Soumyajyoti Haldar**, Burkhard O. Jahn, Aleksandra Denisova, Burkhard Zietz, Roland Lindh, Biplab Sanyal, Helena Grennberg, Klaus Leifer and Henrik Ottosson.
Nature Communications **7**, 12962, (2016)

Contents

Part I:
Introduction & The Theoretical Formalism

1. Introduction

*"Where shall I begin, please your Majesty?"
he asked. "Begin at the beginning," the King
said gravely, "and go on till you come to the
end: then stop."*

— Lewis Carroll, Alice in Wonderland

Electronics, a field of science and engineering, deals with electronic devices made of various electrical components e.g., vacuum tubes, diodes, transistors, integrated circuits, etc. [1]. One of the initial discoveries and inventions in the history of electronics goes way back in 1745, when Kleist and Musschenbroek invented Leyden jar, which was the original form of capacitor. Since then, various inventions and discoveries made by numerous notable scientists and inventors built a solid foundation in development of electronic technology. However, the invention of diode (the simpler version of vacuum tube) using the principle of "Edison Effect" by Fleming in 1905, triggered the beginning of modern electronics. Vacuum tubes became integral part of electronics during the early part of 20th century and the invention of these vacuum tubes made the technologies like radio, television, telephone networks, computers, etc. popular and widespread. However, the use of vacuum tubes made these technologies costly and the devices bulky.

Humans have always been mesmerized by the miniaturization's of modern day electronic devices. The semiconductor devices, which were invented in 1940s, made it possible to manufacture smaller, durable, cheaper, and efficient solid-state devices than vacuum tubes. Consequently, these solid-state devices e.g., transistors, gradually started to replace the vacuum tubes in the electronic devices during 1950s. In the pursuit of smaller size, *integrated circuits* (ICs) were invented. The scaling-down of devices is profoundly dependent on the size of *integrated circuits* (IC), which are the heart and brain of modern day electrical and electronic devices. The ICs are made of large number of tiny electronic circuits, which are created on a wafer made of pure semiconductor material, mainly silicon.

Silicon-based electronics, however, restricts the further scaling down of sizes. The performance of these electronic devices depend on the mobility of charge carriers e.g., negatively charged 'electrons' and positively charged 'holes'. As the size of these chips are getting smaller and complex, the ability to move electrons around are reaching its practical limits due to amount of heat dissipation, leakage between the circuits, doping problems, etc. Hence,

in pursuit of new materials and technologies as a possible substitute to silicon is already under way. One of the promising alternative is to use quantum properties e.g., spin of electrons. The spins of electrons can be aligned either *up* or *down*, which are alike internal bar magnets. The flipping of spins does not require energy to move charge carriers physically, a property that scientists are eager to use for transporting information in 'spintronic' devices. Among several other alternatives [2], such as multigate transistors, III-V compound semiconductors, germanium nanodevices, carbon nanotubes, etc., graphene, a two dimensional monolayer of carbon atoms arranged in a honeycomb lattice [3, 4], has become most promising.

Theoreticians have been studying properties of graphene or '2D graphite' for quite sometime since 1950s [3, 5, 6]. However, in 2004, the experimental realization of creating a stable structure of two dimensional (2D) graphene from the three dimensional (3D) graphite [4] brought graphene into the limelight of materials research as the potential alternative to the silicon-based electronics.

So what makes graphene so interesting? The answer lies in some extraordinary properties of graphene. First, graphene fits in perfectly for the need of 'nano' devices because it is the thinnest material with a highly stable two-dimensional structure. Secondly, graphene has an extremely high charge carrier mobility even at ambient conditions, 200×10^3 cm^2 V^{-1} s^{-1} at a carrier density of 10^{12} cm^{-2} [7, 8], which remains uninfluenced by temperature, electrical or chemical doping. The possibility of tuning charge carriers continuously from electron to hole [9], which is known as ambipolar field effect, also makes graphene an interesting contender for the device fabrications.

The reason of these exotic properties lies in the fact that the charge carriers in graphene imitate relativistic particles. Hence, they are described by Dirac equation with zero rest mass and effective Fermi velocity $v_F \approx 10^6$ m s^{-1} [10]. This relativistic nature is reflected in remarkable graphene properties like anomalous quantum Hall effects (QHE) [11, 12], minimum quantum conductivity [13, 14] and Klein tunneling [15]. Ballistic transport is also feasible in graphene due to its high carrier mobility and long mean free path, which is suitable from the electronic device point of view.

Although graphene has zero carrier density near the Dirac points, it does not have a band gap and the use of graphene in digital electronics is restricted due to the occurrence of minimum quantum conductivity. This leads to a very poor I_{on}/I_{off} ratio $\sim 10^1 - 10^2$ [16], which is not suitable for transistor applications. Hence it is necessary to manipulate the properties of graphene. Among the various attempts that have been made to introduce a semiconductor gap in graphene and modify its properties [17–26], creating defects are of particular interest. The nature and type of defects in graphene have been discussed extensively by Castro Neto *et al.* [10] and Banhart *et al.* [27]. Both intrinsic and extrinsic defects are possible in graphene. In particular, graphene is prone to

form vacancy defects [28, 29]. Such defects can affect the electronic structure and hence transport properties of graphene [26, 30–32].

The lack of band gap in graphene also prompted scientists to investigate other alternative two dimensional materials with possible band gaps. There exist a large number of layered crystalline solid-state materials with weak inter layer interaction from which a stable single layer 2D materials can be extracted [33]. These family of "beyond graphene" 2D materials can be classified further in smaller sub-classes such as 2D allotropes (graphyne, borophene, germanene, silicene, stanene, phosphorene), compounds (graphane, hexagonal boron nitride, germanane, transition metal dichalcogenides, etc.) [17, 21, 34–44]. Transition metal dichalcogenides were well known for quite sometimes [45] and Frindt *et al.* have shown that a few and single layer of metal dichalcogenides can be mechanically and chemically exfoliated from the van der Walls layered metal dichalcogenides [46, 47]. However, the potential of these 2D materials became apparent after an extraordinary research interest in graphene. Many of the 2D materials that had not been considered to exist have been synthesized using state-of-the-art experimental technologies. These 2D materials can be used in various wide range of applications due to their interesting electronic and structural properties, which are quite different from their bulk counterpart [48–53].

However, to use these various properties in commercial electronic devices, the 2D materials have to be prepared in a scalable way. In today's available experimental techniques, chemical vapor deposition method has become one of the first choices to make large scale fabrication of 2D materials. Nonetheless, defects such as edges, heterostructures, grain boundaries, vacancies, interstitial impurities are quite common in CVD prepared samples [27, 54–56]. These defects can be easily observed using various experimental techniques e.g., transmission electron microscopy (TEM) or scanning tunneling microscopy (STM) [57, 58]. Generally, these defects influence the properties of pristine materials. Hence it is important to investigate and thoroughly understand the role of defects either for avoiding their formation or for deliberate engineering. Sometimes defects can have destructive effects on device properties [54]. However, in nano scale, defects can introduce new functionalities, which can be beneficial for applications [59, 60].

A parallel approach in modifying graphene properties due to absence of band gap, is to build a hybrid material involving graphene and other 2D materials. Among other alternative 2D materials [48], hexagonal boron nitride (h–BN) appears to be a perfect candidate in this regard. Hexagonal boron nitride is isoelectronic to graphene, has similar lattice constant (only ~ 1.6 % mismatch), yet having different band structure than graphene, which leads to a complementary electronic structure [49, 61]. *Ab-initio* theoretical calculations on these hybrid materials reveal opening of a variable band gap [62–64], carrier induced magnetism [65], minimum thermal conductance [66] and interfacial electronic reconstruction [67, 68]. Controlled experimental synthesis of planar

hybrid structure of hexagonal boron nitride and graphene sheets with tunable separate graphene and h–BN regions [69–71] expands a great possibility of device fabrication, e. g., 2D field-effect transistors [72]. *Graphane*, hydrogenated graphene, is also a very good choice of making hybrid structures with graphene. These hybrid structures of graphene/*graphane* can mimic the properties of graphene nanoribbons [73–77]. Hence these materials can be useful in various potential applications.

In this thesis, we have employed *ab-initio* density functional theory based methods to investigate the influence of defects and impurities on the properties of 2D materials, such as graphene, silicene (2D sheet of silicon), 2D transition metal dichalcogenides, hybrid structures of graphene/*graphane* and graphene/h-BN. We have also looked into the opportunities of forming magnetic nanostructures on these interface structures, defected graphene, edge reconstructed zigzag graphene nanoribbons, etc. Transport properties of graphene and silicene in presence of various kinds of defects have been studied to identify defect-specific signatures. The effects of defects on gas sensing properties of graphene and on functionalization of graphene using Fe and F have been discussed.

The thesis is arranged in three parts – Part I, II, and III. Part I of the thesis contains two chapters – Introduction in Chapter 1 and brief formalism of density functional theory and computational methods in Chapter 2. The Part II of the thesis, summary of the results, also contains two chapters – Chapter 3 and Chapter 4. Chapter 3 consists of short summaries on the results obtained involving impurities in 2D systems whereas the effects of defects are discussed in Chapter 4. Finally the last part of the thesis, Part III, contains final remarks on the thesis. Here also two chapters are the constituents of this part. The discussions about final conclusions and outlooks are contained in Chapter 5. Last but not the least, Chapter 6 contains the summary of this thesis in Swedish language. For more detailed results and discussion, readers are encouraged to read the original research papers and manuscripts attached at the end of the thesis.

2. Theoretical Methods

This is the Construct. It is our loading program. We can load anything from clothes, to weapons to training simulations. Anything we need.

— Morpheus, The Matrix

Electrons and nuclei are the fundamental particles that determine the physical and chemical characteristics of materials. The atomic and molecular properties such as magnetic, optical, transport and crystal structures of materials are crucially dependent on the respective electronic structure. Therefore, determination of the electronic structure has always been in the focus of condensed matter physics and chemistry community. However, solutions of the electronic structure are not straight forward due to the fact that the electronic interactions in matter are quantum mechanical in nature and the complexity of describing them in a quantum mechanical system increases significantly with the increasing number of the electrons . This bottleneck leads to the branch of physics called "many-body physics".

2.1 Many body problem

The state of a many particle system is described by all electron wave function, $\psi(\{\vec{r}_i, \vec{R}_\alpha\}, t)$, which in general depends on position and time. The dynamics for non-relativistic systems are controlled by a time-dependent Schrödinger equation

$$i\hbar \frac{\partial \psi}{\partial t} = \hat{H}\psi \,. \tag{2.1}$$

$\hat{H}$, the Hamiltonian, represents the total energy operator and has the following form for a many body system, which consists of a number of interacting electrons and nuclei

$$\hat{H} = -\frac{\hbar^2}{2m_e}\sum_i \nabla_i^2 - \sum_\alpha \frac{\hbar^2}{2M_\alpha}\nabla_\alpha^2 - \sum_i \sum_\alpha \frac{Z_\alpha e^2}{|\vec{r}_i - \vec{R}_\alpha|}$$
$$+ \sum_i \sum_{j>i} \frac{e^2}{|\vec{r}_i - \vec{r}_j|} + \sum_\alpha \sum_{\beta>\alpha} \frac{Z_\alpha Z_\beta e^2}{|\vec{R}_\alpha - \vec{R}_\beta|}, \tag{2.2}$$
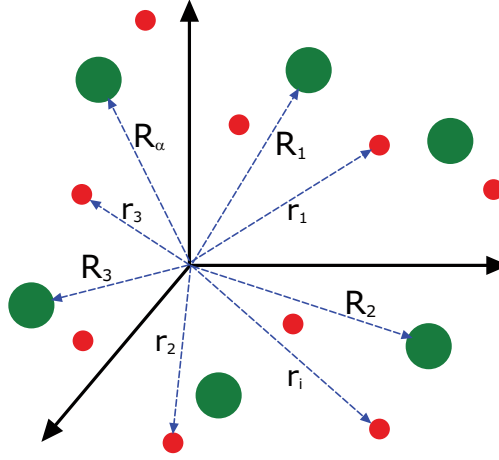
Figure 2.1. Schematics of instantaneous positions of atoms and electrons in a many body system. Small (red) and big (green) circles represent electrons and nuclei respectively. Size of the circles are not in scale.

where m_e and M_α are the mass of electron and α^{th} nucleus respectively, and $\vec{r}_i$, $\vec{R}_\alpha$ are the position of ith electron, α^{th} nucleus respectively as depicted schematically in Fig. 2.1. Z_α is the atomic number of the corresponding nucleus. The first and the second term of the equation 2.2 are the kinetic energy of the electrons and nuclei, respectively. The remaining three terms are the potential energy due to the Coulomb interaction between electron-nucleus, electron-electron and nucleus-nucleus, respectively. The Hamiltonian does not contain any explicit time dependent term. Therefore it is possible to write the wave function as a simple product of a spatial and a time-dependent parts, $\psi\left(\{\vec{r}_i, \vec{R}_\alpha\}, t\right) = \phi_E\left(\{\vec{r}_i, \vec{R}_\alpha\}\right) e^{-iEt}$, which leads to a simpler time-independent form of equation 2.1

$$\hat{H}\psi = E\psi\,, \tag{2.3}$$

where E is the total energy of the system.

However, solving the Schrödinger equation in this form is limited to a very small number of systems. Thus, to be applicable for all types of systems, approximations need to be incorporated. The first approximation utilizes the fact that the nuclei are $\sim 10^3$ times heavier compared to the electrons and thus their motion are significantly slower than the electronic motion. Thus it is plausible that on the time scale at which the nuclei move, the electrons very rapidly adapt to the instantaneous position of the configuration of nuclei. Therefore

the nuclei wave functions are independent of the electronic coordinates, and the wave function of the system can be split into the product of nuclei and electronic terms. This separation of electronic and nuclear motion is known as the Born-Oppenheimer approximation [78]. Thus the Hamiltonian can be separated into the nuclei part and the electronic part can be written as follows,

$$\hat{H}_e = -\frac{\hbar^2}{2m_e} \sum_i \nabla_i^2 - \sum_i \sum_\alpha \frac{Z_\alpha e^2}{|\vec{r}_i - \vec{R}_\alpha|} + \sum_i \sum_{j>i} \frac{e^2}{|\vec{r}_i - \vec{r}_j|} . \qquad (2.4)$$

The nuclei-nuclei interaction, $\sum_\alpha \sum_{\beta>\alpha} \frac{Z_\alpha Z_\beta e^2}{|\vec{R}_\alpha - \vec{R}_\beta|}$, is treated classically by the Ewald method. The total energy of the system is then calculated by adding this nuclei-nuclei interaction.

Even after this approximation, the solution of the Schrödinger equation is not easy because of the two following reasons,

1. The number of electrons in solid, $N \sim 10^{23}$. Therefore, total 4N variables require to describe the many-body electronic wave function.
2. The motion of an electron in solids is affected by the presence of other electrons through electron-electron correlation term $\sum_i \sum_{j>i} \frac{e^2}{|\vec{r}_i - \vec{r}_j|}$.

Therefore, to obtain any feasible solution, different schemes have been devised to approximate the many-body problem.

The first approach to solve the problem was introduced by Hartree by constructing the many electron wave function as a product of single electron wave functions. Solving using the variational principle, single particle Hamiltonian equations (Hartree equations) can be found. These equations are similar to the Schrödinger equation with an effective 'Hartree' potential. However, this approach does not consider antisymmetric description of the fermionic wave function.

Hartree-Fock formalism incorporated this fact by constructing many body electron wave function in a Slater determinant form. By using a variational method, similar Hamiltonian equations can be obtained. However, this formalism introduces an extra potential, named as exchange potential, along with the Hartree potential. This formalism is quite successful for small finite systems. However, it does not incorporate any electron correlation effect and thus remains inaccurate.

Both Hartree and Hartree-Fock methods are wave function based. Therefore, they are computationally expensive for large system sizes. The wave function is a very complicated quantity which cannot be measured experimentally. It depends on 4N variables, three spatial and one spin variable for each N electrons. Electron density, a real quantity, has reduced degrees of freedom and thus it can reduce the computational expanses significantly, if used as variables. The use of electron density as variable to solve many body Schrödinger equation gives birth to Density Functional Theory, the most popular and versatile method in modern day condensed matter physics.

2.1.1 Density functional theory

As stated in the last paragraph, the core concept of Density functional theory (DFT) is that to use the electron density $n(\vec{r})$ as a means to reach a solution to the Schrödinger equation. Thomas and Fermi [79, 80] took the first attempt to obtain information about atomic and molecular systems using electron density. They used a quantum statistical model of electrons which considers only the kinetic energy of the electrons. Contributions coming from the nuclear-electron and electron-electron were treated in a classical way. In this model Thomas and Fermi derived a very simple expression for the kinetic energy based on non-interacting uniform electron gas density but excluding the exchange and correlation of electrons.

Dirac further extended this model by including exchange interaction term based on uniform electron gas [81] and modified the equation of kinetic energy. However, the simple approximations by both Thomas-Fermi and Dirac lacked accurate descriptions of electrons in a many body system, leading to its failure.

2.1.2 Hohenberg-Kohn theorems

The first strong foundation of DFT came from the formalism of Hohenberg-Kohn in 1964 [82]. Hohenberg and Kohn through their two theorems, first showed that the properties of interacting systems can be obtained exactly using the ground state electron density, $n_0(\vec{r})$. This formalism is the core concept of DFT and relies on the following two theorems[*],

Theorem I
For any system of interacting particles in an external potential $V_{ext}(\vec{r})$, the potential $V_{ext}(\vec{r})$ can be determined uniquely, except for a constant, by the ground state particle density $n_0(\vec{r})$

Theorem II
A universal functional for the energy $E[n]$ in terms of density $n(\vec{r})$ can be defined, valid for any external potential $V_{ext}(\vec{r})$. For any particular $V_{ext}(\vec{r})$, the exact ground state energy of the system is the global minimum value of this functional, and the density $n(\vec{r})$ that minimizes the functional is the exact ground state density $n_0(\vec{r})$

Following the two theorems, the total energy of the system can be written as,

$$E[n(\vec{r})] = F[n(\vec{r})] + \int V_{ext}(\vec{r})n(\vec{r})\,d\vec{r}. \qquad (2.5)$$

The functional $F[n(\vec{r})]$ has the following form

$$F[n(\vec{r})] = T[n(\vec{r})] + J[n(\vec{r})] + E_{ncl}[n(\vec{r})], \qquad (2.6)$$

---

[*]The statements of the two theorems are directly taken from the book titled "Electronic Structure: Basic Theory and Practical Methods" written by Richard M. Martin. [83]

where $T[n(\vec{r})]$ is the kinetic energy of the interacting system, $J[n(\vec{r})]$ is the Hartree term, the classical Coulomb interaction between electrons. $E_{ncl}[n(\vec{r})]$ is the non-classical electrostatic contributions coming from self-interaction, exchange (i.e., antisymmetric nature of electrons), and electron correlation effects.

Since the functional $F[n(\vec{r})]$ does not depend on the external potential, it has to be same for any system. If the exact form of $F[n(\vec{r})]$ were a known and simple function of $n(\vec{r})$, then the ground state energy and density in an external potential can easily be determined by the minimization of a functional, which is a function of the three-dimensional density. However, the complexities of many electron system remain in finding the accurate form of the universal functional $F[n(\vec{r})]$. The two Hohenberg-Kohn theorems do not provide any solution to determine the exact form of the functional.

2.1.3 Kohn-Sham formalism

Kohn and Sham, in their article [84], gave a practical approach to obtain the unknown universal functional that we discussed previously. The main idea of Kohn-Sham formalism was to replace the kinetic energy of the interacting many-body system (T) with the exact kinetic energy of a non-interacting system (T_S) built from a set of orbitals, i. e., one electron functions while keeping the same ground state density. The non-interacting kinetic energy term T_S can be written as,

$$T_S = -\frac{1}{2} \sum_{i=1}^{occ} \langle \psi_i | \nabla^2 | \psi_i \rangle \ . \tag{2.7}$$

According to the Kohn-Sham formalism, the total energy functional can be written as

$$E[n(\vec{r})] = \int V_{ext}(\vec{r}) n(\vec{r}) d\vec{r} + T_S[n(\vec{r})]$$
$$+ \frac{1}{2} \iint \frac{n(\vec{r})n(\vec{r}_2)}{|\vec{r} - \vec{r}_2|} \, d\vec{r} \, d\vec{r}_2 + E_{xc}[n(\vec{r})] \,, \tag{2.8}$$

where, V_{ext} is the external potential, T_S is the kinetic energy term. The third term in the equation is Hartree term, which is the classical electrostatic energy of the electrons. E_{xc} is known as the *excahnge-correlation energy* and can be defined using equations 2.5, 2.6 and 2.8 as,

$$E_{xc} = (T[n(\vec{r})] - T_S[n(\vec{r})]) + E_{ncl}[n(\vec{r})]$$
$$= T_C[n(\vec{r})] + E_{ncl}[n(\vec{r})] \,. \tag{2.9}$$

Hence, E_{xc} is the functional which contains the residual part of true kinetic energy, T_C, and the non-classical electrostatic contributions, E_{ncl}. The minimization of Kohn-Sham energy functional in equation 2.8, with respect to the

electron density $n(\vec{r})$ yields a Schrödinger-like Kohn-Sham equation,

$$H_{KS}(\vec{r})\psi_i(\vec{r}) = \left[-\frac{1}{2}\nabla^2 + V_{KS}(\vec{r})\right]\psi_i(\vec{r}) = \varepsilon_i\psi_i(\vec{r}), \qquad (2.10)$$

showing that the non interacting particles are moving in an effective potential, V_{KS}. The potential, V_{KS}, can be written as,

$$V_{KS}(\vec{r}) = V_{ext}(\vec{r}) + V_H(\vec{r}) + V_{xc}(\vec{r}), \qquad (2.11)$$

where, V_{ext} is the external potential, V_H is the Hartree potential and V_{xc} is the *exchange-correlation* potential. The form of these potentials are expressed as,

$$V_H = \int \frac{n(\vec{r}_2)}{|\vec{r} - \vec{r}_2|} \, d\vec{r}_2 \ \text{ and } \ V_{xc} = \frac{\delta E_{xc}[n(\vec{r})]}{\delta n(\vec{r})}.$$

ψ_i are the eigenfunctions and ε_i are the corresponding eigenvalues. The ground state electron density can be calculated as follows,

$$n(\vec{r}) = \sum_{i=1}^{occ} |\psi_i(\vec{r})|^2. \qquad (2.12)$$

The newly calculated electron density can be used to calculate new effective potential self-consistently. From the equation 2.7 and 2.10, the kinetic energy of the non-interacting system can be written as

$$T_S[n(\vec{r})] = \sum_{i=1}^{occ} \varepsilon_i - \int V_{KS}(\vec{r})n(\vec{r}) \, d\vec{r}, \qquad (2.13)$$

and then substituting the value of $T_S[n(\vec{r})]$ in equation 2.8, the total energy can be obtained by the following expression,

$$E[n(\vec{r})] = \sum_{i=1}^{occ} \varepsilon_i - \frac{1}{2} \iint \frac{n(\vec{r})n(\vec{r}_2)}{|\vec{r} - \vec{r}_2|} \, d\vec{r} \, d\vec{r}_2$$
$$- \int V_{xc}(\vec{r})n(\vec{r}) \, d\vec{r} + E_{xc}[n(\vec{r})], \qquad (2.14)$$

where, the total energy functional $E[n(\vec{r})]$ does not depend on the external potential $V_{ext}(\vec{r})$.

2.2 Exchange-correlation approximations

The Kohn-Sham formalism we have discussed previously is exact. If the form of E_{xc} is exactly known, then this formalism will yield exact ground state of

the interacting many-body system. However, the explicit form of the E_{xc} functional is not known and approximations to the form of E_{xc} have to be introduced. Hence, the quality of DFT calculations solely depend on the accuracy of chosen approximation to E_{xc}. Depending on the level of approximation, different forms of E_{xc} can be constructed. Two of the most common used approximations are local density approximation (LDA) and generalized gradient approximation (GGA).

2.2.1 Local density approximation (LDA)

Hohenberg and Kohn proposed the first ever form of exchange-correlation energy [82]. In this proposal, the *exchange-correlation* energy density $\varepsilon_{xc}^{uni}[n(\vec{r})]$ of a system is considered to be the same as associated with the uniform electron gas with a density $n(\vec{r})$. Using this assumption, the form of *exchange-correlation* functional can be written as below,

$$E_{xc}^{LDA}[n(\vec{r})] = \int n(\vec{r})\varepsilon_{xc}^{uni}[n(\vec{r})]\, d\vec{r}, \qquad (2.15)$$

where $\varepsilon_{xc}^{uni}[n(\vec{r})]$ denotes the *exchange-correlation* energy density of a uniform electron gas with density $n(\vec{r})$ calculated locally at a point $\vec{r}$. This is the most basic form of *exchange-correlation* functional and works quite well for many systems. ε_{xc} has two contributions, exchange, ε_x, and correlation, ε_c. The analytical form of ε_x can be evaluated from the approximation of Hartree-Fock exchange and originally derived by Dirac [81] as follows,

$$\varepsilon_x[n(\vec{r})] = -\frac{3}{4}\left(\frac{3\,n(\vec{r})}{\pi}\right)^{\frac{1}{3}}. \qquad (2.16)$$

However, the explicit analytical form of ε_c is not known. Ceperley and Alder obtained highly accurate numerical values of ε_c using quantum Monte-Carlo simulations of the homogeneous electron gas [85]. On the basis of this numerical values, using advanced interpolation techniques, various analytical expressions of ε_c were presented by different authors e.g., Perdew-Zunger [86] Perdew-Wang [87].

Despite its simplicity, LDA seems to work fine particularly for the molecular properties determination such as equilibrium structures, harmonic frequencies or charge moments, properties of itinerant magnetic systems [88]. LDA, however, underestimates the lattice constant of the materials [89] and produce relatively higher binding energies i. e., over binding.

2.2.2 Generalised-Gradient approximation (GGA)

Generalized-Gradient approximation was developed to overcome some of the limitations of LDA. In this method, the *exchange-correlation* density depends

both on the electronic density, $n(\vec{r})$, and on the gradient of the electronic density, $\nabla n(\vec{r})$. GGA *exchange-correlation* energy is obtained by modifying the LDA energy density:

$$E_{xc}^{GGA}\left[n(\vec{r})\right] = \int n(\vec{r})\varepsilon_{xc}^{uni}\left[n(\vec{r})\right] F_{xc}\left[n(\vec{r}), \nabla n(\vec{r})\right] d\vec{r} \qquad (2.17)$$

where $F_{xc}[n(\vec{r}), \nabla n(\vec{r})]$ is an analytic function, known as the enhancement function. Perdew and Wang provided a parameter free form of exchange enhancement factor [90]. It was later on modified by Perdew, Burke and Ernzerhof to give a simplified form, known as PBE after their names. Using a parametrized form of the homogeneous electron gas correlation energy and a gradient dependent term, the GGA correlation can also be constructed [91, 92].

GGA corrected the over binding problem of LDA. It also improves the results in structural properties, bulk phase stability, atomic and molecular energies, phase transitions, cohesive energies, etc. However, GGA does not provide much improvements over LDA in describing itinerant magnetic systems [88].

Although both LDA and GGA are successful in describing some material properties, both of them underestimate the band gap of semiconductors and insulators. The dependence of energy functional $E(N)$ on the number of electrons, N, creates the problem for both LDA and GGA. $E(N)$ and its derivative $\partial E/\partial N$, both are continuous for an integral value of N. However, the derivative of the exact functional might be discontinuous with respect to number of electrons. This contributes to the band gap by a significant amount [93, 94].

2.3 Strong correlation effect: LDA+U

Both LDA and GGA failed to describe the band gap problem in materials, where electrons are localized and strongly interacting, such as Mott insulators, transition metal oxides and rare earth compounds. The problem lies in the fact that both LDA and GGA fail to reproduce orbital energies[†].

A correction to both the LDA and the GGA energy functional has been introduced by incorporating explicit Coulomb interaction of localized electrons (U) in a Hartree-Fock (HF) like approach. This method is commonly known as the LDA+U correction where "LDA+U" stands for LDA- or GGA calculation coupled with orbital dependent interaction. In LDA+U approach, the electrons are divided in two different subsystems,

   I. *localized electrons* for which explicit Coulomb interaction is taken into account.

   II. *wide band electrons*, which are described by the LDA.

[†]Orbital energy $\Rightarrow \varepsilon_i = \partial E/\partial n_i$, $\quad n_i$ is the orbital occupation number.

Instead of density, density matrix elements $\{\rho\}$ were used to define the corrected energy functional as follows,

$$E^{LDA+U}\left[n^{\sigma}(\vec{r}),\{\rho^{\sigma}\}\right] = E^{LDA}\left[n^{\sigma}(\vec{r})\right] + E^{U}\left[\{\rho^{\sigma}\}\right] - E_{dc}\left[\{\rho^{\sigma}\}\right],$$

(2.18)

where, $n^{\sigma}(\vec{r})$ is the charge density for electrons with spin σ. The first term is the Kohn-Sham energy functional. The second term describes the HF correction to the functional.

The third term in equation 2.18 is known as double counting term. This term has to be subtracted from the total energy functional because the energy functional given by LDA already consists of a contribution from the electron-electron interaction.

2.4 Periodic solids

The above formalism discussed so far is applicable for systems with finite number of electrons, e. g., atoms and molecules. However, in solid systems the calculation of electronic structure faces problems because of infinitely many electrons. This can be overcome by employing the periodicity of the solids. In a single particle context, the electrons feel an effective potential, V_{KS}, provided by the KS equation.

$$H_{KS}(\vec{r})\psi_i(\vec{r}) = \left[-\frac{1}{2}\nabla^2 + V_{KS}(\vec{r})\right]\psi_i(\vec{r}) = \varepsilon_i\psi_i(\vec{r}).$$

(2.19)

where V_{KS} follows the lattice periodicity,

$$V_{KS}\left(\vec{r}+\vec{R}\right) = V_{KS}\left(\vec{r}\right),$$

(2.20)

$\vec{R}$ is the translational vector, which is same as the periodicity of the Bravis lattice. According to Bloch theorem [95], in a periodic crystal, the crystal momentum $\vec{k}$ is a good quantum number and enforces a boundary condition for the KS wave function, $\psi_{\vec{k}}$,

$$\psi_{\vec{k}}\left(\vec{r}+\vec{R}\right) = e^{i\vec{k}\cdot\vec{R}}\psi_{\vec{k}}(\vec{r}),$$

(2.21)

where $\psi_{\vec{k}}(\vec{r})$ is the *Bloch* wave function,

$$\psi_{\vec{k}}(\vec{r}) = e^{i\vec{k}\cdot\vec{r}}u_{\vec{k}}(\vec{r}).$$

(2.22)

$u_{\vec{k}}(\vec{r})$ is a periodic function of lattice, $u_{\vec{k}}(\vec{r}) = u_{\vec{k}}(\vec{r}+\vec{R})$. The single particle wave function can be expanded in a complete basis set $\phi_{i,\vec{k}}(\vec{r})$, satisfying Bloch's criteria for periodic boundary condition.

$$\psi_{n\vec{k}}(\vec{r}) = \sum_i c_{i,n\vec{k}}\,\phi_{i,\vec{k}}(\vec{r}),$$

(2.23)

where $c_{i,n\vec{k}}$ is the Fourier expansion coefficient. Using equation 2.23 in equation 2.19 and multiplying from the left by $\left\langle \phi_{i,\vec{k}} \right|$, the following equation can be written,

$$\sum_j \left[\left\langle \phi_{i,\vec{k}} \middle| H_{KS} \middle| \phi_{j,\vec{k}} \right\rangle - \varepsilon_{n\vec{k}} \left\langle \phi_{i,\vec{k}} \middle| \phi_{j,\vec{k}} \right\rangle \right] c_{j,n\vec{k}} = 0 \ . \tag{2.24}$$

The first and second term in equation 2.24 represents the effective Hamiltonian matrix element and the overlap matrix element respectively. By solving the following secular equation,

$$det \left[\left\langle \phi_{i,\vec{k}} \middle| H \middle| \phi_{j,\vec{k}} \right\rangle - \varepsilon_{n\vec{k}} \left\langle \phi_{i,\vec{k}} \middle| \phi_{j,\vec{k}} \right\rangle \right] = 0 \ . \tag{2.25}$$

the eigenvalues $\varepsilon_{n\vec{k}}$ and the expansion coefficients $c_{i,n\vec{k}}$ can be obtained.

2.5 Basis sets: Plane waves

Considerable number of numerical difficulties still affect the implementation of single particle KS equation. This is due to the fact that the behavior of the wave function is quite different in different regions of space, i. e., in the core region and in the valence region. Hence, a complete basis set is needed to describe the wave function in all the regions of space.

There are several possible choices for the basis sets depending on the system studied and required accuracy – plane waves (PW), linearized augmented plane waves (LAPW), localized atomic like orbitals e.g., linear muffin-tin orbitals (LMTO), linear combination of atomic orbitals (LCAO), etc. In this section, we will briefly discuss about plane wave basis sets as most of the results discussed in the thesis are obtained using plane wave based methods.

The lattice periodic function, $u_{j,\vec{k}}(\vec{r})$, can be expressed in a Fourier series as follows

$$u_{j,\vec{k}}(\vec{r}) = \sum_{\vec{G}} c_{j,\vec{G}} \, e^{i\vec{G}\cdot\vec{r}} \ , \tag{2.26}$$

where $\vec{G}$ is the reciprocal lattice vector, the $c_{j,\vec{G}}$ are the plane-wave expansion coefficients, and $\vec{G}.\vec{r} = 2\pi m$, m being an integer and $\vec{r}$ is the real space lattice vector. Hence the KS orbitals can be expressed in a linear combination of plane waves as

$$\psi_{j\vec{k}}(\vec{r}) = \sum_{\vec{G}} c_{j\vec{k}} \left(\vec{G} \right) \times \frac{1}{\sqrt{\Omega}} e^{i(\vec{k}+\vec{G})\cdot\vec{r}} \ , \tag{2.27}$$

where $c_{j\vec{k}}$ are the expansion coefficient of the wave function in plane wave basis set $e^{i(\vec{k}+\vec{G})\cdot\vec{r}}$ and $\vec{G}$ are the reciprocal lattice vectors. It is convenient

that the states are normalized and obey periodic boundary condition in a large volume Ω, which is allowed to go infinity. Hence, the pre-factor, $1/\sqrt{\Omega}$, serves as the normalization factor. $\vec{k}$ is the Bloch wave vector. Hence, the KS equation in the notation of Bloch state can be written as

$$\left(-\frac{\hbar^2}{2m_e}\nabla^2 + V_{KS}(\vec{r})\right)\psi_{j\vec{k}}(\vec{r}) = \varepsilon_{j\vec{k}}\psi_{j\vec{k}}(\vec{r}) \tag{2.28}$$

Using equation 2.27 into equation 2.28, and multiplying from the left with $e^{-i(\vec{k}+\vec{G}').\vec{r}}$ and integrating over $\vec{r}$ we get the matrix eigenvalue equation as:

$$\sum_{\vec{G}'}\left(\frac{\hbar^2}{2m_e}\left|\vec{k}+\vec{G}\right|^2\delta_{\vec{G}'\vec{G}} + V_{KS}\left(\vec{G}-\vec{G}'\right)\right)c_{j\vec{k}}\left(\vec{G}\right) = \varepsilon_{j\vec{k}}c_{j\vec{k}}\left(\vec{G}\right) \tag{2.29}$$

In this form, the kinetic energy is diagonal, and the potential, V_{KS} is described in terms of their Fourier transforms. The solution of equation 2.29 is obtained by diagonalization of a Hamiltonian matrix whose matrix elements $H_{\vec{k}+\vec{G},\vec{k}+\vec{G}'}$ are given by the terms in brackets on the left hand side. The size of the matrix (sum over $\vec{G}'$) is determined by the choice of the cutoff energy $E_{cut} = \frac{\hbar^2}{2m_e}\left|\vec{k}+\vec{G}_{max}\right|^2$, and will be intractably large for systems that contain both valence and core electrons. This is a severe problem, but it can be overcome by the use of the pseudopotential approximation, discussed in the next section.

2.6 Pseudopotential

The pseudopotential approximation deals with the valence electrons of the system. These rely on the fact that the core electrons are tightly bound to their host nuclei, and only the valence electrons are involved in chemical bonding. The wave functions of the core electrons do not change significantly with the environment of the parent atom. Therefore it is possible to combine the core potential with the nuclear potential, and only deal with the valence electrons separately. This method is called Frozen-Core-Approximation (FCA). The physical justification is that almost all the interesting chemical aspects are primarily related to the outermost (valence) electrons of an atom. The standard pseudopotential model via FCA is schematically shown in Fig. 2.2.

The atomic wave functions are orthogonal to each other. Hence, to maintain the orthogonality in the neighborhood of nucleus, i. e., in the core region, the valence electron wave functions must oscillate rapidly. As a result, the kinetic energy of the valence electrons in the core region is quite large and it cancels out with the potential energy coming from the Coulomb potential. It makes the
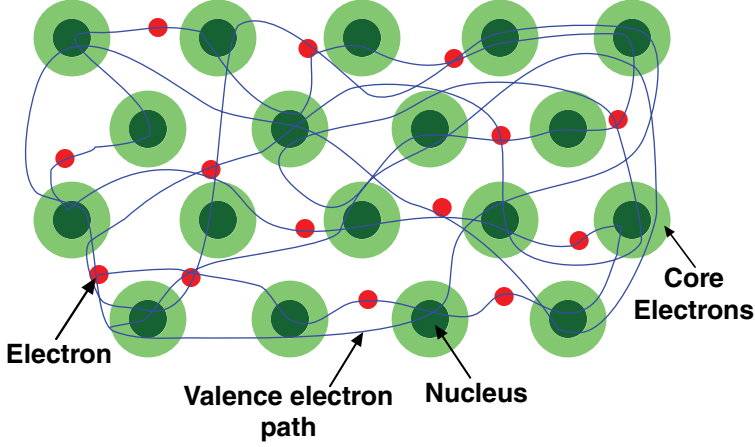
Figure 2.2. Schematic diagram of Frozen Core Approximation (FCA) for the standard pseudopotential model. The ion cores composed of the nuclei and tightly bound core electrons are treated as chemically inert. Dark green, light green and red circles, respectively representing the nucleus, the core electrons and the valence electrons are for illustrations only (sizes of the circles are not in scale).

valence electron more weakly bound than the core electron. Therefore, one can introduce an effective pseudopotential, which will be weaker than the strong Coulomb potential in the core region. The pseudo wave function will be node-less and vary smoothly in the core region – so that it can replace the valence electron wave function. A schematic representation of pseudopotential method is presented in Fig. 2.3.

To explain the construction of pseudopotential, following the operator approach [96], let us assume an atom with Hamiltonian $\hat{H}$, core states $|\psi_c\rangle$ with core energy eigenvalues E_c and valence states $|\psi_v\rangle$ with valence energy eigenvalues E_v. Therefore, the Schrödinger equation can be written as

$$\hat{H}\,|\psi_i\rangle = E_i\,|\psi_i\rangle \ , \tag{2.30}$$

where 'i' stands for both core and valence states. The goal is to obtain smoother valence states in the core region. A smoother pseudo-state $|\psi^{ps}\rangle$ can be defined as

$$|\psi_v\rangle = |\psi^{ps}\rangle + \sum_c |\psi_c\rangle\,\alpha_{cv} \ , \tag{2.31}$$

where the summation is over core states and α_{cv} is the expansion coefficient. Now, the valence state has to be orthogonal to all of the core states. Hence

$$\langle\psi_c|\psi_v\rangle = 0 = \langle\psi_c|\psi^{ps}\rangle + \alpha_{cv} \ . \tag{2.32}$$
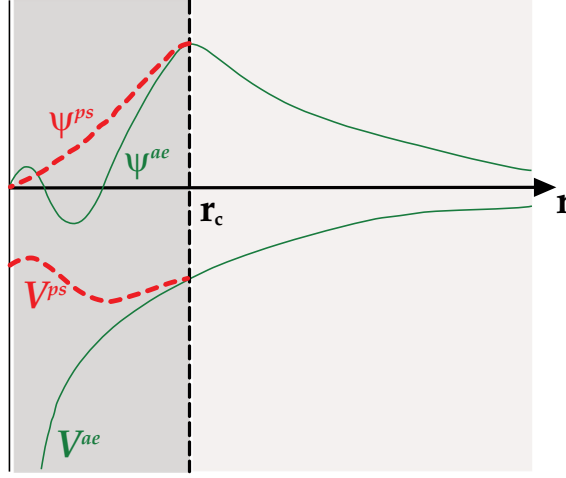
Figure 2.3. Schematic representation of a pseudopotential V^{ps} (red dashed line) and corresponding pseudo wave function ψ^{ps} (red dashed line). The pseudo wave function is node-less and it matches exactly with all electron wave function ψ^{ae} (green solid line) outside of a cut-off radius r_c . This introduces a much softer pseudopotential compared to all electron potential $V^{ae} \sim \frac{-Z}{r}$.

Inserting the value of α_{cv} from equation 2.32 into equation 2.31,

$$|\psi_v\rangle = |\psi^{ps}\rangle - \sum_c |\psi_c\rangle \langle\psi_c|\psi^{ps}\rangle \ . \tag{2.33}$$

Substituting $|\psi_v\rangle$ both side in equation 2.30 and rearranging we get the following equation.

$$\hat{H} |\psi^{ps}\rangle + \sum_c (E_v - E_c) |\psi_c\rangle \langle\psi_c|\psi^{ps}\rangle = E_v |\psi^{ps}\rangle$$

$$\Rightarrow \quad \hat{H}^{ps} |\psi^{ps}\rangle = E_v |\psi^{ps}\rangle \ . \tag{2.34}$$

The above equation 2.34 is analogous to the Schrödinger equation with pseudo-Hamiltonian,

$$\hat{H}^{ps} = \hat{H} + \sum_c (E_v - E_c) |\psi_c\rangle \langle\psi_c| \ , \tag{2.35}$$

and pseudopotential

$$\hat{V}^{ps} = \hat{V}_{eff} + \sum_c (E_v - E_c) |\psi_c\rangle \langle\psi_c|$$

$$= \hat{V}_{eff} + \hat{V}_{nl} \ , \tag{2.36}$$

29

where

$$\hat{V}_{eff} = \text{attractive Coulomb potential}$$

$$\text{and} \quad \hat{V}_{nl} = \sum_c \left(E_v - E_c\right) |\psi_c\rangle \langle\psi_c| \ . \tag{2.37}$$

The energies described by the pseudo wave functions in equation 2.34, are the same as that of the original valence states. The effect of the additional potential $\hat{V}_{nl}$ is localized to the core region and it is repulsive in nature. Hence, it will cancel part of the strong attractive nuclear Coulomb potential $\hat{V}_{eff}$, so that the resulting sum will be a weaker pseudopotential and resulting pseudo wave function will be node-less.

2.6.1 Projector augmented wave

Projector augmented wave (PAW) method is an all electron method. It combines the elegance of plane-wave pseudopotential method with the augmented wave method. This method was first introduced by Blöchl [97]. As adapted in pseudopotential method, PAW approach consists of a simpler energy and potential independent basis but it retains the flexibility of augmented wave method. PAW method consists of a linear transformation (Im) linking an oscillatory true all electron single particle KS wave function $|\psi_n\rangle$ with a computationally convenient auxiliary wave function, $|\tilde{\psi}_n\rangle$,

$$|\psi_n\rangle = \text{Im} \, |\tilde{\psi}_n\rangle \ , \tag{2.38}$$

where, the index n is a cumulative index representing band, $\vec{k}$-point and spin. Using the variational principle with respect to the auxiliary wave function, the KS equation can be transformed as follows,

$$\text{Im}^\dagger \, H \, \text{Im} \, |\tilde{\psi}_n\rangle = \text{Im}^\dagger \, \text{Im} \, |\tilde{\psi}_n\rangle \varepsilon_n \ , \tag{2.39}$$

where $\text{Im}^\dagger \, H \, \text{Im} = \tilde{H}$ is the pseudo Hamiltonian and $\text{Im}^\dagger \, \text{Im} = \tilde{O}$ is the overlap operator. The purpose of this transformation is to avoid the nodal structure of a true wave function close to the nucleus within a certain radius from the core, r_c (See Fig. 2.3). The wave function inside the core region is modified by Im and hence defined as follows,

$$\text{Im} = 1 + \sum_R S_R \ . \tag{2.40}$$

S_R is the difference between auxiliary and true single particle KS wave function while R is the atom site index. S_R acts within an augmented space, which is defined by a cutoff radius, $r_c \in R$.

The core wave function is treated separately as it does not expand beyond augmented region. The energy and the electron density of the core electrons

in a material is approximated with an isolated atom calculations[‡]. Hence, the operator Im acts on valence wave function and it can be expressed within the augmented region as follows,

$$\psi(\vec{r}) = \sum_{i \in R} \phi_i(\vec{r}) c_i \, . \tag{2.41}$$

Here $\phi_i(\vec{r})$ represent the partial wave solutions for Schrödinger equation for an isolated atom and c_i are the expansion coefficients associated with it. In this way, using the transformation Im, the partial wave $|\phi_i\rangle$ is one-to-one mapped locally to an auxiliary partial wave $|\tilde{\phi}_i\rangle$.

$$|\phi_i\rangle = (1 + S_R)\left|\tilde{\phi}_i\right\rangle \quad \text{for } i \in R \tag{2.42}$$

$$S_R\left|\tilde{\phi}_i\right\rangle = |\phi_i\rangle - \left|\tilde{\phi}_i\right\rangle \tag{2.43}$$

This local transformation implicitly enforces a condition that the partial waves $|\phi_i\rangle$ and $\left|\tilde{\phi}_i\right\rangle$ have to be pairwise identical beyond $r_c \in R$:

$$\phi_i(\vec{r}) = \tilde{\phi}_i(\vec{r}) \quad \text{for } i \in R \text{ and } |\vec{r} - \vec{R}_R| > r_{c,R} \tag{2.44}$$

Using auxiliary partial wave basis, any arbitrary auxiliary wave function can be formed within the augmented region,

$$\tilde{\psi}(\vec{r}) = \sum_{i \in R} \tilde{\phi}_i(\vec{r}) c_i = \sum_{i \in R} \tilde{\phi}_i(\vec{r}) \left\langle \tilde{p}_i \mid \tilde{\psi} \right\rangle \tag{2.45}$$

where, the projector operator $|\tilde{p}_i\rangle$ satisfies the following two constraints,

$$\sum_{i \in R} \left|\tilde{\phi}_i\right\rangle \langle \tilde{p}_i| = 1 \quad \dots \quad \text{the completeness relation} \tag{2.46}$$

$$\left\langle \tilde{\phi}_i \mid \tilde{p}_j \right\rangle = \delta_{i,j}; \text{ for } i, j \in R \quad \dots \quad \text{the orthogonality relation} \tag{2.47}$$

In terms of auxiliary and the true partial waves, the transformation operator can be written as,

$$\text{Im} = 1 + S_R \sum_i \left|\tilde{\phi}_i\right\rangle \langle \tilde{p}_i|$$

$$= 1 + \sum_i \left(|\phi_i\rangle - \left|\tilde{\phi}_i\right\rangle\right) \langle \tilde{p}_i| \tag{2.48}$$

[‡]The *frozen-core approximation*

where the sum runs over the partial waves corresponding to all atoms. Hence, the true wave function can be re-obtained as follows,

$$\left|\psi\right\rangle = \left|\tilde{\psi}\right\rangle + \sum_i \left(\left|\phi_i\right\rangle - \left|\tilde{\phi}_i\right\rangle\right)\left\langle\tilde{p}_i|\tilde{\psi}\right\rangle$$

$$= \left|\tilde{\psi}\right\rangle + \sum_R \left(\left|\psi_R^1\right\rangle - \left|\tilde{\psi}_R^1\right\rangle\right) \tag{2.49}$$

where,

$$\left|\psi_R^1\right\rangle = \sum_{i\in R} \left|\phi_i\right\rangle \left\langle\tilde{p}_i|\tilde{\psi}\right\rangle \tag{2.50}$$

$$\left|\tilde{\psi}_R^1\right\rangle = \sum_{i\in R} \left|\tilde{\phi}_i\right\rangle \left\langle\tilde{p}_i|\tilde{\psi}\right\rangle \tag{2.51}$$

As a consequence of this transformation, the wave function is spatially separated out into different parts. Inside the core region, the wave function is expressed with the partial waves consisting of nodal structure, i. e., $\left|\tilde{\psi}_R\right\rangle = \left|\tilde{\psi}_R^1\right\rangle$. This gives the true wave function $\left|\psi_R\right\rangle$ merging to $\left|\tilde{\psi}_R^1\right\rangle$. Beyond the core region, both the auxiliary wave functions and the true wave functions are identical, i. e., $\left|\psi_R\right\rangle = \left|\tilde{\psi}_R\right\rangle$.

Although the PAW method consists of few approximations, e. g., the *frozen-core approximation*, expansion of auxiliary wave function with finite number of plane waves, etc., this method computes to the full wave function, charge and spin densities with a much simpler basis set.

Part II:
Summary of the Results

3. The Effect of Impurities

Curiouser and curiouser!

— Lewis Carroll, Alice in Wonderland

In this chapter, the effect of impurities on the properties of graphene and related hybrid structures, which have been presented in Papers I–IV, will be discussed in general. As mentioned in the introduction, the studies are motivated by the necessity of altering the semi-metallic nature of pure graphene to open a band gap. Keeping this aspiration in mind, in the following sections we will discuss: 1) the effects of metallic impurities on two dimensional hybrid structures of graphene and graphane, 2) exploiting the edge properties of graphene nanostructures using quantum confinement, 3) formation and diffusion of metallic nanostructures on planar hybrid interfaces of graphene and hexagonal boron nitride (h-BN) and 4) 3D quasiperiodic heterostructure of graphene and h-BN to break sublattice symmetry.

We have studied the above mentioned systems by performing electronic structure calculations using plane wave basis sets employing PAW method as implemented in the VASP [98, 99] code.

3.1 Graphene/*Graphane* interfaces with magnetic impurities

The interaction of magnetic impurities (Fe adatom in this case) with the hybrid structures of graphene and *graphane* has been discussed in Paper I. *Graphane*, one of the important compounds of "beyond grpahene" family of 2D materials, is a hydrogenated graphene structure. In this structure, one hydrogen atom is attached to each carbon atom giving rise to an insulating system with sp^3 bonds. This material was first predicted by *ab-initio* theory [17] and latter experimentally synthesized [21]. In graphene, a semimetal to metal to insulator transition has been observed by varying the concentration of hydrogen atoms [100].

Patterning graphene with partial hydrogenation (hybrid graphene/*graphane* interface) can alter the properties of graphene e.g., in introducing conducting channels, band gap opening, and magnetically coupled interfaces [100–105]. These graphene/*graphane* interfaces can mimic the edge properties of zigzag or armchair graphene nanoribbons [73–77] and can be used as a potential material in the field of spintronics research. It has been shown that magnetic

properties of transition metal doped zigzag graphene nanoribbons (ZGNR) are much more robust as compared to the magnetic moments arising from the edge geometry [106]. Antiferromagnetic coupling between two edges of ZGNR can be observed with Fe termination at the edges [107]. Hence, it will be interesting to study the effect of Fe adatom, as a representative of magnetic impurities, in these hybrid graphene/*graphane* interface structures.

3.1.1 Channel structures of graphene/*graphane* interface
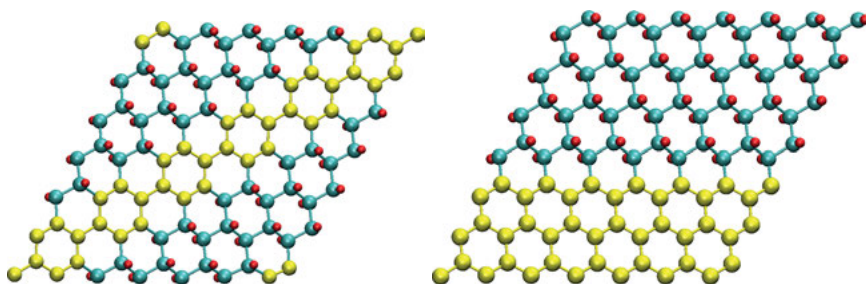
Figure 3.1. Decoration of hydrogen (left) along the diagonal of the unit cell leading to an "armchair" channel and (right) along the edge of the unit cell leading to a "zigzag" channel. In the figure, yellow (light shaded in print) balls are bare carbon atoms, turquoise (dark shades in print) balls are hydrogenated carbon atoms and red (small dark in print) balls are H atoms. For both armchair and zigzag channels, the nanoribbons are 3-rows wide. Reproduced with permission from Paper I. Copyright © 2012 American Physical Society.

We have considered two different graphene/*graphane* hybrid structures - i) where the hydrogen atoms are removed along the diagonal of the *graphane* part to create armchair graphene/*graphane* superlattices, and ii) where the hydrogen atoms are removed along the edge of *graphane* part to create zigzag graphene/*graphane* superlattices. In left and right panel of Fig. 3.1, we have shown a schematic picture of these two structures respectively, for a specific width of three rows. The "armchair channel" is nonmagnetic and has a width-dependent band gap. However, the "zigzag channel" interfaces are magnetic. In our simulations, we have used three different widths of channels.

3.1.2 Single Fe adatom impurity

We have placed the Fe adatom at different places on the channels described above and optimized the geometries to find out the stable adsorption site. The calculated formation energy indicates that the preferred site for Fe adsorption in the armchair channel is the hollow site inside the graphene region, equidistant from the interface. However, Fe adatom prefers to bind at a hollow site

Table 3.1. *Width dependent energies and magnetic moments of the channel systems with a single Fe impurity. E_b, μ_{total} and μ_{Fe} denote the binding energy of Fe, total magnetic moment of the system and magnetic moment on Fe site respectively. Reproduced with permission from Paper I. Copyright © 2012 American Physical Society.*

		Single Fe atom		
Channel Type	Channel Width	E_b (eV)	μ_{total} (μ_B)	μ_{Fe} (μ_B)
Armchair	3-rows	1.6	2.0	1.99
	5-rows	1.10	2.06	2.10
	7-rows	0.80	2.00	1.98
Zigzag	3-rows	1.38	2.1	2.5
	5-rows	1.42	2.01	2.55
	7-rows	1.45	2.01	2.56

closer to the interface in the zigzag channel. This different behavior is due to the antiferromagnetic nature of the edge coupling and the position of Fe adatom is slightly asymmetric with respect to the surrounding hexagon due to the stretching of underlying carbon bonds.
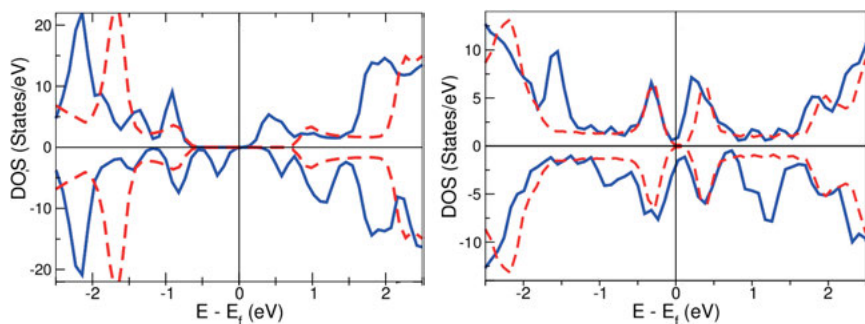
Figure 3.2. (Left Panel) Spin-polarized DOS for single Fe atom placed in the three-row "armchair" channel. Total DOS with (blue solid line) and without (red dashed line) Fe. (Right Panel) Spin-polarized DOS for single Fe atom placed in the three-row "zigzag" channel. Total DOS with (blue solid line) and without (red dashed line) Fe. Reproduced with permission from Paper I. Copyright © 2012 American Physical Society.

In Table 3.1, we have shown the energies and magnetic moments of the Fe atom placed on these channels. Analysis of the binding energies as a function of channel widths reveals that with increasing width, the binding energy remains almost constant in the zigzag channel, while it decreases in the armchair channel. Total magnetic moment for all the systems are $\sim 2.0 \, \mu_B$, similar to the value of total magnetic moment of an Fe adatom substitutionaly placed in

graphene [108]. However, the onsite local moments differ in both channels. The value of onsite local moment is ~ 0.5 μ_B higher in the zigzag channel as compared to the armchair channel. Our calculation indicates that, in the zigzag channel, the binding energy of Fe adatom is higher by ~ 0.2 eV as compared to the pristine graphene [108]. This suggest that the mixed sp^2–sp^3 character increases the binding energy of Fe in the zigzag channel.
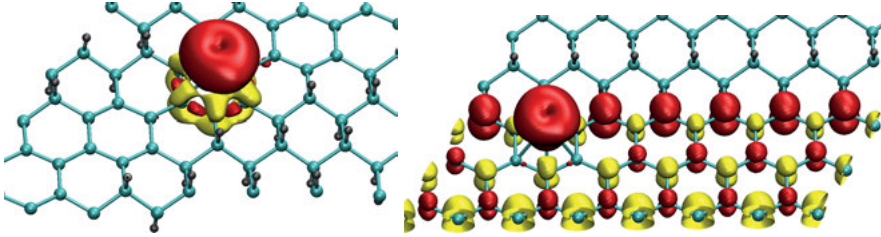

Figure 3.3. Spin-density plot of single Fe atom on the three-row "armchair" (left panel) and "zigzag" (right panel) channel respectively. Red (dark shade in print) is positive spin density and yellow (light shade in print) is negative spin density. Reproduced with permission from Paper I. Copyright © 2012 American Physical Society.

Total density of states for a single Fe adatom placed on a three-row armchair (zigzag) channel have been shown in the left (right) panel of Fig. 3.2. The analysis of site projected DOS (see Paper I for more details) shows that spin-down $d_{z^2-r^2}$ orbitals of Fe atom induce states just below the Fermi energy and reduce the gap quite significantly. In higher width channel structures, similar features can be observed. However, in contrast to the armchair channel, a finite density of states can be observed near the Fermi energy for the zigzag channel. These states are mainly originating from spin-down $d_{z^2-r^2}$ orbitals of Fe atom along with the p_z orbitals of the bare carbon atoms at the interface. Contribution in the spin-up peak just below the Fermi energy is predominantly coming from the delocalized p_z orbitals of bare edge carbon atoms and from the carbon atoms surrounding the Fe atom.

The spin density plots of Fe adatom adsorbed in three-row armchair and zigzag channel have been shown in Fig. 3.3 left and right panels, respectively. From the analysis, we find that for the armchair channel, most of the spin-up densities are localized on Fe. The d orbitals of Fe atom interact with the p_z orbitals of the surrounding carbon atoms and cause an induced negative magnetic moment on the carbon atoms. On the other hand, in the zigzag channel, delocalized spin density can be observed and till fourth nearest neighbor, the effect of Fe adatom can be seen. These interactions reduce the onsite magnetic moments on carbon atoms with a maximum value of 15% on the nearest site. In this channel, due to the interactions of delocalized electron density, only three carbon atoms surrounding the Fe atom get induced negative moment.

38

Effect of spin-orbit coupling

We have also included the spin orbit coupling term in the Hamiltonian in order to calculate the orbital moments and magnetic anisotropy energies (MAEs). Here, MAE refers to magnetocrystalline energy originating from spin-orbit coupling. We have neglected the contribution of shape anisotropy. MAE is defined as $\Delta E = E^{hard} - E^{easy}$. In the armchair channel, the orbital moment of Fe atom is 0.09 μ_B which is ~ 0.04 μ_B higher than the bulk Fe in bcc phase. The magnetic anisotropy energy is 19 meV and it has an in-plane easy axis of magnetization. In case of zigzag channel, with spin orbit coupling, the total magnetic moment increases as some of the carbon atoms contribute ($\sim$ 0.1 μ_B) additively. Here, the magnetic anisotropy energy with in-plane easy axis is about 4 meV per Fe atom, which is smaller compared to the value in the armchair channel. The in-plane orbital moment is 0.1 μ_B in this case. It is to be noted that our calculated MAEs for Fe adatom on both channels are quite high as compared to the MAE of bulk bcc Fe, which is of the order of 1 μeV.

3.1.3 Magnetic interactions between two Fe atoms

In this subsection, we have discussed the results of two magnetic impurities in the two channels. In Table 3.2, we have tabulated the binding energies of Fe atoms, the total magnetic moments, the onsite magnetic moments on Fe atoms, and exchange energies. We have considered various possible Fe-Fe distances for both the channels. In the armchair channel, the two Fe atoms are weakly interacting which is clear from the small fluctuations of binding energies of the Fe atoms with the variation of distances. Hence, the exchange energies are also small. The analysis of total DOS shows a gap in the spin-up channel just below the Fermi energy and a gap in the spin-down channel just above the Fermi energy. It shows a possibility of creating a "spin gapless semiconductor" in narrower armchair channel occurs.

On the other hand, in the zigzag channel, the binding energies and the magnetic moments are distance dependent. The two Fe atoms form a dimer for the smallest Fe-Fe distance. For a Fe-Fe distance of 5.08 Å in all the widths, total magnetic moment decreases with increasing width of channels. It is due to the fact that, the position of the second Fe atom with respect to the first Fe atom introduces negative spin moments on the surrounding carbon atoms. See Paper I for more details.

3.2 Edge reconstructed graphene nanoribbons with H and Fe functionalization

Another approach towards the opening of band gap in the graphene is to use structural confinement. Graphene nanoribbons are the one dimensional counterpart of 2D graphene. These nanoribbons have various fascinating properties

Table 3.2. *Width-dependent energies and magnetic moments of the channel systems with a pair of Fe atoms with possible Fe-Fe distances. The distances between two Fe atoms (d) are in Ångstroms, and the binding energies (E_b) of Fe in are in electron volts. Total magnetic moment of the systems (μ_{total}) and the magnetic moments on the two Fe atoms (μ_{Fe}) are in the units of Bohr magneton (the local magnetic moments on two Fe atoms are separately shown by a slash in between them) and the exchange energies ($E^{ex} = E^{FM} - E^{AFM}$) are in electron volts. Reproduced with permission from Paper I. Copyright © 2012 American Physical Society.*

|		Two Fe atoms in the channel				
Type	Width	d_{Fe} (Å)	E_b (eV)	μ_{total} (μ_B)	μ_{Fe} (μ_B)	E^{ex} (eV)
armchair	3-rows	4.38	3.13	4.02	1.98/2.01	0.009
		8.77	3.18	4.01	1.99/1.99	0.001
	5-rows	4.38	2.25	4.11	2.10/2.10	0.018
		8.77	2.19	4.08	2.11/2.12	0.008
	7-rows	4.38	1.75	4.06	2.04/2.03	0.014
		8.77	1.64	4.01	2.01/2.01	0.016
zigzag	3-rows	2.17	4.12	5.96	2.98/2.98	0.457
		5.08	2.67	7.0	2.59/2.6	0.058
		7.60	2.67	4.26	2.42/2.43	0.038
	5-rows	2.17	4.09	5.89	3.01/3.01	0.834
		5.08	2.73	4.14	2.53/2.53	NA
		7.60	2.80	4.06	2.51/2.51	NA
	7-rows	2.17	4.10	5.82	3.01/3.01	0.795
		5.08	2.80	4.07	2.53/2.54	NA
		7.60	2.87	4.02	2.52/2.52	NA

e.g., band gap opening, quantum confinement effect, magnetism at the edges, etc [109–111]. Depending on the edge geometry, different types of properties can be observed such as metallic behavior in zigzag graphene nanoribbons and semiconducting behavior in armchair graphene nanoribbons [22, 23]. However, confining the geometry in one dimension to produce graphene nanoribbons creates unsaturated edges. These edges are quite active and are prone to structural edge reconstruction [74]. Forming pentagon-heptagon pair at the edges is one of the proposed structural rearrangement of graphene nanoribbon. These deformations are quite similar to the Stone-Wales defect observed in 2D graphene. These reconstructed zigzag graphene nanoribbon (henceforth called "reczag") geometry has also been experimentally verified using transmission electron microscopy [77]. *Ab-initio* calculations indicate that reczag structure has lower total energy as compared to the normal zigzag graphene nanoribbon by 0.35 eV/Å.

In this section and in Paper II, we have discussed the edge reconstruction of graphene nanoribbons and functionalization using H and Fe atoms.

3.2.1 Stability of reconstructed structure

(a)   (b)
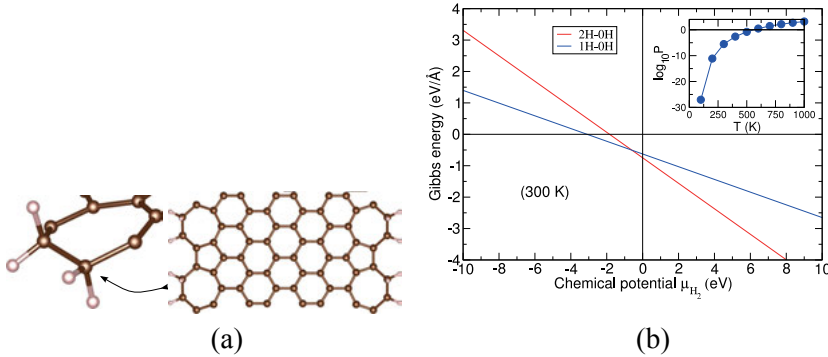
Figure 3.4. (a) Reconstructed edge GNR with 2H termination. Brown balls are C atoms and white balls indicate H atoms. The close-up of the edge structure is also shown; (b) Gibbs free energy calculated for 12 rows-reczag. Both 1H and 2H terminations with respect to bare reczag are presented. In the inset, transition pressures as a function of temperatures are shown. P^0 is the reference pressure taken to be 0.1 bar. Reprinted from Paper II, Copyright © 2012, with permission from Elsevier.

Even after reconstruction at the edges, reczag graphene nanoribbons have dangling bonds and these bonds need to be saturated. We have considered edge termination of each carbon atom by one (1H) and two (2H) hydrogen atoms. The optimized structure of a reczag graphene nanoribbon with 2H termination

41

has been shown in Fig. 3.4(a). The bond length analysis of optimized structures reveal substantial changes at the edges. In reczag graphene nanoribbons, without edge termination, the bond length between two carbon atoms at the edges is ~ 1.25 Å and two edge carbon atoms form triple bond in between them. In 1H termination, the C-C bond length increases to 1.43 Å and for 2H termination, due to twisted edge geometry, the C-C bond length increases further to 1.58 Å (see Fig. 3.4(a)). However, in all the structures, C-C bond lengths in the middle of the ribbon are ~ 1.42 Å, which is similar to the C-C bond length in bulk graphene. Although 1H termination is a planar structure with sp^2 hybridization, 2H termination gives rise to a buckled and twisted edge structure with sp^3 bonds. Phonon calculations on normal 2H terminated reczag graphene nanoribbons structure show unstable phonon modes with hydrogen atom displacement towards the twisted direction. For more details on phonon calculations, see Paper II.

We have calculated the formation energies of 1H and 2H terminated reczag graphene nanoribbons with respect to the bare reczag graphene nanoribbons. The formation energies have been defined as follows

$$E_f = E(G2H) - [E(G1H) + n * E(H_2)],$$

where $E(G2H)$ and $E(G1H)$ are the total energies per edge for 2H and 1H terminated reczag graphene nanoribbons respectively. $E(H_2)$ is the calculated energy for a gaseous H_2 molecule. The number of H_2 molecules used to compensate the uneven number of H atoms is denoted by n. From our calculations, it can be seen that at T = 0K, 1H terminations form spontaneously for reczag graphene nanoribbons geometry which are in contrast to normal zigzag nanoribbon [112]. The formation energies also reveal that the 2H terminated reczag graphene nanoribbons structures are more stable than 1H terminated reczag graphene nanoribbons structures.

We have also calculated Gibbs formation energy as a function of μ_{H_2} to investigate the effect of finite temperature and high gas pressure following the formulations of Wassmann *et al.* [113],

$$G_{H_2} = \frac{1}{2L}[E_{H_2} - (\frac{N_H}{2})\mu_{H_2}],$$
$$G_{H_1} = \frac{1}{2L}[E_H - (\frac{N_H}{2})\mu_{H_2}],$$
$$E_{H_2} = E(G2H) - [E(G0H) + 4E(H_2)],$$
$$E_H = E(G1H) - [E(G0H) + 2E(H_2)],$$
$$\mu_{H_2} = H^0(T) - H^0(0) - TS^0(T) + k_BT \, ln(\frac{P}{P^0}),$$

where μ_{H_2}, H, S, P and k_B are the chemical potential, enthalpy, entropy, pressure and Boltzmann constant respectively. N_H is the number of H atoms attached at the edge. For entropies and enthalpies, the values are taken from

the tabular data presented in Ref. [114]. We have taken 0.1 bar as the reference pressure, P^0, according to the tabular data. Total energies for 2H, 1H and bare reconstructed nanoribbons and hydrogen molecule are indicated as $E(G2H)$, $E(G1H)$, $E(G0H)$ and $E(H_2)$ respectively. The calculated values of normalized Gibbs energy at 300K have been shown in Fig. 3.4(b). Normalization was done by a factor of 2L, where L is the length of unit cell.

From Gibbs energy calculations, it is observed that at room temperature under low hydrogen pressure (less than 10^{-6} bar), 1H terminated edge can be stabilized over 2H terminated edge. However, after 10^{-6} bar hydrogen pressure at room temperature, 2H terminated edges are favored. The required transition pressure* as a function of temperature has been shown in the inset of Fig. 3.4(b). The negative values of $log_{10}P$ over a long range of temperature indicates the formation of 2H terminated reczag graphene nanoribbons under low pressure. Hence, following the previous work by Bhandary *et al.* (Ref. [112]) one can conclude that compared to zigzag edges, reczag graphene nanoribbons are structurally more stable and thus can accommodate higher concentration of H.

The total density of states calculation for 1H and 2H terminations show finite density of states at the Fermi energy. These states mainly originate from the p_z orbitals of the C atoms next to the edge C atoms. However, the saturation of C-C bonds at the edges results into the loss of magnetic moment for both 1H and 2H terminated reczag graphene nanoribbons.

3.2.2 Fe termination at the edges
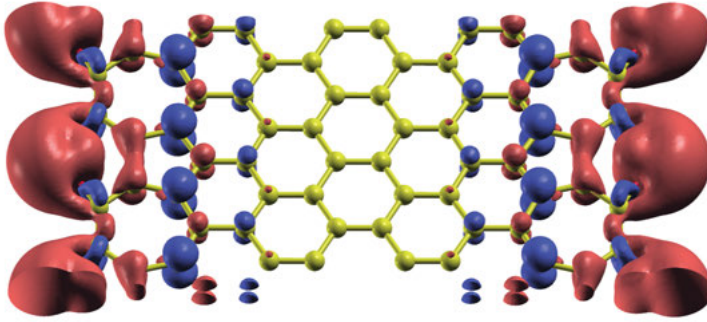
Figure 3.5. Spin density isosurfaces of 8-rows Fe doped reczag edge for a FM coupling across the edges. Red and blue colors represent spin-up and spin-down densities respectively. Reprinted from Paper II, Copyright © 2012, with permission from Elsevier.

---

*The amount of hydrogen pressure which favored formation of the 2H terminated edges over the 1H terminated edges.

We have decorated the reconstructed edges of the nanoribbons with magnetic Fe atoms in order to introduce magnetism and study possible magnetic interactions via graphene lattice. The formation energy E_f of Fe atom at the edge is calculated using the following formula,

$$E_f = E(met_N + reczag) - [N * E(met) + E(reczag)],$$

where $E(met_N + reczag)$ is the total energy of metal+reconstructed edge graphene nanoribbon, $E(reczag)$ is the total energy of reczag graphene nanoribbon and $E(met)$ is the energy of the Fe calculated in its bulk bcc phase. N is the number of Fe atoms in the cell. Analysis of geometry and formation energy reveals that the most stable Fe adsorption site is in between the two heptagons with a calculated formation energy of 2.6 eV. The Fe adsorption causes structural modification at the edges only.

However, the effect of Fe atom at the edge is quite long range which can be easily observed in spin density isosurface plots as shown in Fig. 3.5. The onsite local magnetic moment of Fe atom is 3.5 μ_B, which is quite high and the Fe atom induces opposite moment to the C atoms to which it is bonded. We have also calculated exchange couplings by calculating the total energy difference between FM and AFM coupling across the edges. The exchange coupling starts with a strong ferromagnetic coupling for four rows and gradually decreases as the width increases and finally changes to antiferromagnetic coupling after eight rows. This similar oscillatory exchange coupling behaviors have been in Fe and Co decorated armchair graphene nanoribbons [115].
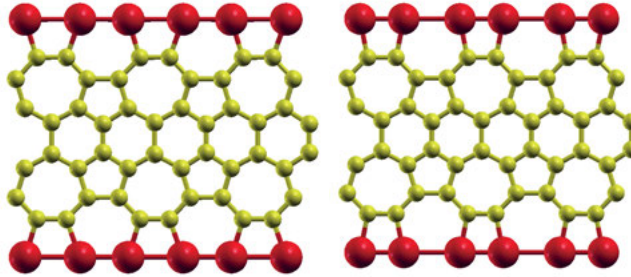
Figure 3.6. The structures of two dimerized chains indicated as Dimer 1 (left) and Dimer 2 (right) in Table 3.3. In the figure, red and yellow balls indicate Fe and C atoms respectively. Reprinted from Paper II, Copyright © 2012, with permission from Elsevier.

We have also investigated the possibility of forming a dimerized chain along the nanoribbon edges. Here the Fe atoms bind to the edge carbon atoms of the heptagons. Two different dimer configurations are possible as shown in Fig. 3.6. The calculation of formation energies tabulated in Table 3.3 indicates

Table 3.3. *Formation energies (ΔE) of two types of Fe dimers in the chain with respective to non-dimerized structure. The corresponding bond lengths (short and long) of the Fe dimers are shown for the two structures shown in figure 3.6 along with the local magnetic moments at Fe sites. Reprinted from Paper II, Copyright © 2012, with permission from Elsevier.*

Dimer	ΔE (eV)	Fe-Fe distance 1 (Å)	Fe-Fe distance 2 (Å)	moment (μ_B)
1	-0.23	2.61	2.30	2.94
2	-0.29	2.77	2.14	2.94

that with increased Fe concentration dimerized chain formation along the edges of reczag graphene nanoribbons is promoted.

3.3 Diffusion and formation of Fe nanostructures on Graphene/h-BN interfaces

The role of 2D planar Graphene/h-BN interfaces on the designing of Fe nanostructures has been presented in Paper III. As discussed in the introduction, the planar graphene/h-BN hybrid sheets can be used to tune the band gap of graphene. For most electronic applications, the use of these 2D materials will involve contacts with metals. Hence a fundamental understanding of the interaction between metals (in the form of adatoms, clusters and thin films, etc.) and hybrid graphene/h-BN interfaces is quite important. Some limited attention has been given in the adsorption of 3d transition metal atoms on hybrid graphene/h-BN structure (1:1 composition of graphene and h-BN) sheets [116]. However, a lot of details about the systems still remain unanswered. Given this background, in this work, detailed adsorption and diffusion of a single and multiple Fe adatoms and their magnetic properties on a hybrid graphene/h-BN sheet have been studied. Diffusion barriers were calculated using the climbing image method within the nudged elastic band (NEB) formalism [117, 118].

3.3.1 Individual Fe adatoms

The structures with completely phase separated graphene and h-BN regions are energetically the most favorable arrangement for hybrid graphene/h-BN sheets [62–64]. So, a 64 atom hybrid graphene/h-BN supercell, where the graphene and h-BN regions forming separate domains and being joined by zigzag C–N and C–B interfaces, have been considered for the calculations. We have calculated the adsorption energies for a single Fe adatom placed at different inequivalent hexagonal sites on the 64-atom supercell (see Fig. 3.7). Adsorption energies at these sites and the heights of the Fe adatom from the
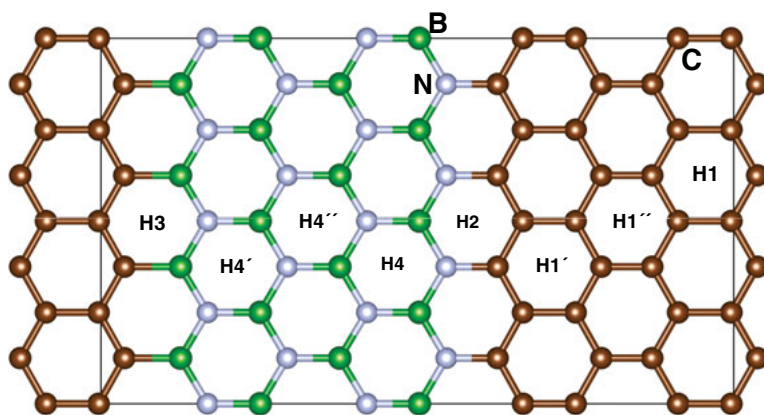
Figure 3.7. Hybrid sheet of graphene/hexagonal boron-nitride showing different symmetry sites considered for calculation of diffusion barriers. Black solid line represents the unit cell considered for the calculation. Brown, green and white balls represent carbon, boron and nitrogen atoms respectively. See text for more explanation. Reproduced with permission from Paper III. Copyright © 2013 American Chemical Society.

surface are mentioned in Table 3.4. We have used these relaxed positions as initial and final positions to carry out diffusion barrier calculations involving the NEB method. Among the hexagonal sites, H4′ turns out to be an unstable one. Our calculation shows that the H3 site at the C–B interface is much lower in energy than H4′ and hence prevents the formation of an energy barrier from going to H4′ to H3. So an adatom placed at this site moves to the neighboring H3 site at the C–B interface after relaxation. The analysis of adsorption energy (see Table 3.4) clearly shows that the H3 site at the C–B interface is the most favorable one followed closely by the H1 site.

Diffusion barriers between all the nearest neighbor hexagonal site (Fig. 3.7) were calculated in both directions using the NEB method. The calculated bar-

Table 3.4. *Adsorption energy and the heights of the Fe adatom (E_a) at different sites. The most stable site is marked in bold. See text for details. Reproduced with permission from Paper III. Copyright © 2013 American Chemical Society.*

Site	E_a (eV)	Height (Å)
H1	1.65	1.57
H1′	1.36	1.58
H1″	1.37	1.55
H2	0.89	1.65
H3	**1.74**	**1.72**
H4	0.39	1.62
H4″	0.57	1.90

Table 3.5. *Calculated diffusion barriers (in eV) along different paths on the hybrid graphene/h-BN sheet. Reproduced with permission from Paper III. Copyright © 2013 American Chemical Society.*

Path	Barrier	Path	Barrier	Path	Barrier
$H3 - H1$	0.34	$H1 - H3$	0.26	$H4'' - H4''$	0.21
$H2 - H1'$	0.1	$H1' - H2$	0.53	$H3 - H3$	0.6
$H1 - H1''$	0.75	$H1'' - H1$	0.53	$H2 - H2$	0.13
$H1 - H1$	0.32	$H1' - H1'$	1.08	$H1' - H1''$	1.3
$H1'' - H1''$	0.46	$H4 - H4$	0.17		

rier values are given in Table 3.5. The diffusion barriers are generally smaller in the h-BN region compared to the graphene region. This suggests that the Fe adatoms will be more mobile in the h-BN region.

The exact mechanism of diffusion at finite temperature can be complex [119]. The diffusion barrier may increase or decrease, or even show non-monotonic behavior with increasing temperature depending on the details of the diffusion mechanism and the vibrational modes at the saddle points in a given system. Rather than estimating diffusion barrier of the adatoms, we have studied their real-time dynamics on the sheet at finite temperatures through Born-Oppenheimer molecular dynamics (MD) simulations. We performed a number of simulations by placing a single Fe adatom at all the inequivalent hexagonal sites. The temperature was set at $T = 300$ K because most practical applications would be at ambient conditions. Our result shows that the Fe adatom can diffuse rather easily over the h-BN region compared to the graphene one. In our simulations, the Fe adatom remains stuck at a $H1'$ or a $H1''$ site and it could not cross the barrier at least for 15 ps and then moves out of these sites. If the Fe adatom is placed at a H2 site, it diffuses to $H1'$ and gets trapped. Starting from the H1 site, the Fe adatom moves back and forth between H1 and H3 before finally settling at a H3 site. For all other hexagonal sites, Fe adatom diffuses and eventually gets trapped at the H3 site at the C–B interface, consistent with the fact that H3 site has the highest adsorption energy.

Following the above discussions, there are two relevant questions that need to be answered. First, the nature of magnetic coupling between two Fe adatoms adsorbed at two different H3 sites along the C–B interface. Secondly, whether two such Fe adatoms remain stuck at two different H3 sites at a finite temperature or they diffuse along the H3-H3 path parallel to the C–B interface and form dimer. These will provide an overview into possible magnetic self-assemblies on this sheet. Our simulations show that a ferro-magnetic (FM) alignment of spins when the two Fe adatom occupy nearest neighbor H3 sites has the lowest energy. Both Fe adatoms have onsite magnetic moment $\sim 3~\mu_B$. The MD simulations up-to 30 ps show that the adatoms remain stuck at their respective H3 sites and only execute thermal oscillations around mean positions. This is also

evident from the fact that the diffusion barrier between two H3 sites is quite high (0.6 eV) as reported in Table 3.5. Hence, the H3 sites truly act as trapping sites for individual Fe adatoms diffusing on the hybrid graphene/h-BN sheets at the room temperature.
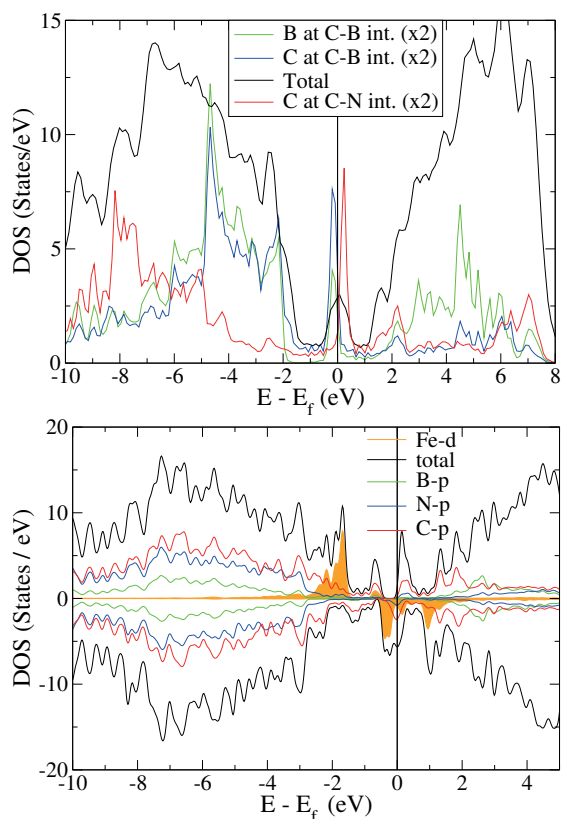
Figure 3.8. DOS for (top panel) pure hybrid grphene/h-BN sheet and (bottom panel) a Fe adatom adsorbed at C–B interface of hybrid graphene/h-BN sheet. Reproduced with permission from Paper III. Copyright © 2013 American Chemical Society.

The analysis of charge density of pure graphene/h-BN sheet shows that at the C–B interface, the charge density is not homogeneously distributed over the C–B bond whereas the C–N interface has a homogeneous charge distribution (π character originating from C and N p_z orbitals) over the C–N bond. This asymmetry in the distribution of charge density allows C–B interface to be more reactive.

The calculated DOS and atom projected DOS (pDOS) for a single Fe adatom trapped at a H3 site on a 64-atom hybrid graphene/h-BN sheet, shown in Fig. 3.8. For comparison, DOS and atom and site projected DOS of the pure sheet are also shown. For the sheet without Fe, the valence band states just below the gap come mainly from the C atoms bonded to B atoms at the C–B interface.

Conduction band states just above the gap come mainly from the C atoms at the C–N interface. States from both C–B and C–N interfaces appear in the gap of pure h-BN. In the presence of Fe, those states still persist, but appear only in the down-spin channel. The analysis of m_ℓ projected DOS reveals that for the C–B interface, Fe d_{xy} orbital hybridizes with B p_z orbital quite prominently. Also, Fe d_{z^2} orbital hybridizes with C p_z and N p_z orbitals. So, a relatively strong binding scenario has established. The up-spin channel with filled d-states does not contribute at the Fermi energy, yielding a half metallic solution. Fe has a magnetic moment of $2.6\ \mu_B$, whereas a few C atoms close to Fe possess small negative moments yielding a total magnetic moment of $2.0\ \mu_B$ in the unit cell. However, for the C–N interface, no significant hybridization (except a small one between Fe $d_{x^2-y^2}$ and B and C p_z orbitals) between Fe d orbitals and p orbitals of B/C/N is observed.

3.3.2 Multiple Fe adatoms

Now that we have gained some understanding of the finite temperature dynamics of isolated Fe adatoms and magnetic exchange coupling between two isolated Fe adatoms on the sheet, we now try to shed some light on the question of clustering and subsequent dynamics when more than one Fe adatom are deposited. Particularly striking was our finding that the H1′ site, in spite of having large barriers, do not trap Fe adatoms, which ultimately get stuck at the H3 sites and thus making finite temperature MD calculations for multiple Fe adatoms even more relevant. The analysis of MD simulations, where multiple Fe adatoms were placed either in the h-BN or graphene regions, shows that the Fe adatoms quickly form a cluster and then the cluster as a whole diffuses easily and finally gets stuck at the C–B interface. In experiments, one may not have such microscopic control during the deposition of Fe adatoms on the hybrid graphene/h-BN sheet. Also in view of the fact that CVD experiments produce domains of h-BN inside a graphene sheet, the adatoms are equally likely to land on either of the regions. To simulate that, we consider a large supercell with 128 atoms: 64 C, 32 B and 32 N atoms. These are divided into two graphene and two h-BN regions as shown in Fig. 3.9. Eight Fe adatoms are placed at eight hexagonal sites on this sheet at $t = 0$ in the following way. Two Fe adatoms are placed in each of the C–1 and C–2 regions, and two Fe adatoms each in the BN–1 and BN–2 regions.

Note that there is a C–B interface between C–1 and BN–1 regions (C–B–int1), a C–N interface between BN–1 and C–2 regions (C–N–int1), another C–B interface between C–2 and BN–2 (C–B–int2) and finally another C–N interface between BN–2 and C–1 (C–N–int2) due to the periodic boundary conditions. As shown in the second panel of Fig. 3.9, within 3 ps, all the four Fe adatoms in the BN–1 and C–1 regions form a Fe_4 cluster. The two Fe adatoms placed in the BN–1 region easily move towards the C–B–int1. At the
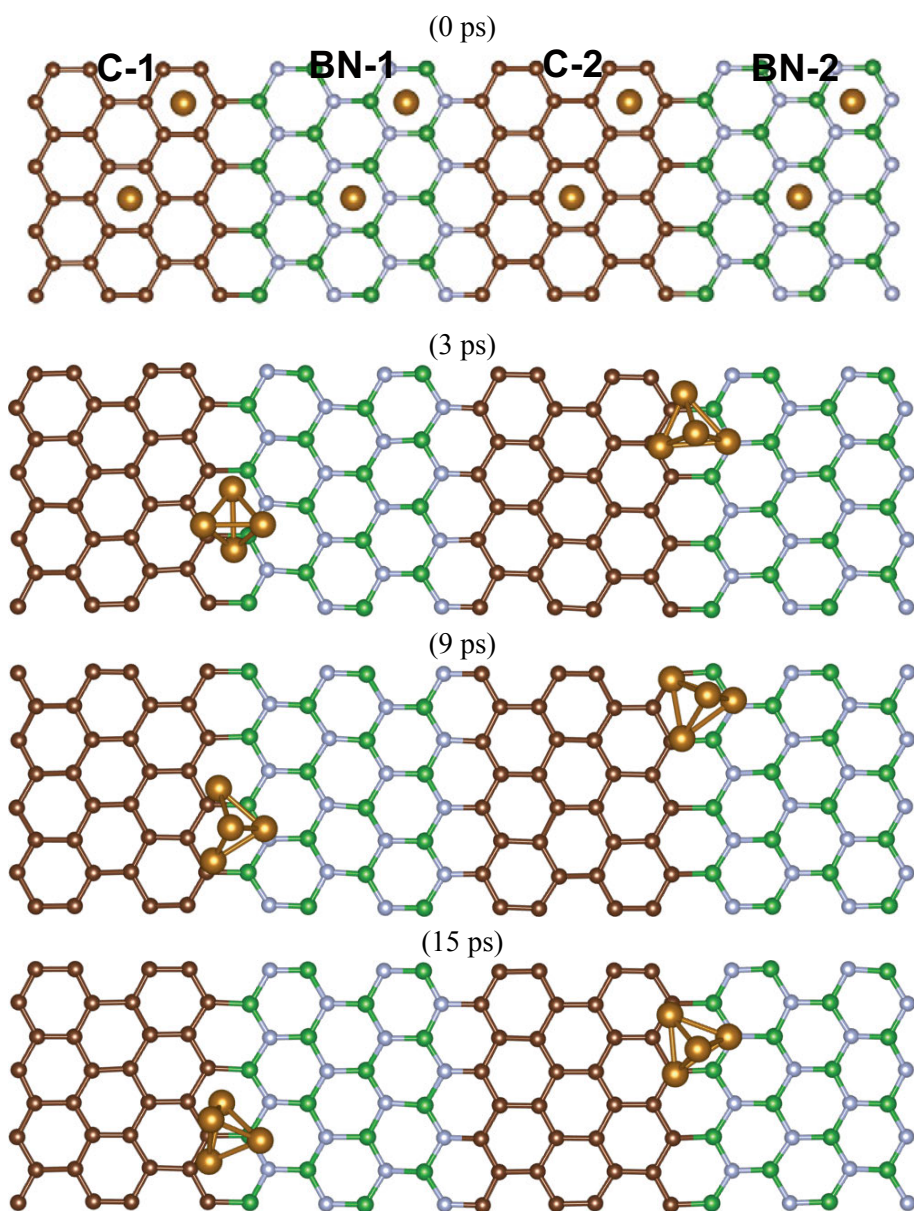
Figure 3.9. Time evolution of eight Fe adatoms on the BNC sheet. We placed two Fe atoms separated from each other on four patches of BN and Graphene. See text for discussions. Reproduced with permission from Paper III. Copyright © 2013 American Chemical Society.

Table 3.6. *Adsorption energies and the heights of Fe adatom (E_a) at different sites from PBE+U calculations. The most favorable site H3 is marked in bold. See text for details. Reproduced with permission from Paper III. Copyright © 2013 American Chemical Society.*

| Site	E_a (eV)	Height (Å)
H1	0.74	1.92
H1′	0.57	1.91
H1"	0.62	1.84
H2	0.58	1.91
H3	**1.11**	**1.96**
H4	0.14	2.21

same time the two Fe adatoms placed in the C–1 region also move towards the C–B–int1. Then these four Fe atoms forms a Fe_4 cluster and as a unit gets trapped at the C–B–int1 interface. Up to 15 ps simulation time, the cluster can be seen to be stuck there as shown in Fig. 3.9. Similarly, the other four Fe adatoms placed in the BN–2 and C–2 regions form a second Fe_4 cluster near the C–B–int2 interface (two Fe adatoms coming from BN–2 region and other two Fe adatoms coming from C–2 region) which gets trapped at the C–B–int2 interface.

3.3.3 Electron correlation effects

For Fe nanostructures, electron correlation effects are expected to be important because of narrow band widths of d-states of Fe. In order to check its effect in the dynamic and electronic properties of the Fe clusters on the hybrid graphene/h-BN sheet, we have used the PBE+U method. The adsorption energies of a single Fe adatom at different hexagonal sites are given in Table. 3.6. It is observed that the adsorption energies decrease at all the sites in presence of a finite U. The heights of the Fe adatom above the sheet expectedly increase with a decrease in hybridization, but the most stable adsorption site does not change. The effect of electron correlations is seen in the calculated diffusion barriers. With the PBE functional, the diffusion barrier between the H1′ and H1″ sites was 1.3 eV. Using PBE+U, the barrier drops to only ~ 0.12 eV. This is due to the weak hybridization between the adatom and the 2D sheet in presence of strong Coulomb interaction. This raises the question whether the Fe cluster would get trapped at the C-B interface even when electron correlations are included. To verify this we have performed MD calculations at $T = 300$ K with four Fe adatoms on a 64-atom hybrid graphene/h-BN sheet using the PBE+U method. Interestingly, the four Fe adatoms do form a cluster as before, and the cluster gets trapped at the C–B interface. Therefore, one

can safely conclude that the findings from PBE calculations are qualitatively similar in the case of PBE+U.

3.4 Quasiperiodic heterostructures with graphene and h-BN
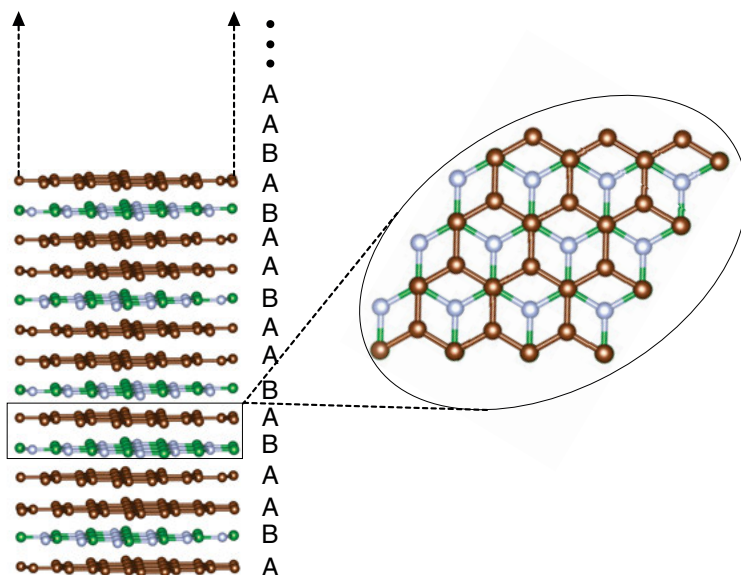
Figure 3.10. Schematic representation of quasiperiodic Fibonacci stacking of graphene and hexagonal boron nitride heterostructure. In inset we have shown the schematics of Bernal stacking that we have used for the stacking the individual layers.

In the previous section (see section 3.3), we have discussed about the planar heterostructure of graphene and h-BN. This idea of heterostructure can be easily extended to three dimension. Graphene and h-BN have a very good lattice matching, which is beneficial for experimental synthesis of high quality stacked 3D heterostructures [120, 121]. Devices with crystalline graphene on h-BN substrate are found to be work better compared to SiO_2 [120]. Giovannetti *et al.* have shown in their *ab-initio* studies that these kind of structures can induce a bandgap [122]. Experimentally, heterostructures of graphene and h-BN have been synthesized by various groups [123–125]. In these structures, possible metal to insulator transitions [123], band gap tuning [126–128] have been observed.

In this section and in Paper IV, we have investigated structural as well as electronic properties of a unique quasiperiodic stacking of h-BN and graphene.

3.4.1 Structural arrangement

Our proposed 3D quasiperiodic structure of graphene and h-BN follows a Fibonacci sequence, S_j. It follows a recurring relation as shown below,

$$S_{j+1} = \{S_j, S_{j-1}\}; \text{where } S_0 = \{B\} \text{ and } S_1 = \{A\}$$
$$\{A\} = \text{graphene single layer}$$
$$\{B\} = \text{h-BN single layer}$$

So the first few sequence will be as follows,

$$S_2 = \{S_1, S_0\} = \{AB\},$$
$$S_3 = \{S_2, S_1\} = \{ABA\},$$
$$S_4 = \{S_3, S_2\} = \{ABAAB\}, ...$$

We have schematically shown the Fibonacci sequence in Fig. 3.10. For the arrangement of inter layer stacking, we have used Bernal stacking which has been shown in the inset of Fig. 3.10. We have considered four different heterostructures with 13, 21, 34, 55 layers and henceforth referred as Fib_{13}, Fib_{21}, Fib_{34}, Fib_{55} respectively. Following the above mentioned Fibonacci sequences, these four heterostructures have the following number of BN (N_{BN}) and graphene (N_C) layers,

$$13 \text{ layers} = (N_{BN}, N_C) = (5, 8) \Longrightarrow \text{Fib}_{13}$$
$$21 \text{ layers} = (N_{BN}, N_C) = (8, 13) \Longrightarrow \text{Fib}_{21}$$
$$34 \text{ layers} = (N_{BN}, N_C) = (13, 21) \Longrightarrow \text{Fib}_{34}$$
$$55 \text{ layers} = (N_{BN}, N_C) = (21, 34) \Longrightarrow \text{Fib}_{55}$$

We have also considered reverse structures by switching the layer compositions. These reverse structures have (8, 5), (13, 8), (21, 13) and (34, 21) layers of (N_{BN}, N_C). This reversing of structures has two relevance, i) change in the concentration of graphene and h-BN layers and ii) change of the interface ordering keeping the number of interfaces unchanged.

3.4.2 Stability and energetics

The 3D heterostructure of h-BN and graphene in forward Fibonacci sequence has two basic building blocks: i) a bilayer graphene sandwiched between h-BN layers from top and bottom, and ii) single layer of graphene in between

Figure 3.11. Schematic representation of different building blocks (a-c) of Fibonacci stacking and their relative formation energy. (d) shows the Fibonacci stacking of graphene and h-BN with most stable building block in it.

two h-BN layers. In first building blocks, following the AB stacking, three different layer configurations are possible e.g., B-C_α-C_β-B, B-C_α-C_β-N, N-C_α-C_β-N. Here α and β represent two different sublattice of C atom. Our calculation indicates that B-C_α-C_β-B structure is more stable compared to the other structures. In Fig. 3.11, we have shown the schematic representation of these building blocks along with their relative energies. The second building block has a B-C_α-B structure where α sublattice C atom of graphene has B atoms on both sides and β sublattice C atom has hexagon center of h-BN on both sides.

We have calculated the formation energies using the following formula

$$E_f = E(\text{G}_m + \text{h-BN}_n) - [m * E(\text{G}) + n * E(\text{h-BN})],$$

where $E(\text{G}_m + \text{h-BN}_n)$ is the total energy of the hybrid graphene BN system, $E(\text{G})$ is the total energy of a single layer graphene, and $E(\text{h-BN})$ is the total energy of a single layer h-BN. The number of graphene and h-BN layers are represented by m and n respectively. The formation energies are normalized by the number of interfaces. In order to compare the stability of these quasiperiodic structures with regular ghaphene and h-BN stacking, we have calculated the formation energies for all these structures. Our calculation shows that the formation energies for all the heterostructures (Fib$_{13}$, Fib$_{21}$, Fib$_{34}$, Fib$_{55}$) are quite similar in values (-63 to -66 meV with LDA exchange correlation and -157 to -161 meV with PBE+vdW). The formation energy for regular graphene

and h-BN structure is much higher (-51 meV with LDA and -130 meV with PBE+vdW) as compared to the Fibonacci structures, which indicates better stability of these quasiperiodic structure over the regular stacking of graphene and h-BN. In the reverse structures with B-C_α-B as building blocks, similar formation energies are obtained.
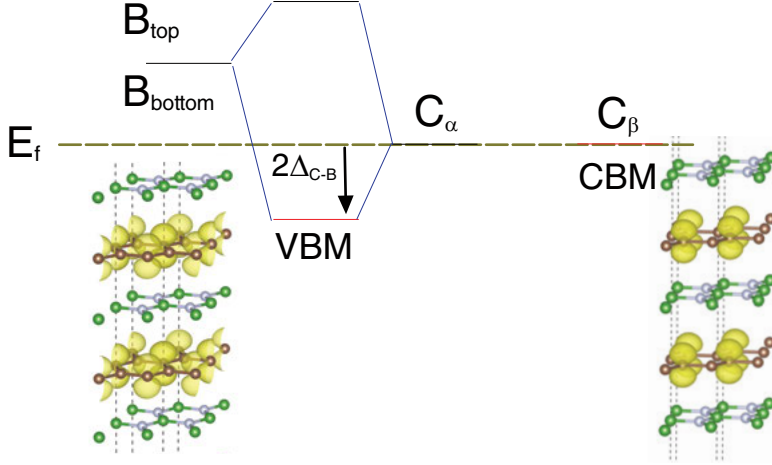
Figure 3.12. Schematic diagram of band level splitting in Fib_{21} reverse structure along with the partial charge density plots for valence band maximum (VBM) and conduction band minimum (CBM) at Dirac point.

Our calculations reveal that the forward Fibonacci structures are metallic while the reverse structure opens up a gap. The B-C_α-C_β-B structure is metallic as the sublattice symmetry is not broken here. However, in B-C_α-B structure, the sublattice symmetry is broken because C_α and C_β atoms have two different environments. Fig. 3.12 shows a schematic picture of level splitting in B-C_α-B structure. The π orbitals of C and B have different energy levels. It causes the C atom from α sublattice to reduce its energy to make a bonding orbital with B. However, the energy level of C from β sublattice does not change. These cause breaks in sublattice degeneracy and opens up a gap. Normal Fibonacci heterostructures contain both blocks and hence remain metallic. On the other hand, the reverse Fibonacci structures contain only B-C_α-B blocks and hence open up band gaps in the order of 13 to 42 meV.

4. The Influence of Defects

"Who in the world am I? Ah, that's the great puzzle."

— Lewis Carroll, Alice in Wonderland

In this chapter, we will discuss how defects can affect the properties of two dimensional (2D) materials which may some time be beneficial or may some time be detrimental from the application point of view. The results have been presented in Papers V–IX. In the following sections, we will discuss: 1) how vacancy defects affect the adsorption and magnetism of Fe cluster, 2) how various defects change the properties of pristine 2D transition metal dichalcogenides, 3) effect of defects in local transport properties in graphene and silicene, and 4) how defected graphene can help in gas sensing activities and fluorination of graphene.

We have used VASP [98, 99] code for our electronic structure calculations. For transport calculation we have used the SIESTA [129] code. Finite temperature diffusion of Fe atoms on the 2D sheet was studied using Born-Oppenheimer molecular dynamics (MD). The temperature was controlled using Nosé thermostat [130–132].

4.1 Adsorption and magnetism of Fe cluster on graphene with vacancy defects

The chemical and magnetic interactions of Fe_n (n=1–6) clusters with vacancy defects (monovacancy to correlated vacancies with six missing C atoms) in graphene have been presented in paper V. As discussed in the introduction, graphene in particular is prone to the formation of vacancy defects. These vacancy defects are quite probable to form strong reactive centers [133, 134] and such defects can affect the electronic structure and hence transport properties of graphene [31, 32]. It is possible to trap magnetic adatoms or clusters at various defect sites [133] and a flux of adatoms may generate various sizes of magnetic nanoclusters at defect sites.

Another reason for investigating trapping of clusters with ferromagnetic species, is that for all applications of graphene in spintronics must include a ferromagnetic spin injector. Regarding spintronic applications, the out-of-plane magnetization has a technological application as it can be used to increase storage density. Finite size clusters may act as potential candidate. Another aspect

is the spin-dipole contribution, which arises from the anisotropic spin densities. For low dimensional systems, it has a significant role on the effective moment, which is the sum of spin and spin-dipole moments, which can be measured by X-ray magnetic circular dichroism (XMCD) experiments.

Given this background, in this work, we tried to analyze how robust is the formation of clusters on defected sites. The effects of magnetic anisotropy and the spin-dipole moments under strong Coulomb interaction on these systems are also discussed.

The *ab-initio* calculations were performed using PAW method and PBE exchange correlation functional. The effect of strong electron-electron interactions were taken into account using PBE+U method [135], where the Coulomb parameter U is added in the Hubbard formalism. For these calculations, we have used $U = 4$ eV and the intra-atomic exchange parameter $J = 1$ eV, which are typical values for $3d$ transition metals. [135, 136].

4.1.1 MD results

In order to investigate how a number of Fe adatoms placed on a defected graphene diffuse, especially whether the Fe adatoms remain isolated or form a cluster, we have performed limited real time Born-Oppenheimer molecular dynamics (MD) up to 30 ps at constant temperature $T = 300$ K, a temperature expected in most practical applications. We have placed six Fe adatoms at six different sites on the sheet and also removed two adjacent C atoms to create a vacancy. Figure 4.1 shows the potential energy landscapes and corresponding geometries (marked by arrows in figure) at different simulation times. The analysis of trajectories and movies of the motion of Fe atoms reveal interesting observations. At the beginning of the simulation, the C atoms near the divacancy center come closer and heal the divacancy to form a 585 defect (Fig. 4.1(a)). Then the Fe adatoms from the adjacent hexagonal sites come together and form dimers (Fig. 4.1(b)-Fig. 4.1(d)) in about < 0.7 ps. These dimers come closer to form a cluster (Fig. 4.1(e)-Fig. 4.1(g)). Finally, in the presence of the Fe cluster near the defect, one Fe atom from the cluster forms bond with the C atoms at the defect site and hence breaks the C–C bonds of the pentagonal rings of the 585 defect (Fig. 4.1(h)). Once the cluster gets trapped at the defected site, it remains trapped and only shows thermal oscillations till the end of the simulation time. Frequent breaking and forming of bonds within the Fe cluster and between Fe and C atoms can be seen during this time. Fig. 4.1(i), the lowest energy structure obtained from the geometry optimization after the MD simulation, shows the formation of bonds within Fe cluster and between Fe and C atoms. Thus our simulations indicate that the formation of cluster at defected site is fairly robust.
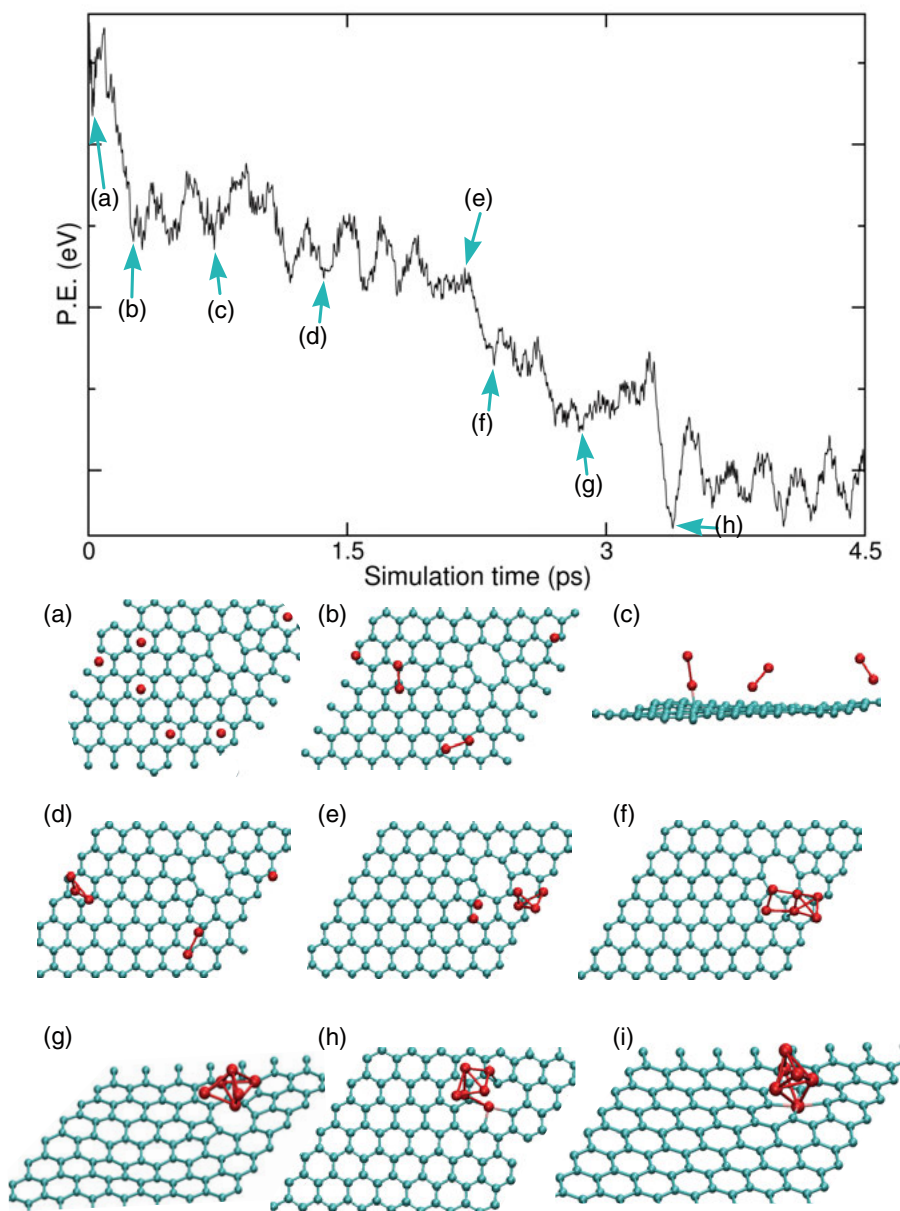
Figure 4.1. Potential energy (P.E.) landscape as a function of simulation time. Schematics (a)-(h) show the snapshots at different simulation times. These snapshots are also marked by arrow in the P.E. graph. Fig. (i) shows the optimized geometry after the completion of MD simulation for 30 ps. See text in Sec. 4.1.1 for more details. Reproduced with permission from Paper V. Copyright © 2014 American Physical Society.
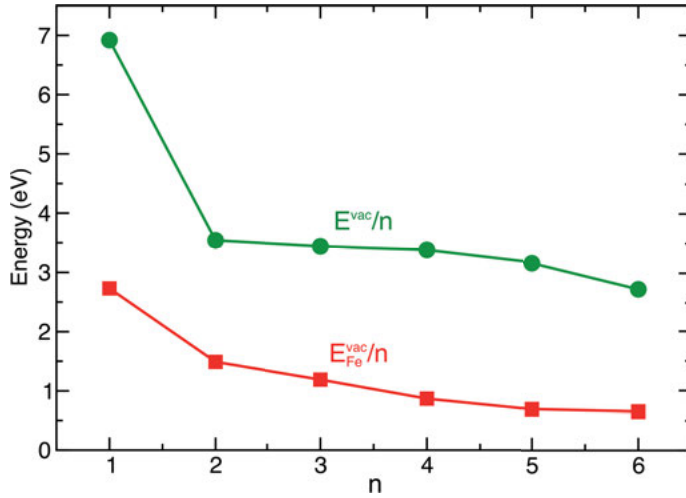
4.1.2 Correlated vacancies in graphene

Figure 4.2. Vacancy formation energies E^{vac} and vacancy formation energies E^{vac}_{Fe} in presence of Fe_n cluster. The energies are normalized with the number of vacancies (n).

Vacancy defects V_1 to V_6 are created by removing C atoms from the same hexagonal ring. Vacancy formation energies (pristine graphene and Fe_n on pristine graphene as reference) are plotted in Fig. 4.2. Excluding V_2, all other vacancies are magnetic due to the presence of dangling bonds. In V_2, saturation of dangling bonds leads to zero magnetic moment. The analysis of vacancy formation energies yields some interesting observations. The energies are gradually reduced with an increase in the number of vacancies correlated to each other indicating that already formed vacancies help to create more vacancies to make the hole bigger and bigger. Another important observation is that Fe clusters promote creation of vacancies as the formation energies are drastically reduced in presence of Fe. This is consistent with the observation made by Boukhvalov and Katsnelson [137], where the Fe atoms were shown to destroy the graphene sheet by creating vacancies.

4.1.3 Interactions of defected graphene with Fe_n clusters

Geometry, energetics & magnetic structure

In Fig. 4.3, we have shown the geometries and spin densities for Fe_n clusters adsorbed on V_n with $n = 1 - 6$. The left and right column show top and side views respectively. For the sake of comparison, the geometries of the free Fe clusters are also shown in the insets of the figures at the left column. The analysis of geometry indicates that in general, the underlying vacancy does not
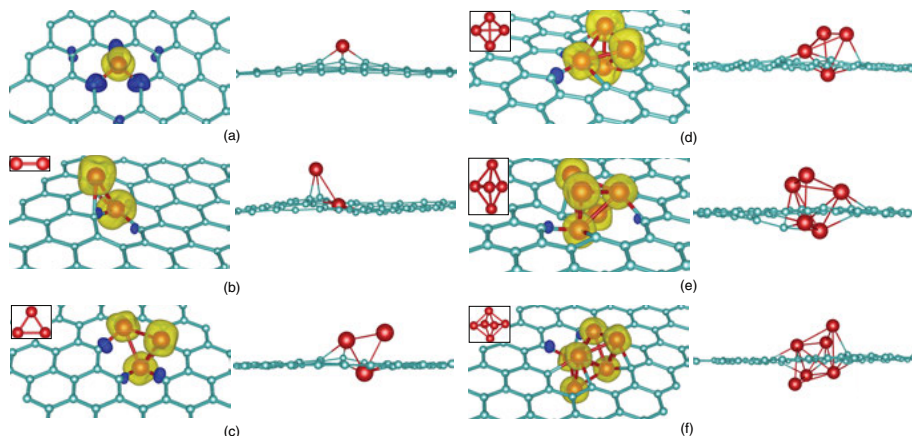
Figure 4.3. Geometries and spin density of Fe_n clusters on V_n vacancies (n=1-6) are shown together. Cyan and red balls indicate C and Fe atoms respectively. Yellow and blue isosurface denotes positive and negative spin densities. Reproduced with permission from Paper V. Copyright © 2014 American Physical Society.

undergo any significant structural rearrangement in presence of Fe clusters. Thus even a single Fe adatom can be used to maintain the structure of underlying lattice despite the presence of the vacancy. The geometries of Fe clusters on graphene are remarkably different from those studied in free space [138]. As seen from Fig. 4.3(a), the optimized geometry for Fe_1 on V_1 shows that the minimum energy position for Fe is at the center of the vacancy. The average Fe–C bond length is ~ 1.77 Å for this case and the height of the Fe adatom from the graphene plane is ~ 1.19 Å. The dimer bond length is about 10 % enhanced in presence of a divacancy in graphene (see Fig. 4.3(b)) from the bond length found in a free cluster. The trimer in free space is reported to be an isosceles triangle [138, 139], while the trimer on a vacancy (see Fig. 4.3(c)) is a distorted isosceles triangle with the bond lengths differing substantially from that in free space. Fe_4 also forms a prism in free space with the bond lengths ranging from 2.22 – 2.41 Å. However in our case the bond length varies substantially from 2.2 Å to 2.63 Å (see Fig. 4.3(d)). The change in the trigonal bi pyramid of isolated Fe_5 is seen in the vertical four-atom plane where the bond lengths are increased with respect to those in free space (see Fig. 4.3(e)). Fe_6 undergoes a substantial change from octahedron to a more complex structure seen in Fig. 4.3(f).

In Table 4.1, the adsorption energies for the Fe_n clusters in a n-vacancy graphene sheet and their magnetic moments are reported, together with the magnetic moments of free Fe_n clusters. As seen from the Table 4.1, the magnetic moments of Fe clusters are slightly reduced by their adsorption on the n-vacancies except for Fe_6 on V_6 and Fe_1 on V_1 where the reduction is huge. However, the magnetic character of the C atoms near to the vacancy is signif-

61

Table 4.1. *Adsorption energies $E_{V_n}^{ad}$ (in eV) for Fe_n cluster adsorbed in n-vacancy graphene sheet, together with their magnetic moments (in μ_B). The calculations are done within PBE+U formalism. The middle column shows the total moment of a Fe cluster on graphene with defects, while the right hand column shows that calculated moment for free Fe clusters. Reproduced with permission from Paper V. Copyright © 2014 American Physical Society.*

n	$E_{V_n}^{ad}$/n	μ_B/n	$\mu_B^{Fe_n}$/n (Free)
1	5.36	0.32	4.0
2	2.80	3.00	4.0
3	2.60	3.32	4.0
4	2.97	3.00	3.5
5	2.71	3.20	3.6
6	2.34	3.33	3.33

icantly affected as seen in Fig. 4.3. The magnetization of the whole system is still basically due to the Fe adatoms. Except for the case with one Fe adatom on a single vacancy, the average Fe magnetic moments for the adsorbed clusters are not so different from the moments in free state. The drastic reduction of magnetic moment for the Fe atom adsorbed at the monovacancy site is due to a strong hybridization between the Fe–d and C–p orbitals at the defect site.

It can be noted that magnetic moments of the C atoms for the defected graphene has reduced significantly after the adsorption of Fe clusters. The analysis reveals that Fe atoms induce a substantial number of states on the Fermi level and it is seen that those are mainly d-like. This feature is general and is present in all the clusters. Partially filled in-plane p orbitals of the edge C atoms around the vacancy sites hybridized with the d-orbitals of adsorbed Fe atoms to pacify the dangling bonds and hence, destroy the local moments at those edge C atoms.

Orbital moments, magnetic anisotropy and spin-dipole moments
We have included SOC in the Hamiltonian to calculate the orbital moments and magnetic anisotropy energies (MAEs) for Fe_n cluster adsorbed systems. Here, MAE corresponds to only magneto-crystalline energy originating from spin-orbit coupling while the contribution of shape anisotropy is neglected. Table 4.2 shows easy axis, magnetic anisotropy and orbital magnetic moments along the easy axes. The calculated average orbital moment of the Fe atoms in these systems are similar to the calculated value for bulk Fe ($\sim 0.05\ \mu_B$ without orbital polarization) in the bcc phase. It is interesting to note that Fe_1 and Fe_4 clusters exhibit out-of-plane easy axes whereas the other ones have easy in-plane magnetization. Therefore, for a flux of adatoms of Fe deposited on graphene defect sites with varieties of cluster formation, one may expect that the cluster macrospins to lie in the plane or perpendicular to the plane of

Table 4.2. *MAE-Data with PBE+U , magnetic anisotropy energy ($\Delta E = E^{hard} - E^{easy}$), average orbital moment for Fe_n clusters on n-vacancy graphenes. Reproduced with permission from Paper V. Copyright © 2014 American Physical Society.*

Cluster	$\langle \mu_{orb} \rangle$	ΔE (meV)	Easy axis	Hard axis
Fe_1	0.010	0.012	(001)	(100)
Fe_2	0.047	0.396	(010)	(100)
Fe_3	0.042	0.843	(010)	(100)
Fe_4	0.032	0.504	(001)	(100)
Fe_5	0.042	0.694	(100)	(010)
Fe_6	0.042	0.708	(100)	(001)
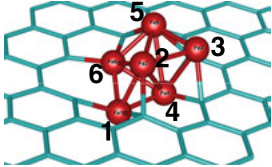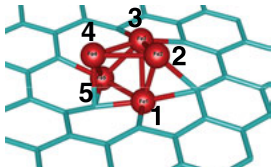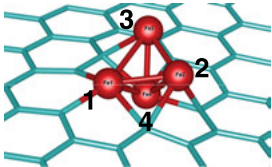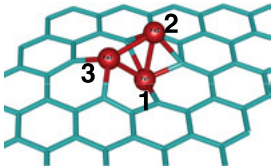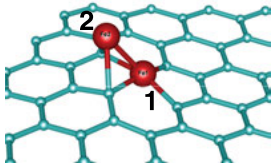
graphene. However, one should note that the cluster magnetization directions will be quite robust as the magnetic anisotropy energies are not so small in magnitude.

In systems having low symmetry, the contribution of the spin-dipole term is expected to be quite significant. Hence, we have performed DFT calculations to calculate the spin dipole moments, following the method prescribed by Freeman *et. al.* [140]. In Table 4.3, the values of spin moments m_s, spin-dipole moments ($7\langle T_z \rangle$) and effective moments (m_{eff}) are shown. One can clearly see that (i) the spin-dipole contributions are not negligible and (ii) the signs of $7\langle T_z \rangle$ are opposite to m_s in many cases, thereby reducing the effective moments of certain Fe atoms in each cluster. The average effective moment varies non monotonically e.g., the $\langle m_{eff} \rangle$ are 2.63 μ_B, 2.65 μ_B and 3.18 μ_B for $n = 4 - 6$ respectively. In fact, the value of $7\langle T_z \rangle$ can reach up to 33 % of the spin moment. However, the average effective magnetic moment of the total system does not vary much from the average spin moment due to mutual cancellation of atomic $7\langle T_z \rangle$.

4.2 Atomic-scale defects in 2D transition metal dichalcogenides

The effect of various point defects on the structural, electronic and optical properties of transition metal dichalcogenides (TMDs) have been presented in Paper VI. As discussed in the introduction, 2D TMDs are one of the alternative "beyond graphene" family members. Unlike graphene, these TMDs are semiconductors. Defects in general create impurity states into the band gap region either closer to the valence band (p-type) or closer to the conduction band (n-type). The interaction of localized states from the defects can couple strongly with the continuum of ionic crystals which have applications in solid state lasers, white LEDs etc [141].

Table 4.3. m_s, $7\langle T_z \rangle$ and $m_{eff} = m_s + 7\langle T_z \rangle$ *values for* Fe_n *clusters adsorbed in n-vacancy graphene system. Calculation were done within PBE+U formalism. Reproduced with permission from Paper V. Copyright © 2014 American Physical Society.*

Cluster	Atom	m_s	$7 < T_z >$	m_{eff}
Cluster size = 6				
	1	3.13	-0.51	2.62
	2	3.18	0.62	3.80
	3	3.24	-0.48	2.76
	4	2.99	0.11	3.10
	5	3.21	0.14	3.35
	6	2.95	0.50	3.45
Cluster size = 5				
	1	2.55	-0.52	2.03
	2	3.23	-0.61	2.62
	3	3.06	0.65	3.71
	4	3.30	-0.72	2.58
	5	2.73	-0.41	2.32
Cluster size = 4				
	1	2.59	0.31	2.90
	2	3.05	-0.99	2.06
	3	3.14	-0.44	2.70
	4	2.81	0.04	2.85
Cluster size = 3				
	1	2.81	-0.03	2.78
	2	3.20	-0.68	2.52
	3	2.85	0.31	3.16
Cluster size = 2				
	1	2.84	0.32	3.16
	2	2.93	0.14	3.07
Cluster size = 1				
	1	0.91	-1.15	-0.24

It is not uncommon to find vacancies during the fabrication process. For example MoS_2 has been found to acquire S vacancies during fabrication which create deep trap states for electrons [142, 143]. These trap states damage the *n*-type conductivity of MoS_2. The mode of fabrication also dictates the amount of defect concentration [144, 145]. There are few theoretical studies available in the literature where specific defects have been studied [142, 143, 146–153]. However systematic studies on the role of various point and double defects on the electronic and optical properties of TMDs are not available in the literature. Therefore, in this work (Paper VI) we tried to address systematically the role of defects in electronic and optical properties of MX_2 TMDs where M = Mo, W and X = S, Se, Te.

4.2.1 Structure and formation energies
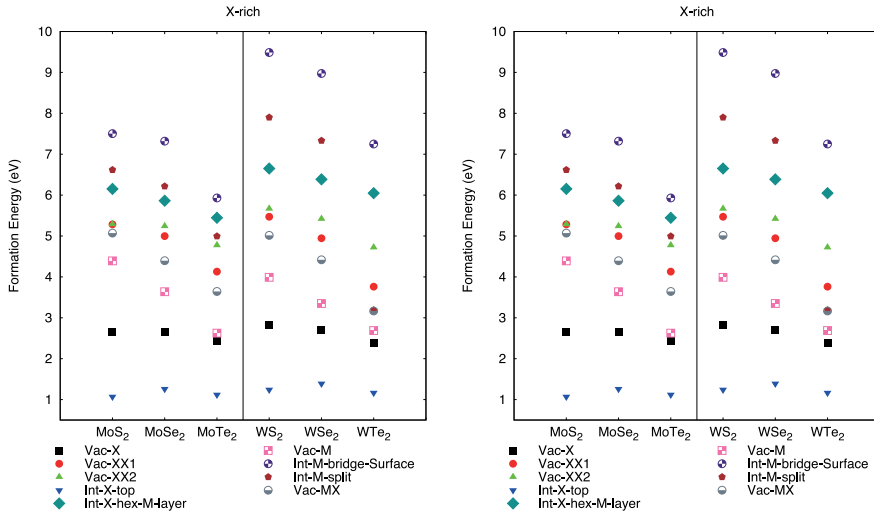
Figure 4.4. Formation energies for different types of defects in various MX_2 systems under both X–rich and M–rich conditions. Reproduced with permission from Paper VI. Copyright © 2015 American Physical Society.

For our study, we have considered six different type of defects namely X vacancy, X interstitial, M vacancy, M interstitial, XX vacancy and MX vacancy. We have used various possible configurations of geometry to determine the minimum energy structure for all the systems. We have calculated the forma-

tion energies (E_f) using the following formula:

$$E_f = E_{\text{defect}} - \left[E_{\text{pristine}} + \sum_i n_i \mu_i \right], \text{ where}$$

E_{defect} = total energy of MX_2 supercell with defect

$E_{pristine}$ = total energy of MX_2 supercell without defect

n_i = number of i element added or removed (with a negative sign)

μ_i = chemical potential of the element i

We have shown the calculated formation energies under X rich and M rich
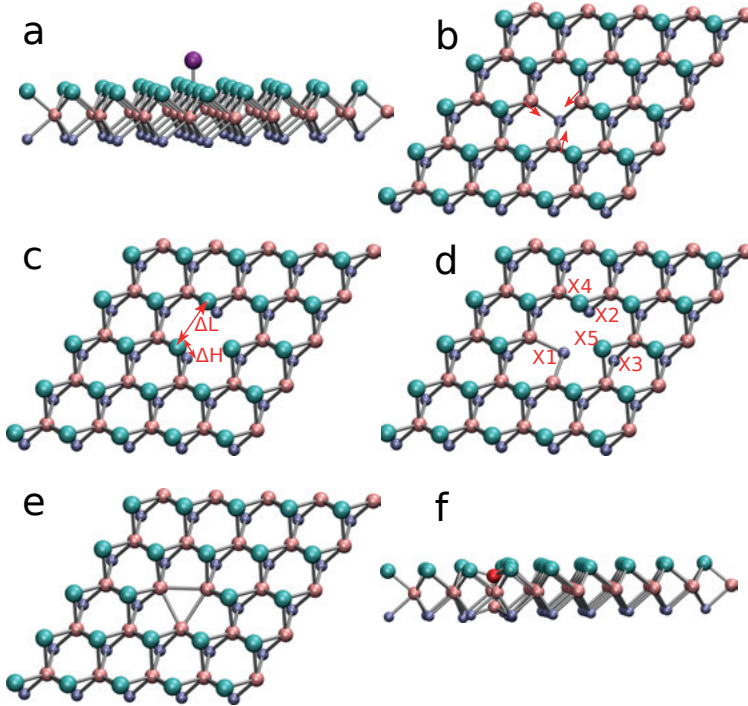
Figure 4.5. Representative figure of optimized geometries for various defects in MX_2 system as designed on 5×5×1 supercell. (a)–(f) represent the following defects: (a) X interstitial, (b) X vacancy, (c) M vacancy, (d) MX vacancy, (e) XX vacancy and (f) M interstitial. The cyan (large) balls denote the X atoms from the top layer, pink (medium) balls denote M atoms and dark blue (small) balls denote X atoms from the bottom layer. In (a), the purple ball refers the X interstitial atom. In (f), the red ball indicates to the M interstitial atom. Red arrows in (b) indicates the movement of M atoms during the relaxation. ΔL and ΔH in (c) represents the change of in-plane and out-of-plane displacements of the X atoms around the M vacancy due to structural relaxation. Reproduced with permission from Paper VI. Copyright © 2015 American Physical Society.

conditions for all the geometries that we have considered in our simulations in Fig. 4.4. The most stable geometries for X interstitial, X vacancy, M vacancy, MX vacancy, XX vacancy, and M interstitial defect have been shown in Fig. 4.5 (a)–(f), respectively. The formation energy calculations show that the stable X interstitial structure is obtained when the X atom is attached on top of a host X atom (Fig. 4.5 (a)). X vacancy is created by removing one X atom from the top X layer. Here, three M atoms surrounding the vacancy relax towards the vacancy site (Fig. 4.5 (b)). For M vacancy, six X atoms with dangling bonds dictate the relaxation of their geometries near the vacancy site. Outward relaxation from the vacancy center can be observed for S and Se atoms. However, for Te atom, the relaxation occurred towards the vacancy center (Fig. 4.5 (c)). The energetically favored position for M interstitial defects are when the M atom is at the split interstitial position along the c direction except WTe$_2$ (Fig. 4.5 (f)). For WTe$_2$, after relaxation the interstitial W atom settled at hexagonal position in the W layer forming a distorted hexagon. During optimization of MX vacancy, five neighboring X atoms (X1–X5 in Fig. 4.5 (d)) nearer to the vacancy site mainly relax. Lowest energy XX divacancy structure is obtained when correlated X atoms are removed from the top and bottom layers of X atom (with same x and y coordinates). The M atoms are in general relax towards the vacancy site and form an equilateral triangle (Fig. 4.5 (e)). See Paper VI for details.

## 4.2.2 Defect concentration at equilibrium

In order to find out the concentration of defects in finite temperature crystal growth condition, we have also calculated the equilibrium defect concentration using the following formula,

$$C_{eq} = N e^{-E_f / k_B T}$$

where N is the concentration of possible defect sites, E_f is the zero temperature formation energy of the defect and T is the temperature. We have chosen T= 1000 K – 1200 K during the crystal growth. This range of temperature is chosen as most of the MX_2 single layer structures are synthesized experimentally in this range [154–159]. From our calculation, it is quite evident that under X rich condition, X interstitial defects and under M rich condition, X vacancy defects will occur more frequently. However, the probability of forming M interstitial or M vacancies are quite low.

## 4.2.3 Electronic structure and optical properties

Energy level diagrams for all six defects in all MX_2 system have been constructed and shown in Fig. 4.6. The columns (a)–(f) in each subplot indicates
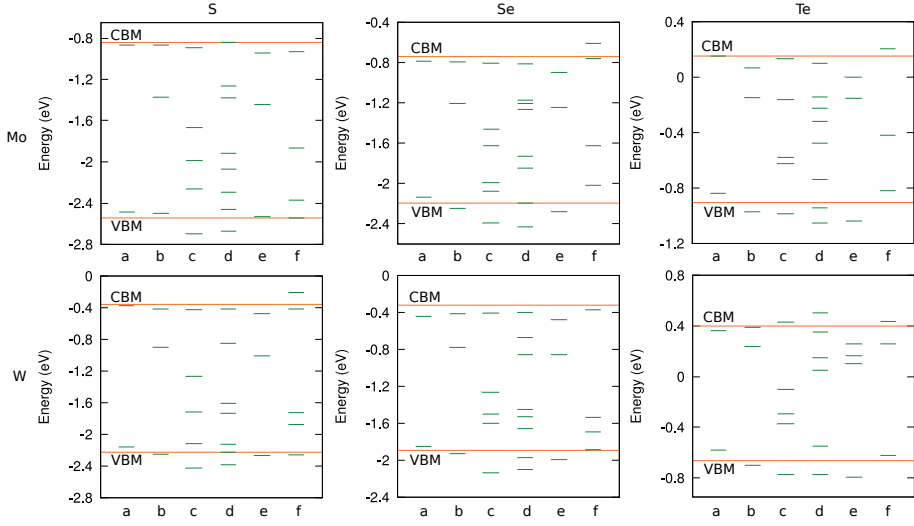
Figure 4.6. Energy level diagram for different defects in all the MX_2 systems. In each subplot, columns (a)-(f) refer to X interstitial, X vacancy, M vacancy, MX vacancy, XX vacancy and M interstitial respectively. The orange (long dashed in print) line shows the position of VBM and CBM for pristine MX_2. Green solid and dashed lines denote the occupied and unoccupied defect states respectively. Reproduced with permission from Paper VI. Copyright © 2015 American Physical Society.

X interstitial, X vacancy, M vacancy, MX vacancy, XX vacancy, and M interstitial defect, respectively. The position of conduction band minima (CBM) and valence band maxima (VBM) were marked using an orange dashed line. The green solid and dashed line represents the position of defect states in occupied and unoccupied states, respectively. Density of states (DOSs) calculation indicates that the qualitative nature of DOSs are quite similar between MoS_2, WS_2; $MoSe_2$, WSe_2; and $MoTe_2$, WTe_2. Our analysis of energy level diagram (see Fig. 4.6) and DOSs indicate that in general defect states appear in the band gap region of the pure system except for X interstitial defects. In case of X interstitial defects, the impurity states appear near the band edges and merge with both valence and conduction bands.

Defects in the MX_2 can also cause changes in the optical properties. However, our calculations indicate that the most notable change can be visible for the following three defects: - i) M vacancy, ii) X vacancy and iii) MX vacancy. Therefore we have shown optical spectra for the three defects in MoX_2 system in Fig. 4.7. For Mo vacancy in MoS_2, defect peaks occur below and above the Fermi energy giving rise to a transition around 1 eV. The peak in $MoSe_2$ is broader due to the fact that there are two possible transitions within a very close energy range. In $MoTe_2$, the defect state due to Mo vacancy occurs very close to the Fermi energy and therefore generates a sharp optical transition at a very

68
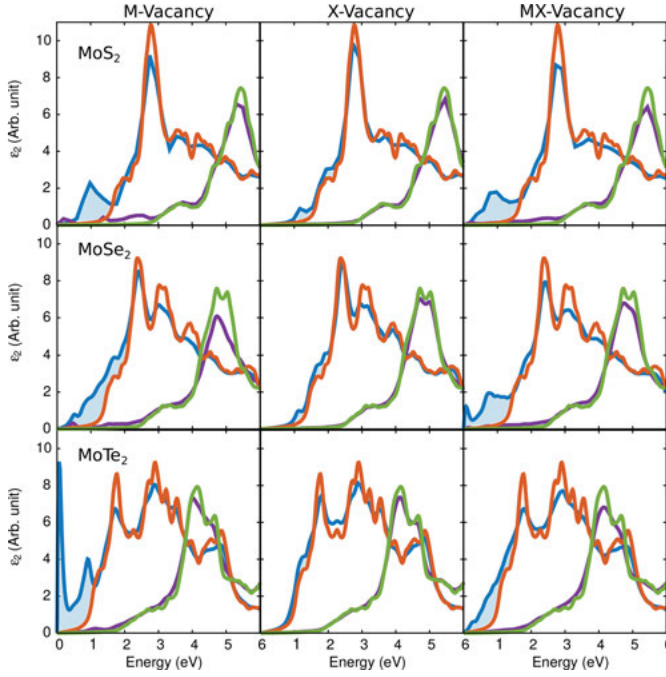
Figure 4.7. Comparison of imaginary parts of the dielectric functions (ε_2) between MoS$_2$, MoSe$_2$, and MoTe$_2$ for M vacancy, X vacancy, and MX vacancy. Blue and orange lines denote in-plane contribution of ε_2 for defected and pure systems, respectively. Purple and green lines denote out-of-plane contribution of ε_2 for defected and pure systems, respectively. The shaded region represents the prominent contributions of defect related peaks compared to the pristine system. Reproduced with permission from Paper VI. Copyright © 2015 American Physical Society.

low energy. For X vacancies, defect states are closer to conduction band minimum and hence the optical spectra show slight changes from pristine. There are number of defect peaks appearing near the Fermi energy for MX vacancy and hence transition occurs at around 0.5 eV, which shows a broader peak compared to the M vacancy. For MX_2 systems, the absorption spectra occur in the visible region which can be suitable for photocatalysis using sunlight. Optical properties for the above three defects show similar characteristics for WX_2 systems.

4.3 Electronic transport properties of graphene and silicene with defects

As we have discussed before, silicene (a 2D sheet of Silicon) can be a viable alternative to graphene. Silicene has hexagonal structure and its electronic

properties are similar to graphene. The electron mobility in silicene is also in the same order of magnitude as in graphene [160]. Defect free monolayer graphene or silicene is very difficult to obtain in large scale fabrication process such as CVD and it results in creation of few defects [54, 55]. Although defects can effect adversely to device properties [54], in nanoscale defects can introduce exciting features which can be used for various applications [59, 60, 161–163]. Defects in graphene and silicene have been studied from the perspective of electronic structure, creation, mobility, self healing, etc [27, 57, 164–168]. However, there are not adequate studies about the electronic transport properties of defects e.g., local defects, in two dimensional silicene as well as in graphene. In Paper VII, we have used *ab-initio* density functional theory with non-equilibrium Green's function (NEGF) [169, 170] methods to compare different defects in these two monolayers and analyze electronic transport calculations.

For these calculations, we have used SIESTA [129] code using a double-ζ polarized basis set (DZP) for valence electrons, and norm-conserving pseudopotentials [171].

4.3.1 Structures and energetics

We have considered four different defects in graphene and hexagonal silicene. These are: i) Stone-Wales defect, ii) Monovacancy, iii) 585 divacancy (divacancy with two pentagon and one octagon, and iv) 555777 divacancy. In Fig. 4.8(a)-(d), we have shown the schematic representations of these defects along with the setup used for calculation of electronic transport (see Fig. 4.8(g)). Side view of graphene and silicene are also shown in the Fig. 4.8(e)-(f).
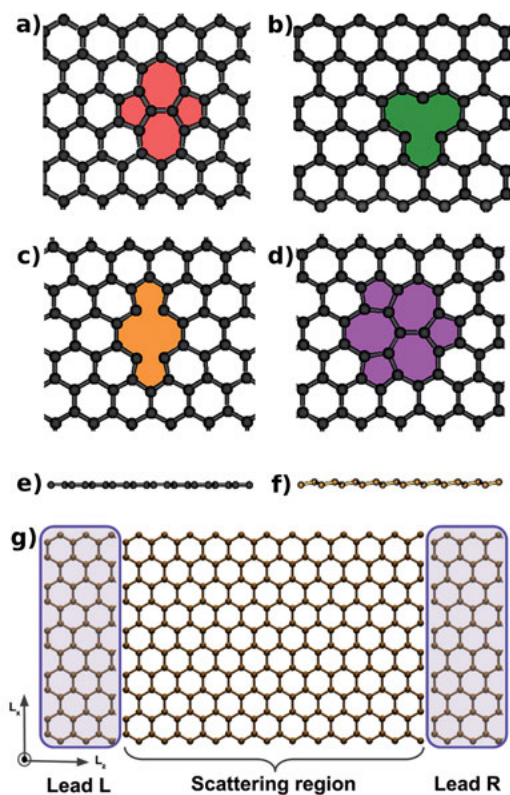
Table 4.4. *Defect formation energies in graphene and silicene. Reproduced from Paper VII by permission of The Royal Society of Chemistry.*

Defect	Formation Energy (eV)	
	graphene	silicene
SW	4.87	1.84
1V	7.62	2.87
2V-555777	6.63	2.74
2V-585	7.48	3.24

In order to find out the relative stability of these defects we have calculated the formation energy using the following formula:

$$E_f = E_{\text{total}}^D - E_{\text{total}} + N\mu_i \,,$$

where, E_{total}^D is the total energy of the system with defect, E_{total} is the total energy of the pristine system. The number of atom removed is denoted by N and μ_i is the chemical potential ($i = $ C or Si).

Figure 4.8. Top view of the schematic representation of the defective structures used in this work for both graphene and silicene: a) Stone-Wales (SW), b) monovacancy (1V), c) divacancy (2V-585) and d) divacancy (2V-555777). Side view of e) graphene, f) silicene. While pristine graphene is perfectly flat, silicene exhibits a rugged structure. g) Setup used in the electronic transport calculations for both graphene and silicene: two electrodes and a central scattering region. Reproduced from Paper VII by permission of The Royal Society of Chemistry.

The defect formation energies are tabulated in Table 4.4. Our results show that defects in silicene have a smaller E_f than graphene by at least a factor of two. This is mainly due to the cohesive energy. Cohesive energy in silicene is 4.27 eV/atom whereas it is 8.21 eV/atom in graphene. Hence defect formation in silicene has higher probability as compared to graphene. A clear hierarchy of formation energies can be observed for both graphene and silicene. The order of stability in graphene is $SW < 2V - 555777 < 2V - 585 < 1V$. However for silicene, the order is slightly different $SW < 2V - 555777 < 1V < 2V - 585$.

In graphene, the stability of 2V-585 defect is lower compared to 2V-55577 defect because of two broken bonds. In silicene, monovacancy has smaller

formation energy than 2V-585 defect. However, in graphene, the trend is opposite. The reason behind this is that the buckling in silicene helps for better rearrangement of dangling bonds in monovacancy compared to graphene. This is also evident in the value of magnetic moment. While monovacancy in graphene shows a 1.4 μ_B magnetic moment, monovacancy in silicene shows zero magnetic moment.

4.3.2 Transport properties
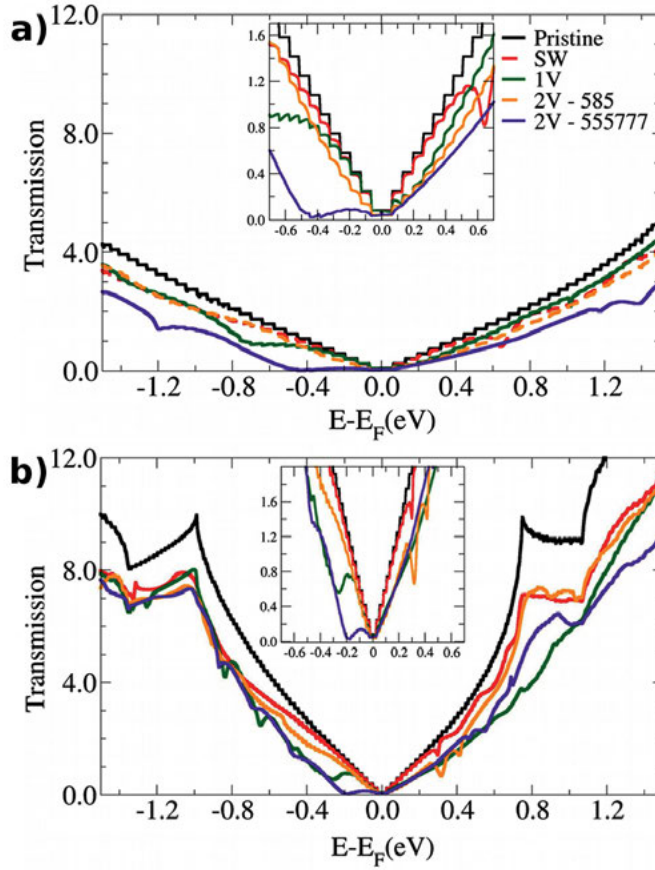
Figure 4.9. Transmission coefficients as a function of energy for the different defects in a) graphene, and b) silicene. The insets show a zoom-in of the region around the Dirac cone. Reproduced from Paper VII by permission of The Royal Society of Chemistry.

We have calculated the transverse electronic transport properties of silicene and graphene and compared them with the pristine system. By applying a com-

bination of source or drain and gate voltage, it is possible to see the signature of different defects in the form of a Fano resonance.

The transmission coefficients for different defects in graphene and silicene have been shown in Fig. 4.9. In pristine system, the Dirac cone feature can clearly be seen. However, the transmittance is larger for silicene due to fact that the valence and conduction bands dispersion are much lower than graphene [10, 172].
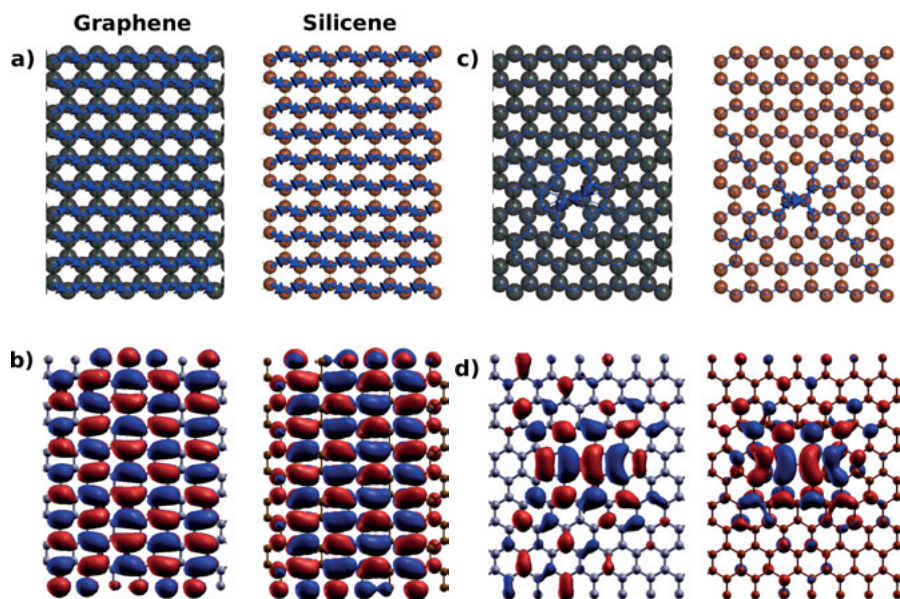
Figure 4.10. Top view of local current (LC) and wave functions (WF) for both graphene and silicene: a) Pristine structure (LC); b) pristine WF; c) Stone-Wales defect and d) Stone-Wales (WF). For WF plots, blue represents the real part and the red represents the imaginary part. The images presented correspond to a zoomed-in region of the actual simulation cell presented in Fig. 4.8(g). Reproduced from Paper VII by permission of The Royal Society of Chemistry.

From the analysis of transport properties, in case of graphene, we can see that there are no significant changes for Stone-Wales and 585 divacancy defects for energy level below the Fermi energy. This is also true for monovacancy till energy -0.4 eV. A broad resonance can be seen at -0.8 eV. Significant change in transmission coefficients can be observed for 555777 divacancy defects where suppression of transmission occurs due to scatterings at states near to the vacancy site. For positive energy level above the Fermi energy, a sharp resonance occurs at 0.65 eV for Stone-Wales defect. However for other cases the changes are minimal, which can be seen in the change of slope of the transmission curve. For silicene, the behavior of the transmission curves are quite similar. However the main difference is that the resonances appear closer to

the Fermi energy which can be accessed by applying relatively small bias and gate voltage.

We have also looked into local transport properties [173] to investigate how it is affected by these resonances. The local transport properties were calculated for pristine system and for Stone-Wales defect as it shows the resonance. Results of local current densities and corresponding wave functions for these systems have been shown in Fig. 4.10. We have chosen $E - E_F = +0.65$ eV for graphene and $E - E_F = +0.29$ eV for silicene as they correspond to the resonance position. Our calculations show that for both pristine systems, the current flows from left to right. The wave functions are spread all over the system and are not localized. For Stone-Wales defect in both graphene and silicene, the local currents are concentrated near the defect site which is consistent with the Fano resonance (coupling between bound state with the continuum of the band). Due to such a high current density near the defect site, one can expect a local heating which can affect the functionality of the devices.

4.4 Gas sensing activity using defected graphene

Gas sensing is one of many application areas where graphene can be used due to its unique properties such as i) being a two dimensional material with only surface and no volume enhancing the effect of surface dopants, and ii) high conductivity and low electrical noise enables graphene to detect very small signal changes because of gas molecule absorption. Among p-doped and n-doped gases, NO_2 has a very good sensitivity to the pristine graphene due to large amount of charge transfer. Gaseous molecules act as electron acceptor or donor when they are adsorbed on graphene. These cause change in career density and hence electrical resistance in graphene, which is the primary gas sensing mechanism in graphene [174]. NO_2 molecules are in general attached to graphene by physisorption. However, it is expected that the NO_2 will interact more with defected graphene as compared to the pristine graphene thus affecting the conduction electrons much more [175]. Hence, creation of defects in pristine graphene can enhance the gas sensing activity.

Therefore, it will be important to understand how gas molecules react with defected graphene. In Paper VIII, together with our experimental colleagues, we have discussed creation of defects in graphene using ion beam irradiation and studied the gas-sensing properties using various experimental techniques. The experimental findings are supported by our *ab-initio* density functional theory.

4.4.1 Experimental sample preparation and measurements

The sample of graphene flakes were created using the mechanical exfoliation methods and deposited on heavily doped Si substrates containing 300 nm SiO_2.

The electrical contacts were created on the device using electron beam lithography. Using ion beam irradiation with 30 keV Ga^+ ions in a vacuum chamber under $\sim 10^{-6}$ mbar pressure, defects were created on the graphene. One single irradiation contains an ion dose of $\sim 10^{12}$ ions cm^{-2} and a 20×20 μm^2 area was irradiated. A mixture of N_2 and 10-ppm NO_2 gases were used as target gas while N_2 gas was used for purging purposes.
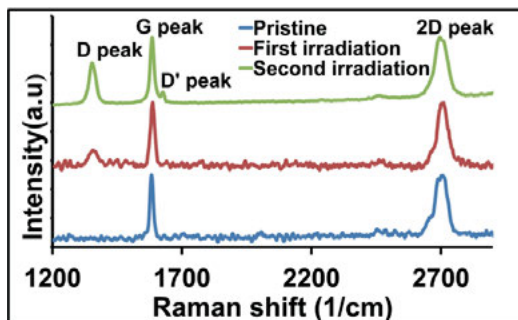

Figure 4.11. The evolution of Raman spectra with respect to the ion irradiation of graphene. The dose is $\sim 110^{12}$ ions cm^{-2} for each irradiation. Reproduced with permission from Paper VIII. Copyright © 2012 IOP Publishing. All rights reserved.
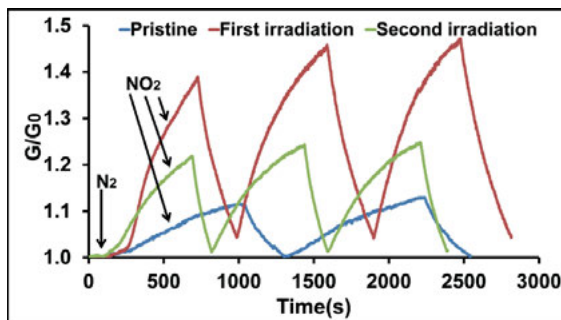
Figure 4.12. Normalized conductance (G/G_0) response of the graphene gas sensor. The exposure of the NO_2 gas started after 110 s in all three cases. During the gas exposure the conductance increases, and by turning off the gas flow and opening N_2 as purging gas, the conductance decreases. From curve fits we find that the average rise times for pristine, first and second defected graphene (during NO_2 exposure) are 500 s, 328 s and 420 s respectively. Reproduced with permission from Paper VIII. Copyright © 2012 IOP Publishing. All rights reserved.

The thickness of the graphene sample can be measured using Raman spectroscopy (514 nm wavelength) and atomic force microscopy experiments. The evolution of Raman spectra with respect to different amount of ion irradiation in graphene along with a Raman spectrum comparison of pristine graphene were shown in Fig. 4.11. G-peak at ~ 1580 cm^{-1} and 2D-peak at ~ 2700 cm^{-1} are the characteristic of Raman spectroscopy in graphene and graphite.

The shape of 2D-peak can be used to identify the number of layers. From the Raman spectra and AFM analysis we conclude that the current sample has a bilayer geometry. The appearance of D and D′ peaks after irradiation indicates the formation of defects .

Fig. 4.12 shows the response of normalized conductance (G/G_0) of pristine, first and second irradiated graphene with a exposure of 100 ppm NO_2 in N_2 at room temperature. G_0 represents the conductance measured in graphene before the exposure of the gases. NO_2 exposure of pristine graphene causes electron transfer to the molecule and increases hole density. Hence the conductance increases. After first irradiation when the defected graphene is exposed to the NO_2 gas, a faster response in changing in conductance can be seen. The normalized conductance response decreases after second irradiation due to possible increase in defects and scattering states and hence the gas sensing properties also decreases.
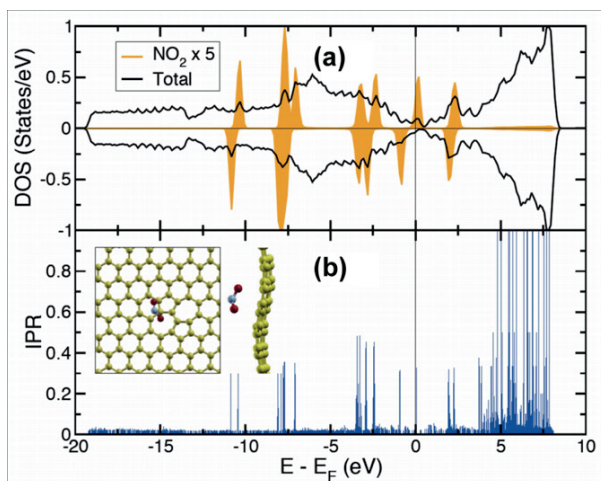
4.4.2 Theoretical simulations

Figure 4.13. (a) Total and molecular NO_2 spin-polarized DOS. (b) Inverse participation ratio (IPR) for the electronic states of Stone-Wales defect with NO_2. In (b), optimized geometry of NO_2 at SW-defect site in the graphene lattice is shown as top and side views. Reproduced with permission from Paper VIII. Copyright © 2012 IOP Publishing. All rights reserved.

We have used monolayer graphene to investigate the interactions between NO_2 and defected graphene using *ab-initio* density functional theory. Monolayer was considered instead of bilayer as most of the defects are same in both cases. We have compared the binding energy of NO_2 in pristine graphene with four different defects in graphene such as monovacancy, divacancy (585), 686 defect [176], and Stone-Wales defect.

Table 4.5. *Binding energies for NO$_2$ molecules on pristine and defected graphene. Reproduced with permission from Paper VIII. Copyright © 2012 IOP Publishing. All rights reserved.*

Structure	E_B (eV)
Pristine	0.30
Monovacancy	0.32
Divacancy (585)	0.28
686 Defect	0.35
Stone-Wales	0.72

In Table 4.5, we have tabulated the binding energies of NO$_2$ molecule with pristine graphene and other defects. Our calculations indicate that the NO$_2$ molecule binds strongly with the Stone-Wales defect with binding energy value of 0.72 eV. In other defects, the binding energies are ~ 0.3 eV.

The total density of states along with the site projected density of states for NO$_2$ are shown in Fig. 4.13. The spin polarized molecular levels of NO$_2$ molecules appear near the Fermi energy causing 1 μ_B / cell magnetic moment. We have also calculated inverse participation ratio (IPR) [177] for the electronic states of NO$_2$ adsorbed Stone-Wales defect (see Fig. 4.13(b)). IPR is inversely proportional to the number of atoms that are contributing to a specific molecular orbital. Hence a quantitative description of molecular orbital localization can be given from IPR. In our calculation, the IPR has very small values near the Fermi energy indicating a conducting character of the states.

The binding energy and sticking probability for NO$_2$ molecules on a pristine and defected graphene surface are further analyzed using Langmuir isotherm model. Our results show that higher binding energies are required in order to explain experimental rise time. Our DFT calculation correctly predicts increase of binding energy for Stone-Wales defect which results into a increased adsorption and conductivity.

4.5 Site-selective local fluorination of graphene with defects

Functionalization of graphene is one of many routes to make graphene advantageous for application purpose. Local approach in functionalization is an up-and-coming method to retain the beneficial properties of graphene after its modification of structure and functionalization. Among various possibilities, functionalization by using plasmas containing radicals is quite promising. Plasma enhanced graphene functionalizations have been shown in various experiments [178–181]. However, these methods are not selective to the local sites and extra photo/electron resist has to be used which can cause unwanted

impurities on the surface of graphene. In Paper IX, we have reported a unique approach which allows a precise site-selective fluorination of graphene. The experimental results are supported by the *ab-initio* density functional theory based simulations.

4.5.1 Sample preparations and experimental results
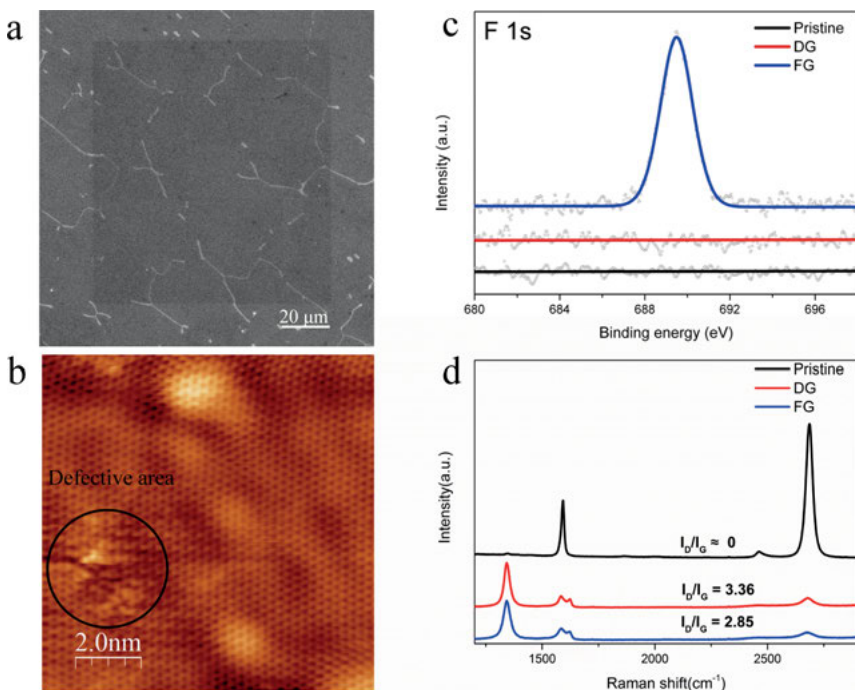
Figure 4.14. Characterization of pristine graphene, defected graphene (DG) and fluorinated graphene (FG). (a) Scanning electron microscope (SEM) image of local functionalization of graphene (100 μm $\times$ 100 μm) with ion doses of 10^{13} ions/cm^2 and simultaneous 167s gas exposure. (b) Scanning tunneling microscopy image of DG under the same ion dosage. (c) X-ray photoelectron spectroscopy spectra of F $1s$ peak of pristine graphene, DG and FG. FG reveals a distinguished F $1s$ peak, and the F $1s$ spectrum of pristine graphene as well as DG is given as a reference. (d) Raman comparison of pristine graphene, DG and FG. Lower I_D/I_G in FG in contrast to DG indicates lower degree of defects density and larger crystalline size. Reprinted from Paper IX.

In order to fluorinate graphene (FG), we have used focused ion beam (30kV Ga$^+$) irradiation dosage of 10^{13} ions/cm^2 with exposure to XeF$_2$ for 167s. For comparison purpose, defected graphene (DG) has been prepared using only ion irradiation. The basic principle of this type of fluorination process is to create reaction between fluorine contained molecules and defected graphene

containing carbon atoms with dangling bonds. We have used 100 μm $\times$ 100 μm area for the irradiation purpose (see Fig. 4.14(a)). Fig. 4.14(b) shows the scanning tunneling image of DG structure prepared using same ion irradiation dosage. Under this amount of dose, most of the lattice structures of graphene remains intact. However, defects in terms of vacancies form in the damaged part of the graphene. Distinct XPS peak for F $1s$ can be seen in FG which indicates its formation. The intensity of F $1s$ peak increases for grazing angle signifying the surface localization of fluorine atoms.

Structural information can also be obtained from the Raman spectroscopy (see Fig. 4.14(d)). The analysis of Raman spectra shows that after irradiation the intensity of D-peak (at 1350 cm^{-1}), which is negligible in pristine graphene, increases. However, there is a drastic decrease in the intensity of 2D-peak (at 2700 cm^{-1}) indicating the breaking of translational symmetry of the sp^2 carbon bonds in graphene. The ratio of D-peak and G-peak (I$_D$/I$_G$) is lower in FG as compared to the DG which indicates lesser number of structural disorder in FG. To analyze and understand the structures in more details, STM calculation were performed on FG sample which indicates that the fluorine atoms are localized near to the defects created by irradiation.

4.5.2 Fluorination of graphene from materials modeling

Table 4.6. *Adsorption energies of fluorine on pristine graphene as well as the edge carbon atoms surrounding defects. Reprinted from Paper IX.*

Structure	E_{abs} (eV)	Hybridization
Pristine	-1.91	sp^3
Divacancy site A	-2.86	sp^3
Divacancy site B	-2.25	sp^3
Hole defect site C (dangling bond)	-5.64	sp^2
Hole defect site D	-2.18	sp^3

In order to investigate the adsorption behavior of fluorine atoms on defected graphene, we have performed *ab-initio* density functional theory calculations. Following the STM experiments, we have considered two different type of defects to model our simulations. These two models are – i) divacancy model and ii) hole-defect model which are shown in Fig. 4.15. There are four different possible places (marked as site A–D) where a single fluorine atom can be adsorbed. In Table 4.6 we have tabulated the adsorption energies for fluorine atom in these four sites. From the Table 4.6, it can be clearly seen that the adsorption energies for fluorine atom are quite lower around the defected sites as compared to the pristine graphene. It suggest that fluorine atoms are more prone to react with the carbon atoms surrounding the defect sites. At site C, due to the presence of dangling bond at the carbon atom, the adsorption energy
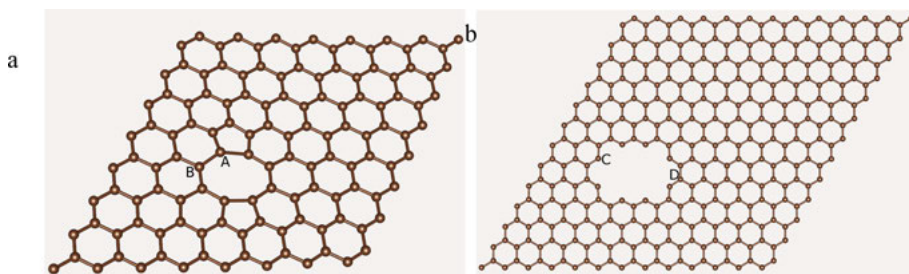
Figure 4.15. *Ab-initio* density functional calculation models of fluorinated graphene. Di-vacancy model (a) and hole-defect model (b), 0.95 nm in length, are based on the STM observations. Adsorption energies are shown in table 4.6. Reprinted from Paper IX.

of fluorine at this site is much lower compare to others. Here the carbon fluorine bond length is 1.36 Å, which is typical for a sp^2 hybridization and this bond has in-plane orientation. In other adsorption sites a sp^3 hybridization can be observed.

Part III:
Final Conclusions

5. Summary and Outlook

*"Would you tell me, please, which way I ought
to go from here?"*
*"That depends a good deal on where you want
to get to," said the Cat.*

— Lewis Carroll, Alice in Wonderland

The material research to find out suitable materials for beyond silicon electronics has become a predominant part in various aspects of science and technology in the 21st century. Graphene and other "beyond graphene" family of materials are among the many promising candidates in this regard. However, it is experimentally challenging to produce these materials in large scale quantity without incorporating any defects or impurities. From the device fabrication point of view, these defects or impurities can be either beneficial e.g., modification of material properties to get a desired outcome, or detrimental e.g., creating scattering states in electronic current transport. Hence, a proper understanding of the repercussions caused by these impurities and defects on these materials is extremely important. Therefore, the research work carried out in this thesis was focused on the effects of impurities and defects in modifying the properties of graphene and its derivatives, silicene and transition metal dichalcogenides for applications ranging from solar cells, nanoelectronics, optoelectronics, gas sensors, spintronics, etc.

We have mainly focused on the results of metallic impurities in graphene and its derivative structures in Chapter 3. We have also looked into the properties of quasiperiodic graphene and hexagonal boron nitride hybrid heterostructure systems to solve the classic band gap problem of graphene. In Chapter 4, we have discussed how defects affect the properties of graphene, silicene and transition metal dichalcogenides. Paying attention to spintronics and magnetic device applications, we have used single or small nanostructures of Fe as our choice of transition metal impurities.

In our study of single and a pair of Fe atoms in graphene/*graphane* interface structures shows that the responses of the magnetic impurities are different in "armchair" and "zigzag" channels. While the magnetic response is localized in the armchair channel, it is delocalized in the zigzag channel. An in-plane easy axis with relatively large magnetic anisotropy energy can be observed in the armchair channel. The Fe atoms strongly interact with the zigzag channel and hence a stronger ferromagnetic coupling between the the Fe atoms can

be observed. A possibility of realizing a spin gapless semiconductor material by doping appropriate magnetic impurities have been observed in the armchair channel. In the conducting zigzag channel, magnetic interaction between two impurities shows oscillating coupling across the edge for a specific width. Hence, a possibility of creating ultrathin device with fascinating properties has been discussed.

In our study of reconstructed zigzag graphene nanoribbons, we have shown that the reconstructed zigzag edges behave as metal and it does not show any magnetism. Using single and double hydrogen atoms, chemical functionalization of the edges are possible. However, the functionalization using two hydrogen atoms are preferable than the one. To introduce magnetism, we have also functionalize the edges with Fe chains which shows a variation of inter edge magnetic coupling between ferromagnetic and antiferromagnetic.

From the study of diffusion of Fe nanostructures on 2D hybrid structures of graphene and h–BN, we have shown that the diffusion barriers have smaller values on the h–BN part as compare to those in graphene part. Using in-depth *ab-initio* molecular dynamics simulations at room temperature (300 K), we conclude that mobile Fe adatoms form Fe clusters and they are eventually settled at the C–B interface. We predict that the artificially designed 2D hybrids of graphene and h–BN may act as potential substrates for spontaneous formation of magnetic structures at C–B interfaces.

We have also studied the properties of 3D quasiperiodic arrangements of grpahene and hexagonal boron nitride and demonstrated that these arrangements are more stable than their counterpart 1:1 periodic arrangement. We have shown that an opening of band gap is possible using certain sequences of Fibonacci stacking.

We have also shown that in pure graphene, the formation of correlated vacancy is facilitated. Molecular dynamics study revealed that the adsorbed Fe adatoms form clusters in a very short time scale and get trapped at the vacancy sites. It is also observed that the Fe clusters promote vacancy formation, i. e., it becomes easier to remove C atoms from the graphene lattice in presence of Fe. The strong adsorption of Fe clusters at the vacancy sites produces anisotropy in geometries and spin densities. Hence, a strong variation of local spin-dipole moments (parallel or antiparallel to the spin moments) yields a significant variation in the effective moments, which are measurable in XMCD experiments. The analyses of magnetic anisotropy energies reveal that for some of the cluster sizes, out-of-plane easy axes of magnetization are stabilized with a moderately large MAE, which could be important for magnetic data storage.

In our extensive study of native defects in transitional metal dichalcogenides (MX_2; M=Mo, W; X=S, Se, Te) we have found out that X interstitial defect is the most probable defects that will form under X rich conditions. However, under M rich environment, X vacancy is the energetically most favored defect except MTe$_2$ systems. M atom related defects have in general quite high formation energy leading to the formation of these defects in MX_2 systems un-

likely. These defect states appear in the gap region in general and suitably designed defected systems can be a good source for making light emitting devices.

Analysis of defect formation energies in graphene and silicene indicate that the formation of defects will be much easier in the latter material. STM simulations indicate that it will be difficult to distinguish defects in buckled silicene structure using STM and measuring $I - V$ characteristics can be a way around. Presence of these defects causes scattering leading to increment of local current densities which can cause heating and possible deterioration in device performance.

Our experiments and theoretical simulations confirm that the gaseous NO_2 molecule bind strongly with defected graphene which in turn increases the sensitivity of graphene to NO_2 gas molecule with a factor of three. Hence we speculate that defected graphene will be a very good candidate for gas sensing purpose. Deliberate creation of defects using ion bombardment can also facilitate the local site selective functionalization of graphene with Fluorine atoms.

5.1 Future prospects

The computational techniques that I have learned during my Ph. D can be used to investigate various other interesting properties of graphene and other 2D materials. Graphene has been called "wonder material" after its experimental realization in 2004. Since then, a tremendous effort has been put in graphene research to use these 2D materials in commercial products. Despite that, it remains challenging to use graphene in large commercial quantities. Recently, Briggs Automotive Company launched a new model of car called "Mono" with panels made out of graphene. But, still in 2016 and in coming years the research and prototype phase of graphene will continue. It may take decades to make graphene a commercial success. Hence, the research on 2D materials has become a rapidly increasing field. There are almost 40 possible transition metal dichalcogenides (TMDs) possible as depicted in Fig. 5.1. However, There are other 2D materials like silicene, phosphorene, etc., which have various interesting properties. Hybrid 2D planar or 3D heterostructures using various TMDs and other 2D materials are also becoming quite promising in this regard.

One of the major issues that the 2D materials researches are facing is to produce large defect free materials in a cost effective way. Hence understanding of these vast number 2D pristine systems as well as systems with various defects and impurities such as line defects, grain boundaries, etc. are quite important. As a future project, I want to continue my research in the field of 2D materials keeping in mind various applications oriented goal. The realization of practical devices relies on understanding of electron transport in these
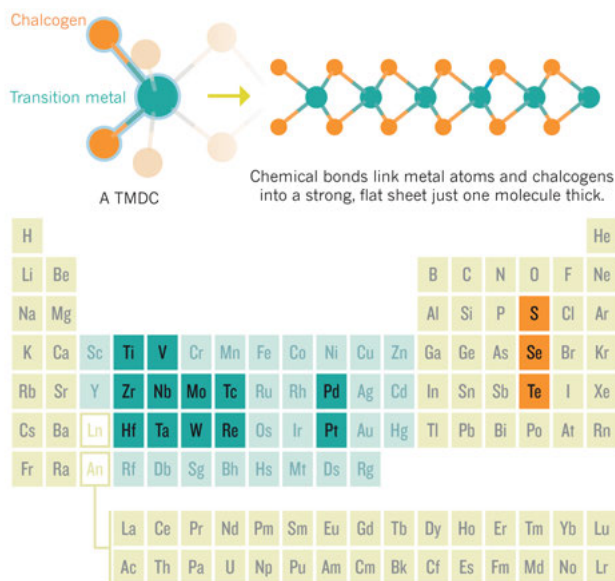
Figure 5.1. Various possible combination of transition metal dichalcogenides containing one transition-metal atom (green) for every two chalcogen atoms (orange). Reprinted by permission from Macmillan Publishers Ltd: Nature News ([33]), copyright © (2015).

systems, both pristine and with defects and impurities. Thus, it will be important to focus on transport calculations in these systems. Besides transport through 2D materials, another important aspect is to use them as ultrathin electrodes to send electrons through quantum dots or even a single molecule. In this case, the challenging aspects are the treatment of electron correlation in describing the electronic structure of the scattering region, effects of vibration via electron-phonon coupling to describe inelastic processes etc. The development of non-equilibrium transport under a finite bias taking into consideration the above-mentioned aspects within the framework of ab-initio theory will also be my interest.

Exciton, particularly prominently observed in disordered and low dimensional materials such as TMDs and some other group-IV sulfide materials, is a quasiparticle excitation consisting of a bound electron-hole pair that mediates the absorption and emission of light. Fig. 5.2 shows a schematic representation of exciton. The presence of a localized defect state in the band gap will significantly affect the excitonic properties as depicted in the figure. Hence, an advancement in studying the optical properties of these system can be carried out by including the effects of exciton with the help of Bethe-Salpeter equation. These advanced computational studies will be computationally demanding due to the nature of the research problems and the choice of materials.
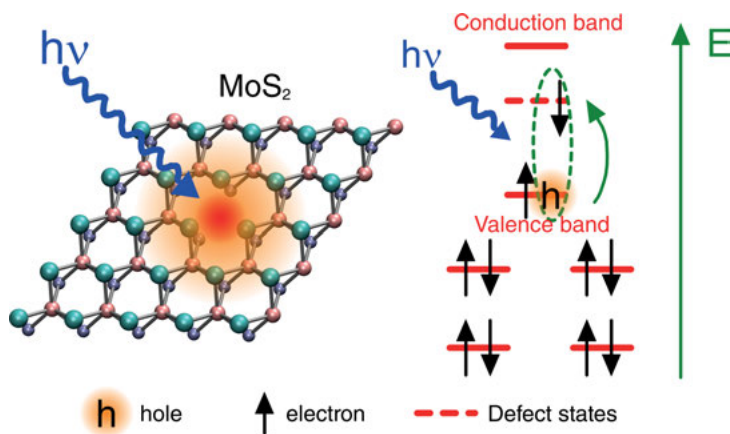
Figure 5.2. Schematic diagram to illustrate excitonic effects. The MoS_2 figure is adapted with permission from Paper VI. Copyright ©2015 American Physical Society.

Hence, availability of next generation computing resources as well as numerical codes with advanced techniques are quite necessary. Also, the experiments are needed to carry out in order to confirm various theoretical findings which can become extremely challenging as in many cases, the manipulation of properties is need to be done in an atomic scale.

6. Populärvetenskaplig sammanfattning

Elektronik, ett område inom vetenskap och teknik, behandlar elektroniska apparater tillverkade av olika elektriska komponenter, t.ex. vakuumrör, dioder, transistorer, integrerade kretsar (IC), etc. Elektronikuppfinningarnas historia sträcker sig tillbaks till 1745, då Kleist och Musschenbroek först uppfann "Leydenflaskan", vilken var den ursprungliga kondensatorn. Sedan dess har olika uppfinningar och upptäckter byggt en solid grund för utvecklingen av elektronik. Flemings upptäckt av dioden 1905 utlöste början av den moderna tidens starka präglan av elektroniken. Dioder och vakuumrör blev integrerade delar inom elektroniken under den tidiga delen av 20-talet och uppfinningen av dessa vakuumrör har gjort teknik så som radio, TV, telefonnät, datorer, etc. mycket populära och utbredda. Men användningen av vakuumrör gjorde dessa tekniker kostsamma och anordningarna skrymmande.

Miniatyrisering av moderna elektroniska apparater har alltid fascinerat människor i allmänhet. De halvledarkomponenter som uppfanns under 1940-talet gjorde det möjligt att tillverka mindre, mer hållbara, billigare och effektivare fasta-tillsånds enheter än vakuumrör. Därför började dessa fasta-tillsånds enheter, så som transistorer, gradvis att ersätta vakumrören på 1950-talet. I jakten på mindre storlek upfanns integrerade kretsar (IC). Möjligheten att minska storleken för dagens moderna elektroniska apparater är starkt beroend av möjligheten att minska storleken hos dessa integrerade kretsarna (IC), vilka är deras hjärtan och hjärnor.

Kiselbaserade integrerade kretsar har begränsningar för hur små de kan göras. Strävan efter nya material och tekniker som har möjlighet att ersätta kisel pågår därför redan. Bland flera andra alternativ har grafen, vilket består av ett tvådimensionellt (2D) monolager av kolatomer ordnade i ett hexagonalt gitter, blivit det mest lovande. Men även om grafen har några extraordinära egenskaper så gjorde avsaknaden av ett bandgap grafen olämpliga för transistorapplikationer. Detta har lett forskare till att leta efter andra 2D-material med lämpliga egenskaper där ström genom materialet kan slås "PÅ" och "AV". Bildandet av defekter och föroreningar i dessa 2D-material är en del av tillverkningsprocessen och kan inte undvikas. Dessa defekter och föroreningar påverkar egenskaperna hos dessa material. Å ena sidan kan dessa defekter och föroreningar förstöra elektriska egenskaper, å andra sidan kan de på nanoskala introducera nya egenskaper som kan vara till nytta för att skapa enheter för olika tillämpningar. Följaktligen måste det undersökas grundligt hur dessa defekter och föroreningar påverkar egenskaperna hos dessa material.

I denna avhandling har vi diskuterat effekten av föroreningar och defekter på grafen och andra 2D-material. Vi har använt ab-initio täthetsfunktionalteoribaserade datorsimuleringar för att analysera de strukturella och elektroniska egenskaperna hos dessa system. Bortsett från 2D material så som grafen, silicene och övergångsmetalldichalcogenides (TMDC) har vi använt både 2D och 3D hybridstrukturer som härstammar från 2D material. Olika 2D material så som grafen, hydrerad grafen(grafan) och hexagonal bornitrid (h-BN) är antingen staplade i 3D eller 2D för att bilda dessa hybridstrukturer. Som orenhet har vi i vår studie studerat en enstaka järnatom eller en grupp av järnatomer. Hybridstrukturer av grafen-grafan kan likna grafennanoband och visar intressanta magnetiska egenskaper i närvaro av järnföroreningar. Med hjälp av kantrekonstruktion kan sicksacks-grafennanoband visa kantmetallicitet. 2D-(plana) och 3D-hybridstrukturer av grafen och h-BN visar också intressanta egenskaper. Öppnande av bandgap är möjligt med hjälp av vissa specifika arrangemang av 3D kvasiperiodisk stapling av grafen och h-BN, och dessa strukturer är mer stabila än normalt återkommande stapling. Plana hybridstrukturer kan fånga järnkluster på kol-bor-gränssnitt och därmed kan dessa strukturer fungera som potentiella substratmaterial för att bilda magnetiska nanostrukturer.

Vakanserna i grafen föredrar att bildas på ett korrelerat sätt vilket underlättar adsorption av föroreningsatomer så som järnatomer, vilka tenderar att bilda kluster som fastna på de vakanta platserna. Detta är i motsats till den mycket diffusiva situationen på rent grafen och därmed kan dessa magnetiska enheter tillhandahålla stabila magnetiska moment som är användbara för att lagra information.

Tillsammans med experimentalister har vi etablerat att defekter i grafen även hjälper med platsselektiv lokal fluorering och adsorption av gasformigt NO_2. Skapandet av defekter i grafen ökar NO_2 känsligheten hos grafen och sålunda kommer det att vara användbart som en gaskänslig anordning. Även om defekter kan hjälpa i vissa tillämpningar så visar våra elektroniska transportberäkningar att defekter även kommer leda till spridning. Denna spridning kommer att leda till en ökning i lokal ström och värme, vilket kan leda till försämrad prestanda för enheter. I vår systematiska studie av olika defekter i olika TMDCs har vi visat att defektsignaturer lätt kan ses i strukturella, elektroniska och optiska egenskaper.

I ett nötskal diskuterar denna avhandling olika aspekter av orenheter och defekter i grafen och relaterade 2D-material. Vi har diskuterat hur dessa antingen kan vara skadliga eller till nytta i olika enhetsapplikationer. I framtiden vill vi ytterligare utöka våra studier för att studera effekterna av linjedefekter, korngränser i TMDCs. Ett annat intressant ämne skulle vara att studera excitoner, som är bundna tillstånd av elektroner och hål, och deras signaturer i det optiska spektrumet i närvaron av lokala defekter.

Acknowledgments

"Knowledge is in the end based on acknowledgment."

— Ludwig Wittgenstein

I would like to take this opportunity to express my sincere appreciation to every person who has supported me during my Ph. D studies at the Division of Materials Theory, Department of Physics & Astronomy at Uppsala University. The task was Herculean and difficult to accomplish without the guidance of my advisers, Dr. Biplab Sanyal and Prof. Olle Eriksson. They were always supportive of my work and open to various new ideas and discussions. Their support, advice, encouragement and particularly providing a dynamic research environment to work helped me to complete the Ph. D studies and resulted in a continuous improvement of my scientific knowledge. Therefore, I would like to thank both of them. Special thanks goes to Biplab-da for his critical suggestions and analytic comments during our both formal, and informal discussions.

I am deeply thankful to both Prof. Dilip Kanhere and Prof. Anjali Kshirsagar, my previous advisers, who introduced me in the field of computational material physics and Density Functional Theory. I am extremely thankful to Prof. Kanhere, who has always supported and encouraged me in all aspects.

I would also like to sincerely acknowledge all my collaborators, Prof. Kanhere, Prof. Leifer, Prof. Sen, Prof. Rocha, Prof. Ottoson, for giving me the opportunity to become part of various fruitful and challenging scientific collaborations. Thanks to Heike, Barbara, Ralph, Rodrigo, Hu, Iulia, Hakkim, Manoj, Raffaello, Kjell, Johann, Sumanta, Bhalchandra, Prachi, Pooja for the valuable discussions that I had with them and the feed backs that I received from them were always helpful in broadening my knowledge. I am also grateful to Kristofer for his extensive help in translating the thesis summary in Swedish. It is definitely worth mentioning my proof-reading friends, Ritwik, Vivek, Pralay and Rudra to whom I am truly thankful for their help in improving this thesis. A special acknowledgment goes to the Knut and Alice Wallenberg foundation (KAW) which provided the financial support for my Ph. D studies.

My most sincere thanks to my office mates, Sumanta and Vancho, for providing such a lively office environment and for all the fun, jokes, discussions and activities we did together. Special thanks goes to Vancho for organizing so many fun activities including the long road trips in Iceland, Spain, Paris and Macedonia. A very special thanks to Sumanta, Ritwik, Amitava

References

[1] C. Susskind, Spectrum, IEEE **3**, 72 (1966).

[2] L. Venema, Nature **479**, 309 (2011).

[3] P. R. Wallace, Phys. Rev. **71**, 622 (1947).

[4] K. S. Novoselov, A. K. Geim, S. V. Morozov, D. Jiang, Y. Zhang, S. V. Dubonos, I. V. Grigorieva, and A. A. Firsov, Science **306**, 666 (2004).

[5] J. C. Slonczewski and P. R. Weiss, Phys. Rev. **109**, 272 (1958).

[6] J. W. McClure, Phys. Rev. **104**, 666 (1956).

[7] J.-H. Chen, C. Jang, S. Xiao, M. Ishigami, and M. S. Fuhrer, Nat Nano **3**, 206 (2008).

[8] A. Akturk and N. Goldsman, Journal of Applied Physics **103**, 053702 (2008).

[9] A. K. Geim and K. S. Novoselov, Nat Mater **6**, 183 (2007).

[10] A. H. Castro Neto, F. Guinea, N. M. R. Peres, K. S. Novoselov, and A. K. Geim, Rev. Mod. Phys. **81**, 109 (2009).

[11] Y. Zhang, Y.-W. Tan, H. L. Stormer, and P. Kim, Nature **438**, 201 (2005).

[12] K. S. Novoselov, E. McCann, S. V. Morozov, V. I. Fal/'ko, M. I. Katsnelson, U. Zeitler, D. Jiang, F. Schedin, and A. K. Geim, Nat Phys **2**, 177 (2006).

[13] M. I. Katsnelson, The European Physical Journal B - Condensed Matter and Complex Systems **51**, 157 (2006).

[14] K. S. Novoselov, A. K. Geim, S. V. Morozov, D. Jiang, M. I. Katsnelson, I. V. Grigorieva, S. V. Dubonos, and A. A. Firsov, Nature **438**, 197 (2005).

[15] M. I. Katsnelson, K. S. Novoselov, and A. K. Geim, Nat Phys **2**, 620 (2006).

[16] X. Li, X. Wang, L. Zhang, S. Lee, and H. Dai, Science **319**, 1229 (2008).

[17] J. O. Sofo, A. S. Chaudhari, and G. D. Barber, Phys. Rev. B **75**, 153401 (2007).

[18] R. M. Ribeiro, N. M. R. Peres, J. Coutinho, and P. R. Briddon, Phys. Rev. B **78**, 075442 (2008).

[19] E. Bekyarova, M. E. Itkis, P. Ramesh, C. Berger, M. Sprinkle, W. A. de Heer, and R. C. Haddon, Journal of the American Chemical Society **131**, 1336 (2009).

[20] P. A. Denis, R. Faccio, and A. W. Mombru, ChemPhysChem **10**, 715 (2009).

[21] D. C. Elias, R. R. Nair, T. M. G. Mohiuddin, S. V. Morozov, P. Blake, M. P. Halsall, A. C. Ferrari, D. W. Boukhvalov, M. I. Katsnelson, A. K. Geim, and K. S. Novoselov, Science **323**, 610 (2009).

[22] Y.-W. Son, M. L. Cohen, and S. G. Louie, Phys. Rev. Lett. **97**, 216803 (2006).

[23] Y.-W. Son, M. L. Cohen, and S. G. Louie, Nature **444**, 347 (2006).

[24] M. Y. Han, B. Özyilmaz, Y. Zhang, and P. Kim, Phys. Rev. Lett. **98**, 206805 (2007).

[25] L. Jiao, L. Zhang, X. Wang, G. Diankov, and H. Dai, NATURE **458**, 877 (2009).

[26] R. Martinazzo, S. Casolo, and G. F. Tantardini, Phys. Rev. B **81**, 245420 (2010).

[27] F. Banhart, J. Kotakoski, and A. V. Krasheninnikov, ACS Nano **5**, 26 (2011).

[28] A. Hashimoto, K. Suenaga, A. Gloter, K. Urita, and S. Iijima, Nature **430**, 870 (2004).

[29] M. H. Gass, U. Bangert, A. L. Bleloch, P. Wang, R. R. Nair, and G. K., Nat Nano **3**, 676 (2008).

[30] S. H. M. Jafri, K. Carva, E. Widenkvist, T. Blom, B. Sanyal, J. Fransson, O. Eriksson, U. Jansson, H. Grennberg, O. Karis, R. A. Quinlan, B. C. Holloway, and K. Leifer, J. Phys. D: Appl. Phys. **43**, 045404 (2010).

[31] V. A. Coleman, R. Knut, O. Karis, H. Grennberg, U. Jansson, R. Quinlan, B. C. Holloway, B. Sanyal, and O. Eriksson, J. Phys. D: Appl. Phys. **48**, 062001 (2008).

[32] K. Carva, B. Sanyal, J. Fransson, and O. Eriksson, Phys. Rev. B **81**, 245405 (2010).

[33] E. Gibney, Nature **522**, 274 (2015).

[34] V. O. Özçelik and S. Ciraci, The Journal of Physical Chemistry C **117**, 2175 (2013).

[35] Z. a. Piazza, H.-S. Hu, W.-L. Li, Y.-F. Zhao, J. Li, and L.-S. Wang, Nat. Commun. **5**, 1 (2014).

[36] A. J. Mannix, X.-F. Zhou, B. Kiraly, J. D. Wood, D. Alducin, B. D. Myers, X. Liu, B. L. Fisher, U. Santiago, J. R. Guest, M. J. Yacaman, A. Ponce, A. R. Oganov, M. C. Hersam, and N. P. Guisinger, Science **350**, 1513 (2015).

[37] P. Bampoulis, L. Zhang, A. Safaei, R. van Gastel, B. Poelsema, and H. Zandvliet, Journal of Physics: Condensed Matter **26**, 442001 (2014).

[38] L. Tao, E. Cinquanta, D. Chiappe, C. Grazianetti, M. Fanciulli, M. Dubey, A. Molle, and D. Akinwande, Nat. Nanotechnol. **10**, 1 (2015).

[39] G. L. Lay, P. D. Padova, A. Resta, T. Bruhn, and P. Vogt, Journal of Physics D: Applied Physics **45**, 392001 (2012).

[40] B. Aufray, A. Kara, S. Vizzini, H. Oughaddou, C. Léandri, B. Ealet, and G. Le Lay, Applied Physics Letters **96**, 183102 (2010).

[41] L. Takahashi and K. Takahashi, Phys. Chem. Chem. Phys. **17**, 21394 (2015).

[42] L. Li, Y. Yu, G. J. Ye, Q. Ge, X. Ou, H. Wu, D. Feng, X. H. Chen, and Y. Zhang, Nat. Nanotechnol. **9**, 372 (2014).

[43] S. Berner, M. Corso, R. Widmer, O. Groening, R. Laskowski, P. Blaha, K. Schwarz, A. Goriachko, H. Over, S. Gsell, M. Schreck, H. Sachdev, T. Greber, and J. Osterwalder, Angew. Chemie - Int. Ed. **46**, 5115 (2007).

[44] E. Bianco, S. Butler, S. Jiang, O. D. Restrepo, W. Windl, and J. E. Goldberger, ACS Nano **7**, 4414 (2013), pMID: 23506286.

[45] A. D. Wilson, J. A.; Yoffe, Adv. Phys. **18**, 193 (1969).

[46] R. F. Frindt, J. Appl. Phys. **37**, 1928 (1966).

[47] P. Joensen, R. Frindt, and S. Morrison, Mater. Res. Bull. **21**, 457 (1986).

[48] K. S. Novoselov, D. Jiang, F. Schedin, T. J. Booth, V. V. Khotkevich, S. V. Morozov, and A. K. Geim, Proceedings of the National Academy of Sciences of the United States of America **102**, 10451 (2005).

[49] K. Watanabe, T. Taniguchi, and H. Kanda, Nat Mater **3**, 404 (2004).

[50] T. Georgiou, R. Jalil, B. D. Belle, L. Britnell, R. V. Gorbachev, S. V. Morozov, Y. J. Kim, A. Gholinia, S. J. Haigh, O. Makarovsky, L. Eaves, L. A. Ponomarenko, A. K. Geim, K. S. Novoselov, and A. Mishchenko, Nat.

Nanotechnol. **8**, 100 (2013).

[51] G. T. Feliciano, C. Sanz-Navarro, M. D. Coutinho-Neto, P. Ordejón, R. H. Scheicher, and A. R. Rocha, Phys. Rev. Appl. **3**, 1 (2015).

[52] G. L. Lay, Nat. Nanotechnol. **10**, 202 (2015).

[53] J. Prasongkit, R. G. Amorim, S. Chakraborty, R. Ahuja, R. H. Scheicher, and V. Amornkitbamrung, J. Phys. Chem. C **119**, 16934 (2015).

[54] H. S. Song, S. L. Li, H. Miyazaki, S. Sato, K. Hayashi, A. Yamada, N. Yokoyama, and K. Tsukagoshi, Sci. Rep. **2**, 337 (2012).

[55] T. Niu, M. Zhou, J. Zhang, Y. Feng, and W. Chen, J. Am. Chem. Soc. **135**, 8409 (2013).

[56] X. Zou and B. I. Yakobson, Acc. Chem. Res. **48**, 73 (2015).

[57] J. C. Meyer, C. Kisielowski, R. Erni, M. D. Rossell, M. F. Crommie, and A. Zettl, Nano Letters , 3582 (2008).

[58] M. M. Ugeda, I. Brihuega, F. Guinea, and J. M. Gómez-Rodríguez, Physical Review Letters **104**, 96804 (2010).

[59] A. R. Rocha, T. B. Martins, A. Fazzio, and A. J. R. Da Silva, Nanotechnology **21**, 345202 (2010).

[60] C. Xu, G. Luo, Q. Liu, J. Zheng, Z. Zhang, S. Nagase, Z. Gao, and J. Lu, Nanoscale **4**, 3111 (2012).

[61] N. Ooi, A. Rairkar, L. Lindsley, and J. B. Adams, Journal of Physics: Condensed Matter **18**, 97 (2006).

[62] K. Yuge, Phys. Rev. B **79**, 144109 (2009).

[63] J. Zhu, S. Bhandary, B. Sanyal, and H. Ottosson, The Journal of Physical Chemistry C **115**, 10264 (2011).

[64] J. da Rocha Martins and H. Chacham, ACS Nano **5**, 385 (2011).

[65] A. Ramasubramaniam and D. Naveh, Phys. Rev. B **84**, 075405 (2011).

[66] J.-W. Jiang, J.-S. Wang, and B.-S. Wang, Applied Physics Letters **99**, 043109 (2011).

[67] S. Bhowmick, A. K. Singh, and B. I. Yakobson, The Journal of Physical Chemistry C **115**, 9889 (2011).

[68] J. M. Pruneda, Phys. Rev. B **81**, 161409 (2010).

[69] L. Ci, L. Song, C. Jin, D. Jariwala, D. Wu, Y. Li, A. Srivastava, Z. F. Wang, K. Storr, L. Balicas, F. Liu, and P. M. Ajayan, Nat Mater **9**, 430 (2010).

[70] Z. Liu, L. Ma, G. Shi, W. Zhou, Y. Gong, S. Lei, X. Yang, J. Zhang, J. Yu, K. P. Hackenberg, A. Babakhani, J.-C. Idrobo, R. Vajtai, J. Lou, and P. M. Ajayan, Nat Nano **8**, 119 (2013).

[71] P. Sutter, R. Cortes, J. Lahiri, and E. Sutter, Nano Letters **12**, 4869 (2012).

[72] G. Fiori, A. Betti, S. Bruzzone, and G. Iannaccone, ACS Nano **6**, 2642 (2012).

[73] K. Nakada, M. Fujita, G. Dresselhaus, and M. S. Dresselhaus, Phys. Rev. B **54**, 17954 (1996).

[74] P. Koskinen, S. Malola, and H. Häkkinen, Phys. Rev. Lett. **101**, 115502 (2008).

[75] P. Koskinen, S. Malola, and H. Häkkinen, Phys. Rev. B - Condens. Matter Mater. Phys. **80**, 073401 (2009).

[76] X. Jia, M. Hofmann, V. Meunier, B. G. Sumpter, J. Campos-Delgado, J. M. Romo-Herrera, H. Son, Y. P. Hsieh, A. Reina, J. Kong, M. Terrones, and M. S. Dresselhaus, Science (80-.). **323**, 1701 (2009).

[77] Ç. Ö. Girit, J. C. Meyer, R. Erni, M. D. Rossell, C. Kisielowski, L. Yang, C.-H. Park, M. F. Crommie, M. L. Cohen, S. G. Louie, and A. Zettl, Science **323**, 1705 (2009).

[78] M. Born and R. Oppenheimer, Annalen der Physik **84**, 0457 (1927).

[79] L. H. Thomas, Mathematical Proceedings of the Cambridge Philosophical Society **23**, 542 (1927).

[80] E. Fermi, Rend. Accad. Naz. Lincei **6**, 602 (1927).

[81] P. A. M. Dirac, Mathematical Proceedings of the Cambridge Philosophical Society **26**, 376 (1930).

[82] P. Hohenberg and W. Kohn, Phys. Rev. **136**, B864 (1964).

[83] R. M. Martin, *Electronic Structure* (Cambridge University Press, 2004) cambridge Books Online.

[84] W. Kohn and L. J. Sham, Phys. Rev. **140**, A1133 (1965).

[85] D. M. Ceperley and B. J. Alder, Phys. Rev. Lett. **45**, 566 (1980).

[86] J. P. Perdew and A. Zunger, Phys. Rev. B **23**, 5048 (1981).

[87] J. P. Perdew and Y. Wang, Phys. Rev. B **45**, 13244 (1992).

[88] I. I. Mazin, M. D. Johannes, L. Boeri, K. Koepernik, and D. J. Singh, Phys. Rev. B **78**, 085104 (2008).

[89] P. Haas, F. Tran, and P. Blaha, Phys. Rev. B **79**, 085104 (2009).

[90] J. P. Perdew, J. A. Chevary, S. H. Vosko, K. A. Jackson, M. R. Pederson, D. J. Singh, and C. Fiolhais, Phys. Rev. B **46**, 6671 (1992).

[91] J. P. Perdew, K. Burke, and M. Ernzerhof, Phys. Rev. Lett. **77**, 3865 (1996).

[92] J. P. Perdew, K. Burke, and M. Ernzerhof, Phys. Rev. Lett. **78**, 1396 (1997).

[93] J. P. Perdew, International Journal of Quantum Chemistry **28**, 497 (1985).

[94] J. P. Perdew, International Journal of Quantum Chemistry **30**, 451 (1986).

[95] F. Bloch, Zeitschrift für Physik **52**, 555 (1929).

[96] V. Heine (Academic Press, 1970) pp. 1 – 36.

[97] P. E. Blöchl, Phys. Rev. B **50**, 17953 (1994).

[98] G. Kresse and J. Hafner, Phys. Rev. B **47**, 558 (1993).

[99] G. Kresse and J. Furthmüller, Phys. Rev. B **54**, 11169 (1996).

[100] P. Chandrachud, B. S. Pujari, S. Haldar, B. Sanyal, and D. G. Kanhere, J. Phys. Condens. Matter **22**, 465502 (2010).

[101] A. K. Singh and B. I. Yakobson, Nano Lett. **9**, 1540 (2009).

[102] P. Sessi, J. R. Guest, M. Bode, and N. P. Guisinger, Nano Lett. **9**, 4343 (2009).

[103] Y. H. Lu and Y. P. Feng, J. Phys. Chem. C **113**, 20841 (2009).

[104] R. Balog, B. Jørgensen, L. Nilsson, M. Andersen, E. Rienks, M. Bianchi, M. Fanetti, E. Lægsgaard, A. Baraldi, S. Lizzit, Z. Sljivancanin, F. Besenbacher, B. Hammer, T. G. Pedersen, P. Hofmann, and L. Hornekær, Nat. Mater. **9**, 315 (2010).

[105] Z. M. Ao, A. D. Hernández-Nieves, F. M. Peeters, and S. Li, Appl. Phys. Lett. **97**, 233109 (2010), 1011.4167 .

[106] S. R. Power, V. M. De Menezes, S. B. Fagan, and M. S. Ferreira, Phys. Rev. B - Condens. Matter Mater. Phys. **84**, 195431 (2011), 1108.6199 .

[107] Y. Wang and H. P. Cheng, Phys. Rev. B **83**, 113402 (2011).

[108] H. Valencia, A. Gil, and G. Frapper, J. Phys. Chem. C **114**, 14141 (2010).

[109] L. Pisani, J. A. Chan, B. Montanari, and N. M. Harrison, Phys. Rev. B **75**, 064418 (2007).

[110] O. V. Yazyev, Reports on Progress in Physics **73**, 056501 (2010).

[111] J. Kunstmann, C. Özdoğan, A. Quandt, and H. Fehske, Phys. Rev. B **83**, 045414 (2011).

[112] S. Bhandary, O. Eriksson, B. Sanyal, and M. I. Katsnelson, Phys. Rev. B - Condens. Matter Mater. Phys. **82**, 165405 (2010).

[113] T. Wassmann, A. P. Seitsonen, A. M. Saitta, M. Lazzeri, and F. Mauri, Phys. Rev. Lett. **101**, 096402 (2008), 0808.2283 .

[114] J. M. W. Chase, J. Phys. Chem. Ref. Data, Monog. **9**, (1998).

[115] Y. Wang and H.-P. Cheng, Phys. Rev. B **83**, 113402 (2011).

[116] P. Srivastava, M. Deshpande, and P. Sen, Physical chemistry chemical physics : PCCP **13**, 21593 (2011).

[117] G. Henkelman and H. Jónsson, The Journal of Chemical Physics **113**, 9978 (2000).

[118] G. Henkelman, B. P. Uberuaga, and H. Jónsson, The Journal of Chemical Physics **113**, 9901 (2000).

[119] A. Zobelli, C. P. Ewels, A. Gloter, and G. Seifert, Phys. Rev. B **75**, 094104 (2007).

[120] C. R. Dean, a. F. Young, I. Meric, C. Lee, L. Wang, S. Sorgenfrei, K. Watanabe, T. Taniguchi, P. Kim, K. L. Shepard, and J. Hone, Nat. Nanotechnol. **5**, 722 (2010), 1005.4917 .

[121] W. Yang, G. Chen, Z. Shi, C.-C. Liu, L. Zhang, G. Xie, M. Cheng, D. Wang, R. Yang, D. Shi, K. Watanabe, T. Taniguchi, Y. Yao, Y. Zhang, and G. Zhang, Nat. Mater. **12**, 792 (2013).

[122] G. Giovannetti, P. A. Khomyakov, G. Brocks, P. J. Kelly, and J. van den Brink, Phys. Rev. B **76**, 073103 (2007).

[123] S. J. Haigh, A. Gholinia, R. Jalil, S. Romani, L. Britnell, D. C. Elias, K. S. Novoselov, L. A. Ponomarenko, A. K. Geim, and R. Gorbachev, Nat. Mater. **11**, 764 (2012), 1206.6698 .

[124] L. A. Ponomarenko, A. K. Geim, A. A. Zhukov, R. Jalil, S. V. Morozov, K. S. Novoselov, I. V. Grigorieva, E. H. Hill, V. Cheianov, V. Falko, K. Watanabe, T. Taniguchi, and R. V. Gorbachev, Nat. Phys. **7**, 958 (2011), 1107.0115 .

[125] P. Sutter, J. Lahiri, P. Zahl, B. Wang, and E. Sutter, Nano Lett. **13**, 276 (2013).

[126] A. Ramasubramaniam, D. Naveh, and E. Towe, Nano Lett. **11**, 1070 (2011), 1011.2489 .

[127] Y. Fan, M. Zhao, Z. Wang, X. Zhang, and H. Zhang, Applied Physics Letters **98**, 083103 (2011), http://dx.doi.org/10.1063/1.3556640.

[128] R. Quhe, J. Zheng, G. Luo, Q. Liu, R. Qin, J. Zhou, D. Yu, S. Nagase, W.-N. Mei, Z. Gao, and J. Lu, NPG Asia Mater. **4**, e16 (2012).

[129] J. M. Soler, E. Artacho, J. D. Gale, A. García, J. Junquera, P. Ordejón, and D. Sánchez-Portal, Journal of Physics: Condensed Matter **14**, 2745 (2002).

[130] S. Nosé, The Journal of Chemical Physics **81**, 511 (1984).

[131] S. Nosé, Progress of Theoretical Physics Supplement **103**, 1 (1991).

[132] D. M. Bylander and L. Kleinman, Phys. Rev. B **46**, 13756 (1992).

[133] B. Sanyal, O. Eriksson, U. Jansson, and H. Grennberg, Phys. Rev. B **79**, 113409 (2009).

[134] A. V. Krasheninnikov, P. O. Lehtinen, A. S. Foster, P. Pyykkö, and R. M. Nieminen, Phys. Rev. Lett. **102**, 126807 (2009).

[135] V. I. Anisimov, F. Aryasetiawan, and A. I. Lichtenstein, Journal of Physics: Condensed Matter **9**, 767 (1997).

[136] I. V. Solovyev, P. H. Dederichs, and V. I. Anisimov, Phys. Rev. B **50**, 16861 (1994).

[137] D. W. Boukhvalov and M. I. Katsnelson, Appl. Phys. Lett **95**, 023109 (2009).

[138] S. Yu, S. Chen, W. Zhang, L. Yu, and Y. Yin, Chem. Phys. Lett **446**, 217 (2007).

[139] G. L. Gustev and C. W. B. Jr., J. Phys. Chem. A **107**, 7013 (2003).

[140] R. Wu and A. Freeman, Physical Review Letters **73**, 1994 (1994).

[141] B. Lounis and M. Orrit, Reports on Progress in Physics **68**, 1129 (2005).

[142] W. Zhou, X. Zou, S. Najmaei, Z. Liu, Y. Shi, J. Kong, J. Lou, P. M. Ajayan, B. I. Yakobson, and J.-C. Idrobo, Nano Letters **13**, 2615 (2013), pMID: 23659662, http://dx.doi.org/10.1021/nl4007479 .

[143] J.-Y. Noh, H. Kim, and Y.-S. Kim, Phys. Rev. B **89**, 205417 (2014).

[144] B. Radisavljevic, A. Radenovic, J. Brivio, V. Giacometti, and A. Kis, Nature Nanotechnology **6**, 147 (2011).

[145] Y.-H. Lee, X.-Q. Zhang, W. Zhang, M.-T. Chang, C.-T. Lin, K.-D. Chang, Y.-C. Yu, J. T.-W. Wang, C.-S. Chang, L.-J. Li, and T.-W. Lin, Advanced Materials **24**, 2320 (2012).

[146] K. Q. Dang and D. E. Spearot, Journal of Applied Physics **116**, 013508 (2014).

[147] S. Tongay, J. Suh, C. Ataca, W. Fan, A. Luce, J. S. Kang, J. Liu, C. Ko, R. Raghunathanan, J. Zhou, F. Ogletree, J. Li, J. C. Grossman, and J. Wu, Sci. Rep. **3**, 2657 (2013).

[148] L. ping Feng, J. Su, and Z. tang Liu, Journal of Alloys and Compounds **613**, 122 (2014).

[149] M. Ghorbani-Asl, A. N. Enyashin, A. Kuc, G. Seifert, and T. Heine, Phys. Rev. B **88**, 245440 (2013).

[150] H.-P. Komsa, S. Kurasch, O. Lehtinen, U. Kaiser, and A. V. Krasheninnikov, Physical Review B **88**, 035301 (2013).

[151] H.-P. Komsa and A. V. Krasheninnikov, Physical Review B **91**, 125304 (2015).

[152] S. KC, R. C. Longo, R. Addou, R. M. Wallace, and K. Cho, Nanotechnology **25**, 375703 (2014).

[153] C. Ataca and S. Ciraci, The Journal of Physical Chemistry C **115**, 13303 (2011).

[154] X. Ling, Y.-H. Lee, Y. Lin, W. Fang, L. Yu, M. S. Dresselhaus, and J. Kong, Nano Letters **14**, 464 (2014).

[155] S. Wang, Y. Rong, Y. Fan, M. Pacios, H. Bhaskaran, K. He, and J. H. Warner, Chemistry of Materials **26**, 6371 (2014).

[156] X. Wang, Y. Gong, G. Shi, W. L. Chow, K. Keyshar, G. Ye, R. Vajtai, J. Lou, Z. Liu, E. Ringe, B. K. Tay, and P. M. Ajayan, ACS Nano **8**, 5125 (2014).

[157] N. R. Pradhan, D. Rhodes, S. Feng, Y. Xin, S. Memaran, B.-H. Moon, H. Terrones, M. Terrones, and L. Balicas, ACS Nano **8**, 5911 (2014).

[158] Y. Zhang, Y. Zhang, Q. Ji, J. Ju, H. Yuan, J. Shi, T. Gao, D. Ma, M. Liu, Y. Chen, X. Song, H. Y. Hwang, Y. Cui, and Z. Liu, ACS Nano **7**, 8963 (2013).

[159] J.-K. Huang, J. Pu, C.-L. Hsu, M.-H. Chiu, Z.-Y. Juang, Y.-H. Chang, W.-H. Chang, Y. Iwasa, T. Takenobu, and L.-J. Li, ACS Nano **8**, 923 (2014).

[160] Z. G. Shao, X. S. Ye, L. Yang, and C. L. Wang, J. Appl. Phys. **114**, 093712 (2013).

[161] H. Liu, J. Gao, and J. Zhao, J. Phys. Chem. C **117**, 10353 (2013).

[162] W.-F. Tsai, C.-Y. Huang, T.-R. Chang, H. Lin, H.-T. Jeng, and A. Bansil, Nature Communications **4**, 1500 (2013).

[163] Z. Ni, H. Zhong, X. Jiang, R. Quhe, G. Luo, Y. Wang, M. Ye, J. Yang, J. Shi, and J. Lu, Nanoscale **6**, 7609 (2014).

[164] S. Li, Y. Wu, Y. Tu, Y. Wang, T. Jiang, W. Liu, and Y. Zhao, Scientific Reports **5**, 7881 (2015).

[165] A. C. Ferrari, F. Bonaccorso, V. Falko, K. S. Novoselov, S. Roche, P. Bøggild, S. Borini, F. Koppens, V. Palermo, N. Pugno, J. a. Garrido, R. Sordan, A. Bianco, L. Ballerini, M. Prato, E. Lidorikis, J. Kivioja, C. Marinelli, T. Ryhänen, A. Morpurgo, J. N. Coleman, V. Nicolosi, L. Colombo, A. Fert, M. Garcia-Hernandez, A. Bachtold, G. F. Schneider, F. Guinea, C. Dekker, M. Barbone, C. Galiotis, A. Grigorenko, G. Konstantatos, A. Kis, M. Katsnelson, C. W. J. Beenakker, L. Vandersypen, A. Loiseau, V. Morandi, D. Neumaier, E. Treossi, V. Pellegrini, M. Polini, A. Tredicucci, G. M. Williams, B. H. Hong, J. H. Ahn, J. M. Kim, H. Zirath, B. J. van Wees, H. van der Zant, L. Occhipinti, A. Di Matteo, I. a. Kinloch, T. Seyller, E. Quesnel, X. Feng, K. Teo, N. Rupesinghe, P. Hakonen, S. R. T. Neil, Q. Tannock, T. Löfwander, and J. Kinaret, Nanoscale **7**, 4598 (2014).

[166] J. Gao, J. Zhang, H. Liu, Q. Zhang, and J. Zhao, Nanoscale **5**, 9785 (2013).

[167] V. O. Özçelik, H. H. Gurel, and S. Ciraci, Physical Review B **88**, 045440 (2013).

[168] A. D. S. Martins and M. Veríssimo-Alves, Journal of Physics: Condensed Matter **26**, 365501 (2014).

[169] M. Brandbyge, J.-L. Mozos, P. Ordejón, J. Taylor, and K. Stokbro, Physical Review B **65**, 165401 (2002).

[170] A. R. Rocha, V. García-Suárez, S. Bailey, C. Lambert, J. Ferrer, and S. Sanvito, Physical Review B **73**, 85414 (2006).

[171] N. Troullier, Phys. Rev. B **43**, 1993 (1991).

[172] S. Cahangirov, M. Topsakal, E. Aktürk, H. Şahin, and S. Ciraci, Physical Review Letters **102**, 236804 (2009).

[173] M. Paulsson and M. Brandbyge, Physical Review B **76**, 115117 (2007).

[174] F. Schedin, A. K. Geim, S. V. Morozov, E. W. Hill, P. Blake, M. I. Katsnelson, and K. S. Novoselov, Nature Materials **6**, 652 (2007).

[175] Y.-H. Zhang, Y.-B. Chen, K.-G. Zhou, C.-H. Liu, J. Zeng, H.-L. Zhang, and Y. Peng, Nanotechnology **20**, 185504 (2009).

[176] D. J. Appelhans, M. T. Lusk, and Z. Lin, Physical Review B **82**, 073410 (2010).

[177] R. Atta-Fynn, P. Biswas, P. Ordejón, and D. A. Drabold, Physical Review B **69**, 085207 (2004).

[178] R. R. Nair, W. Ren, R. Jalil, I. Riaz, V. G. Kravets, L. Britnell, P. Blake, F. Schedin, A. S. Mayorov, S. Yuan, M. I. Katsnelson, H.-M. Cheng, W. Strupinski, L. G. Bulusheva, A. V. Okotrub, I. V. Grigorieva, A. N. Grigorenko, K. S. Novoselov, and A. K. Geim, Small **6**, 2877 (2010).

[179] J. T. Robinson, J. S. Burgess, C. E. Junkermeier, S. C. Badescu, T. L. Reinecke, F. K. Perkins, M. K. Zalalutdniov, J. W. Baldwin, J. C. Culbertson, P. E. Sheehan, and E. S. Snow, Nano Letters **10**, 3001 (2010).

[180] R. Stine, W.-K. Lee, K. E. Whitener Jr., J. T. Robinson, and P. E. Sheehan, Nano Letters **13**, 4311 (2013).

[181] W. H. Lee, J. W. Suk, H. Chou, J. Lee, Y. Hao, Y. Wu, R. Piner, D. Akinwande, K. S. Kim, and R. S. Ruoff, Nano Letters **12**, 2374 (2012).

Acta Universitatis Upsaliensis

Digital Comprehensive Summaries of Uppsala Dissertations
from the Faculty of Science and Technology 1432

Editor: The Dean of the Faculty of Science and Technology

A doctoral dissertation from the Faculty of Science and
Technology, Uppsala University, is usually a summary of a
number of papers. A few copies of the complete dissertation
are kept at major Swedish research libraries, while the
summary alone is distributed internationally through
the series Digital Comprehensive Summaries of Uppsala
Dissertations from the Faculty of Science and Technology.
(Prior to January, 2005, the series was published under the
title "Comprehensive Summaries of Uppsala Dissertations
from the Faculty of Science and Technology".)

ACTA
UNIVERSITATIS
UPSALIENSIS
UPPSALA
2016